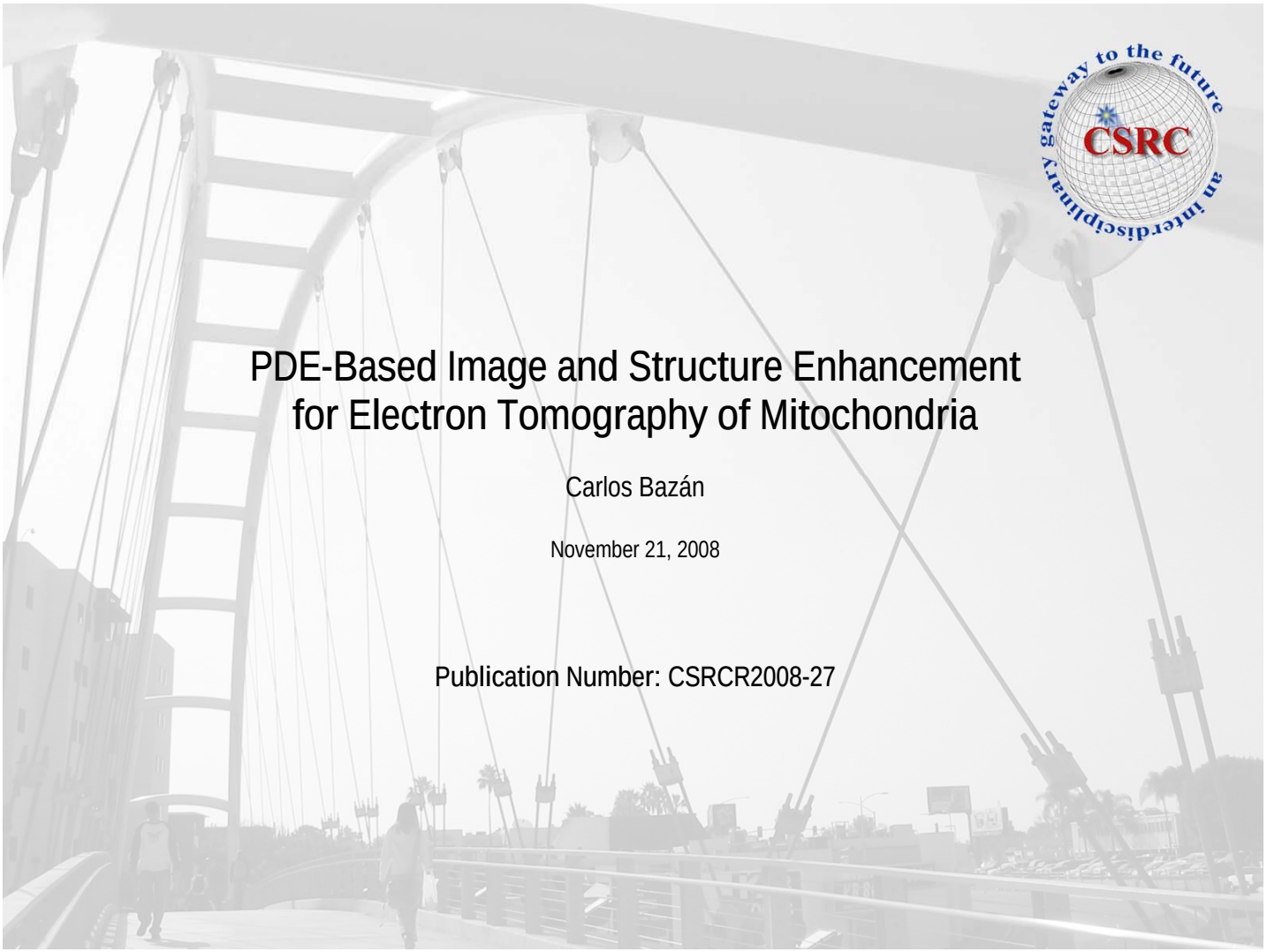

PDE-Based Image and Structure Enhancement for Electron Tomography of Mitochondria

Carlos Bazán

November 21, 2008

Publication Number: CSRCR2008-27

Computational Science & Engineering Faculty and Students Research Articles

Database Powered by the Computational Science Research Center Computing Group & Visualization Lab

COMPUTATIONAL SCIENCE & ENGINEERING

SAN DIEGO STATE UNIVERSITY

Computational Science Research Center
College of Sciences
5500 Campanile Drive
San Diego, CA 92182-1245
(619) 594-3430

PDE-Based Image and Structure Enhancement for Electron Tomography of Mitochondria

by

Carlos Alberto Bazán

A Dissertation
Submitted to the Faculty of
San Diego State University
and
Claremont Graduate University

In Partial Fulfillment of
the Requirements for the Degree of
Doctor of Philosophy
in
Computational Science

San Diego, California

Approved by:

Peter Blomgren

We, the undersigned, certify that we have read this dissertation by Carlos Alberto Bazán and approve it as adequate in scope and quality for the degree of Doctor of Philosophy.

Dissertation Committee:

Peter Blomgren, Chair

Robert Mellors, Member

Ali Nadim, Member

Hedley Morris, Member

Peter Salamon, Member

Dedication

To my wife María del Carmen and my children

Carlos Sebastián, Pedro Nicolás, and Melissa Mariah.

In molecular biology there are technical advances, discoveries, and ideas—usually in that order.

– Sydney Brenner
2002 Nobel prize in Physiology or Medicine laureate

Abstract of the Dissertation

PDE-Based Image and Structure Enhancement

for Electron Tomography of Mitochondria

by

Carlos Alberto Bazán

San Diego State University and Claremont Graduate University

Mitochondrial function plays an important role in the regulation of apoptosis. Additionally, defects in this function are believed to be related to many common diseases of aging. In the presence of one of these diseases, mitochondrial function undergoes measurable disturbance accompanied by drastic morphological alterations, suggesting that a correlation exists between mitochondrial structure and functionality. However, the interpretation and measurement of the architectural organization of mitochondria depend heavily upon the availability of good software tools for filtering, segmenting, extracting, measuring, and classifying the features of interest. In this work, we develop mathematically sound and computationally robust partial differential equation-based algorithms for the reduction of noise, and the enhancement of structural information in images of mitochondria obtained via electron microscope tomography.

We design a multi-stage approach for extracting the mitochondrial structures from electron tomograms. For the noise reduction phase of the pipeline, we devise a structure enhancing anisotropic nonlinear diffusion model. It is based on an improved image smoothing and edge detection technique that employs a combination of nonlinear diffusion and bilateral filter. The eigenvectors of the bilaterally smoothed structure tensor form the basis for the diffusion tensor, where the eigenvalues are prescribed so that there is a smooth transition, rather than a hard threshold switching, of the diffusion characteristics among image areas of differing structural properties. The

method is equipped with a new and simple diffusion stopping criterion, derived from the second derivative of the correlation between the noisy image and filtered image. After the noise reduction phase, we synthetically enhance the contrast of the image by applying the confidence connected segmentation algorithm. Following that, structures are extracted using a level set formulation which includes a term that drives the level set function toward a signed distance function. The extracted contours are rendered as a three-dimensional image model. The results are very encouraging and this computational approach is potentially much faster, and is more robust and unbiased than hand-tracing of structures.

We develop an adaptive total variation-based model with morphologic convection and anisotropic diffusion, and devise a user-independent method for choosing all the parameters in the model. We estimate the unknown noise level via a simple approximation that uses convolution with a Gaussian kernel. We implement a pixel-wise parameter in the forcing-term that allows more diffusion in homogeneous areas, and it restricts the diffusion in areas with higher probability of belonging to edges. This parameter also enables more diffusion in the early stages of the scale-marching process and discourages diffusion as iterations evolve. For the anisotropic diffusion process, we implement a diffusion tensor that adapts to the underlying structure of the image by applying a range of diffusion processes in each direction. The proposed model applies diffusion methods consistent with either the total variation-norm or the Euclidean-norm, or an interpolation between these two norms. We also implement an adaptive time-step that helps with the stability and the speed of the total variation-based restoration process. The adaptive time-step is smaller in regions with high gradients and is larger in regions with low gradients. The results obtained by applying this model to noisy images are comparatively superior in both speed and quality of the restoration.

We propose a homomorphic total variation-based algorithm for the reduction of the multiplicative noise present in low-dose electron microscope imagery. In the implementation of this model we employ some of the aforementioned adaptive parameters that we devise for the adaptive total variation-based model. We compare the performance of the proposed model to that of a total variation-based algorithm that was originally designed for the removal of multiplicative noise. The resulting images after applying both techniques are very similar in quality. Ours is the first implementation of this method within the context of electron microscope tomography.

Acknowledgements

This thesis has been an amazing journey. It was made possible through the support of many people and organizations to whom I owe a great deal of appreciation. First and foremost, I would like to express my sincere gratitude to my adviser and friend Prof. Peter Blomgren, for his invaluable guidance and mentoring during the more than four years of this thesis's work. The contributions from this research are the results of our countless, fruitful, and 'highly caffeinated' discussions. I feel deeply thankful to Prof. Jose Castillo for his relentless leadership as head of the Computational Science Research Center. His enthusiastic entrepreneurship has been a real inspiration throughout my years as a doctoral student. I was delighted to interact with Prof. Paul Paolini by participating in several of the many programs he runs at San Diego State University. I greatly benefited from his wisdom and insight.

Prof. Ali Nadim, Prof. Alpan Raval, Prof. Hedley Morris, Prof. Robert Mellors, and Prof. Peter Salamon deserve special thanks as my thesis committee members and advisors, and for their constructive comments on this work. Prof. Nadim and Prof. Raval are two of the excellent instructors I had during my year of residency at Claremont Graduate University. Prof. Mellors and Prof. Salamon are two of the first faculty members with whom I interacted after joining the doctoral program. Since then, they have been actively collaborating in this research in various capacities. I am very grateful to Prof. Terrence Frey and the San Diego State University Mitochondria Research Group, for their always helpful input and for providing the data used in our computations. From this group, my special thanks go to Mei Sun and Mariam Ghochani. I gratefully thank Prof. Barbara Bailey and Prof. Kristin Duncan for helping me with the statistical aspects of this research. My gratitude also goes to Michelle Miller for co-authoring one of our papers.

No research work can be possible without the generous support from funding organizations, and this is no exception. I greatly appreciate the support of the National Institutes of Health through its NIW RoadMap Initiative award R90 DK07015, for providing the main funding for this research. I am also very appreciative of the early support I received from the Department of Finance, College of Business Administration at San Diego State University. The support I received from Prof. Nikhil Varaiya, Prof. Swaminath Badrinath, Prof. Kuntara Pukthuanthong-Le, Prof. Tom Warshauer, and Prof. Edward Omberg is very much appreciated. I would also like to acknowledge the support I received from the Department of Energy that allowed my training internship at Lawrence Berkeley Laboratory, and the National Science Foundation that permitted my training at both the University of California San Diego and the University of California Los Angeles.

I would also like to thank the following people: Prof. Roger C. Wagner from the University of Delaware, Dr. Anton Hillebrand and Dr. Vladan Lučić from the Max Planck Institute of Biochemistry, Amanda Charr Englund from the FEI Company, and Prof. José-Jesús Fernández from the University of Almeria for providing comments and some figures for this thesis; Dr. James Otto, Jane Kalionzes, Kristin Kuipers, Keely Bamberg, Dr. Chao-Jen Wong, Wes Bethel, Parisa Plant, and Sofia Clemente, for all their help and their friendship. My utmost gratitude goes to my family, my wife María del Carmen and my children Carlos Sebastián, Pedro Nicolás, and Melissa Mariah, for their unconditional love and support throughout my life, this thesis would have simply been impossible without them.

Contents

List of Figures

List of Tables

List of Abbreviations

1D	one dimensional
2D	two dimensional
3D	three dimensional
AND	anisotropic nonlinear diffusion
ATP	adenosine triphosphate
ART	algebraic reconstruction technique
BF	bilateral filter
BV	bounded variation
CB	conjugate barrier
CCD	charged-coupled device
CED	coherence enhancing diffusion
CFL	Courant-Friedrichs-Lewy (condition)
CT	computed tomography
CTF	contrast-transfer function
DFM	direct Fourier method
DNA	deoxyribonucleic acid
DOF	degree-of-freedom
DQE	detector quantum efficiency
EED	edge enhancing diffusion
EM	electron microscopy
EMCCD	electron multiplying charge-couple device
ET	electron (microscope) tomography
FEG	field-emission gun
FBP	filtered back-projection
GD	Gaussian diffusion
HPF	high pressure freezing
ICCD	intensified charge-couple device
ILST	iterative least-squares technique
MAD	median absolute deviation
keV	kilo-electron volt
ML-EM	maximum likelihood-expectation maximization
mtDNA	mitochondrial deoxyribonucleic acid
MTF	modulation transfer function

μm	micrometer (10^{-6} meter)
NMR	nuclear magnetic resonance
nm	nanometer (10^{-9} meter)
OSL-EM	one step late-expectation maximization
PDE	partial differential equation
PET	positron emission tomography
RF/FS	rapid freezing with freeze-substitution
POCS	projection on convex sets
PSF	point spread function
ROI	region of interest
SAR	synthetic aperture radar
SED	structure enhancing diffusion
SER	series expansion reconstruction
SIRT	simultaneous iterative reconstruction technique
SNR	signal-to-noise ratio
SPECT	single positron emission computed tomography
SSC	slow-scan charge-couple device
TEM	transmission electron microscope
TIM	Tikhonov iterative method
TV	total variation
WBP	weighted back-projection
WT	wavelet transform

List of Symbols

$*$	convolution operator
Ω	image domain
$\partial\Omega$	boundary of the image domain Ω
$\lvert\Omega\rvert$	measure of the image domain Ω
f	true or noise-free image
u_0	observed or noisy image
u	restored or filtered image
u_σ	convolved image with a Gaussian, $G_\sigma * u$
u_{bf}	convolved image with bilateral filter, $G_{bf} * u$
η	additive noise
m	multiplicative noise
$\delta x, \delta y, \delta z$	grid size discretization, usually set $\delta x = \delta y = \delta z = 1$
δt	time-step
d	dimensionality of the data
t	scale parameter or time of the diffusion process
u_t	shorthand notation for $\partial u/\partial t$
u_x, u_y, u_z	shorthand notation for $\partial u/\partial x$, $\partial u/\partial y$, $\partial u/\partial z$
∇	gradient operator
∇^2	Laplacian operator
$\lvert\nabla u\rvert$	magnitude of the gradient of u, $\sqrt{u_x^2 + u_y^2}$, at point (x, y)
div or $\nabla\cdot$	divergence operator
G_σ	Gaussian kernel of with σ
G_{bf}	bilateral filter kernel
$\mathbf{D}_\sigma$	diffusion tensor (from $\mathbf{J}_\sigma$)
$\mathbf{D}_\rho$	diffusion tensor (from $\mathbf{J}_\rho$)
$\mathbf{D}_{bf}$	diffusion tensor (from $\bar{\mathbf{J}}_{bf}$)
g	diffusivity function
λ	contrast parameter or Lagrange multiplier
σ	noise scale or width of the Gaussian kernel G_σ
$\mathbf{n}$	outward normal vector
$\mathbf{J}_\sigma$	structure tensor $\nabla u_\sigma \cdot \nabla u_\sigma^{\mathrm{T}}$
$\mathbf{J}_\rho$	structure tensor $G_\rho * \mathbf{J}_\sigma$
$\mathbf{J}_{bf}$	structure tensor $\nabla u_{bf} \cdot \nabla u_{bf}^{\mathrm{T}}$

$\bar{\mathbf{J}}_{bf}$	structure tensor $G_{bf} * \mathbf{J}_{bf}$
$\mathbf{v}_i$	eigenvector of the structure and diffusion tensors
λ_i	eigenvalue of the diffusion tensor
μ_i	eigenvalue of the structure tensor
$\langle a, b \rangle$	scalar, dot product, or inner product of a and b
μ	mean value
β	bias term parameter
α	regularization constant, typically set to 10^{-3}
C	coherence parameter
C_i	coherence parameter $(i = 2, 3)$
p	percentile for the Perona-Malik estimation of λ
p_i	exponent in the Blomgren-Chan-Mulet model
T	stopping time of the diffusion process
$\mathbf{I}$	identity matrix
P_i	structure feature metrics
V	subvolume of the 3D data u
$\mathbf{x}$	coordinate of a pixel, (x, y), or a voxel, (x, y, z)
$\mathrm{var}\,(a)$	variance of a
$\mathrm{corr}\,(a, b)$	correlation coefficient between a and b

Chapter 1

Introduction

1.1 Motivation

Scientists have been captivated by mitochondria[1] ever since they were first described by Kölliker (1856) as filamentous (mito) and grain (chondrium)-like structures in muscle cells [83]. Mitochondria are cellular organelles *conditio sine qua non* complex animals could not evolve in aerobic conditions. They carry out most cellular oxidation and produce the majority of the adenosine triphosphate (ATP), which is the universal energy currency of all known living organisms [399]. Since the early 1990's the study of mitochondria has undergone a revival, fueled by landmark discoveries and considerable advances in our understanding of phenomena such as mitochondrial import, movement, fission, fusion, inheritance, and interactions with the nucleus and other organelles [301].

To date, it is firmly established that mitochondrial function plays an important role in the regulation of apoptosis or programmed cell death [149, 195, 196, 197, 215, 270, 362]. For instance, following a variety of cell death signals, mitochondria exhibit early alterations in function and morphological changes, such as the opening of the permeability transition pore or mitochondrial megachannel [38, 52, 126, 180, 186, 226,

[1] Benda (1898) coined the term 'mitochondria' to define these cellular organelles.

297, 399, 400, 409]. There is also strong evidence that defects in function may be related to many of the most common diseases of aging, such as Alzheimer dementia, Parkinson's disease, type II diabetes mellitus, stroke, atherosclerotic heart disease, and cancer[2]. This assertion is founded on the observation that mitochondrial function undergoes measurable disturbance accompanied by drastic morphological alterations in the presence of these multisystem diseases [12, 82, 91, 127, 257, 267, 290, 345].

Concurrent with the aforementioned conceptual advances, there has been a significant increase in the types of tools available to study the correlation between mitochondrial structure and function. Along with the now classic methods for isolating mitochondria and assaying their biochemical properties, there are new and powerful methods for visualizing, monitoring, and perturbing mitochondrial function while assessing their genetic consequences [227, 301]. Electron (microscope) tomography (ET) has allowed important progress in the understanding of mitochondrial structure. This imaging technique currently provides the highest three-dimensional (3D) resolution of the internal arrangement of mitochondria in thick sections [165, 289, 293]. Nevertheless, the interpretation and measurement of the architectural organization of mitochondria depend heavily on the availability of good software tools for filtering, segmenting, extracting, measuring, and classifying the features of interest [128, 224, 292, 315, 328].

It has been argued in the structural biology community [127, 205] that the image processing methodologies in the 3D ET field are not yet sufficiently developed, so as to correctly extract features and understand spatial relationships in the mitochondrial structure. There is strong need for a set of image processing methodologies that

[2]It has been estimated that mitochondrial disorders affect at least 1 in 5000 of the population [327]. Skeletal and cardiac muscles and the central nervous system are most commonly affected by mitochondria disorders [187, 291, 319]. Please refer to Appendix A for a more comprehensive list of mitochondria disorders and their clinical syndromes.

will facilitate efficient analysis of the data obtained via ET [240, 401]. Therefore, the main motivation for this work is the development of mathematically sound and computationally robust algorithms for the reduction of noise and the enhancement of structural information in mitochondrial images. We carry out an inter-disciplinary approach, based on a combination of established expertise in the fields of image processing, mathematics, computational science, and structural biology. Our research efforts initially focus on the understanding of the sources and mechanisms which introduce noise (image degradation) in the ET processes. Correct modeling of the degradation helps us design effective algorithms for the removal of the noise without negatively impacting fine-detail structural information, and allows for more accurate *a posteriori* feature recognition, boundary segmentation, and visualization.

1.2 Goal of the Thesis

The objective of this research from the standpoint of its contribution to the state of the art is to develop, implement, and integrate modern image processing techniques in order to obtain more accurate structural information of mitochondria from data collected using 3D ET. The larger goal is to help boost the understanding of the intricate mitochondrial architecture and its relation to functionality. In general, this work is relevant to the structural biology community and its contribution to public health through the understanding of biological systems. In particular, our work will help the San Diego State University Mitochondria Research Group led by Prof. Terrence Frey. This group has been investigating the structure and function of mitochondria among other biological assemblies for many years. They apply techniques of high resolution electron microscopy (EM) and digital image processing to study the structures of biological macromolecules, macromolecular assemblies, and whole organelles. Their

study of mitochondria has led, along with the work of several other research groups, to a new paradigm of mitochondria structure.

As mentioned above, the interpretation and measurement of the structure of mitochondria depend crucially on the employment of algorithms for segmenting and classifying the features of interest, tools for making 3D measurements, and software for interactively visualizing components of the structure [290]. There have been many technical improvements in computational tools (both hardware and software) aimed at furthering the capability of extracting quantitative information from 3D ET. Several software applications and computational techniques have been specifically developed for ET. These packages offer comprehensive sets of tools that allow a wide range of structural biology analyses. The most popular general packages are IMOD [192, 230], SPIDER [30, 124, 398], Protomo [347, 387, 388, 389], SerialEM [231], EM3D [159], XMIPP [333], TOM [266], EMAN/EMAN2 [218, 346], and UCSF tomography [403, 404]. There are also many tools available that permit specialized tasks such as data acquisition [231, 266, 344, 403, 404, 407], signal filtering [47, 111, 117, 223, 249, 273, 334, 363, 388], image segmentation [212, 310, 366], and data visualization [21, 143, 395, 396]. Nevertheless, two of the most critical aspects within the ET processes, namely the 3D filtering and two-dimensional (2D) and 3D segmentation and feature extraction processes, are still the subject of active research. The former constitutes the main topic of this thesis.

1.3 Thesis Contributions

In chapter 2 we summarize our findings from an extensive literature review on image degradation in the ET processes. Good understanding of the sources and mechanisms that incorporate noise and artifacts in cryo-electron tomography from thick-section

specimens allows for the application of appropriate image processing techniques. As a result of this research, we propose to model the noise in ET by a combination of additive and multiplicative noise. For high counts (as in high-dose ET), the image is predominantly perturbed by additive noise. In low-dose ET, it is more accurate to assume that the image is degraded by multiplicative noise. The simplicity of this noise model for ET makes it very attractive for employing basic techniques, adapted from classic and well established partial differential equation (PDE) -based image processing methodologies.

The contributions in chapter 3 can be divided into two parts. In the first part of the chapter, we propose a new image smoothing and edge detection technique that employs a combination of nonlinear diffusion and bilateral filter. The model is based upon two very well established methodologies in the image processing community, which makes the model easy to understand and implement. Our numerical experiments show that the proposed model is capable of achieving more accurate restorations from noisy images, as compared to two other popular nonlinear diffusion models in the literature. We also propose a new and simple diffusion stopping criterion, derived from the second derivative of the correlation between the noisy image and the filtered image. This indirect measure allows stopping the diffusion process very close to the point of maximum similarity between the noise-free image and the restored image, in the absence of the former. The stopping criterion is sufficiently general to be applied with most nonlinear diffusion methods normally used for image noise removal.

In the second part of the chapter we present a multi-stage approach for extracting the mitochondria structures from ET. (i) In the initial restoration, or noise reduction phase, we propose a structure enhancing anisotropic nonlinear diffusion strategy. The local structure tensor is formed from the gradient information of a bilaterally

smoothed version of the current image. In order to close gaps in structures caused by imaging limitations, the local structure tensor is further smoothed with a bilateral filter, forming a smoothed version of the structure tensor. The eigenvectors of the smoothed structure tensor form the basis for the diffusion tensor, where the eigenvalues are prescribed so that there is a smooth transition, rather than a hard threshold switching of the diffusion characteristics between image areas of differing structure properties. (ii) After the noise reduction phase, we synthetically enhance the contrast of the image by applying the confidence connected segmentation algorithm. (iii) Following that, structures are extracted using a level set formulation which includes a term that drives the level set function toward a signed distance function. This both simplifies the initialization of the algorithm and removes the need for re-initialization. (iv) The extracted contours are rendered as a 3D image model. The results are very encouraging and this computational approach is potentially much faster, and is more robust and unbiased than hand-tracing of structures.

The contributions in chapter 4 can also be divided into two parts. In the first part we develop an adaptive total variation-based model with morphologic convection and anisotropic diffusion, and devise a user-independent method for choosing all the parameters in the model. We start by estimating the unknown noise level via a simple approximation that uses convolution with a Gaussian kernel. This parameter is updated at each iteration and as the noise is being removed, it reduces the diffusion and helps reach convergence. We implement a pixel-wise parameter in the forcing-term that allows more diffusion in homogeneous areas and restricts the diffusion in areas with higher probability of belonging to edges. This parameter also allows more diffusion in the early stages of the scale-marching process and less diffusion as iterations evolve. These are desirable attributes in image noise removal applications. For the anisotropic diffusion process, we implement a diffusion tensor that not only

steers the diffusion in such a way that the eigenvectors prescribe the diffusion directions and the corresponding eigenvalues determine the amount of diffusion along these directions, but also adapts to the underlying structure of the image and applies a range of diffusion processes in each direction. The proposed model applies diffusion methods consistent with either the total variation-norm or the Euclidean-norm, or an interpolation between the two norms. Finally, we implement an adaptive time-step that helps with the stability and the speed of the total variation-based restoration process. The size of the time-step varies across the image at each iteration. The adaptive time-step is smaller in regions with high gradients and is larger in regions with low gradients. Both of these are desirable features for preserving the edges and for smoothing isotropic regions, respectively.

In the second part of this chapter we design a homomorphic total variation-based algorithm for the reduction of the multiplicative noise present in low-dose EM imagery. In a homomorphic system, the natural logarithm is used to transform the multiplicative nature of the degradation into an additive one and then, the resulting degraded image is processed by using a filter to reduce the additive noise. An exponential function is then applied to the output of the filter. In the implementation of this model we employ some of the adaptive parameters we devise in the first part of the chapter. For the purpose of performance comparison, we implement a total variation-based model that was originally designed for the removal of multiplicative noise. Ours is the first implementation of this method within the context of EM tomography.

1.4 Overview of the Chapters

Chapter 2 provides an overview of the main procedures involved in the EM of large biological material volumes. This overview helps identify the steps that are more prompt to noise and artifacts. A good understanding of the image degradation introduced during the ET processes allows for the design of appropriate image processing methodologies for EM imagery. Chapter 3 is about anisotropic nonlinear diffusion and the application of these models for the denoising of images and the enhancement of image structures. In this chapter we present a review of the Perona-Malik-type models that where adapted for the processing of electron tomograms, and propose a multi-stage approach for the extraction of mitochondrial structures from electron tomogram for visualization and analysis. Chapter 4 deals with total variation-based methods and the employment of these models for the removal of noise in images while preserving the structures (edges). We offer a survey of the application of these methods predominantly during the 3D volume reconstruction, and introduce total variation-based methods as a viable approach for the removal of noise from electron tomograms. Chapter 5 presents the algorithms that were used to implement the experiments in this research. The main emphasis is put in the design of simple algorithm that can run in parallel using the new MATLAB® Parallel Computing Toolbox™.

Chapter 2

Electron (Microscope) Tomography

2.1 Introduction

The basic concepts employed in ET have been known since the early part of the twentieth century. They are based on a principle first discovered by Radon [305] in 1917, *i.e.*, a 3D reconstruction of an object can be retrieved from its projections. In 1968, De Rosier and Klug [81] applied this principle to formulate an algorithm for the reconstruction of a 3D object from a set of electron microscope images. Coincidentally, Hart [160] used an electronic picture-scanning device and a digital computer to superimpose and form a montage of electron micrographs[1] taken from a specimen along several different directions. These events opened the doors to the possibility of using ET to bridge the gap between the biological structural studies at the molecular and cellular levels[2] [220, 243, 343]. The complete procedure to reconstruct, model, and interpret large biological material volumes by ET can be divided into four main steps: (i) specimen preparation, (ii) electron microscopy, (iii) volume computation, and (iv) image analysis and interpretation [171]. All of these steps have their own practical challenges and are potential sources of noise and artifacts.

[1] Electron micrographs (tilt series) are 2D projections of the specimen at different tilt angles.

[2] Among the interesting objects in this size range are cellular protein machines, giant protein and nucleic acid assemblies, large subcellular organelles (mitochondria), and small bacteria [401].

2.2 Specimen Preparation

Most of the recent resurgence of interest in ET is undoubtly due to improvements in specimen preparation. All of the earlier techniques were notorious for their artifacts [29, 122, 125, 220, 242, 243]. Today, different techniques are employed based on several variables such as specimen type, the kind of structural information to be retrieved, and characteristics of the equipment being used [6]. Some of these specimen preparation techniques are (i) staining, (ii) chemical fixation and plastic embedding, (iii) rapid freezing, (iv) rapid freezing with freeze-substitution and plastic embedding, and (v) cryopreparation and cryosectioning.

(i) Staining with heavy metal salts is often used as a means of increasing the contrast in the images. This contrast is achieved in two ways: in positive staining, the heavy metal salt forms a complex with the organic material turning it darker. In negative staining, the heavy metal salt replaces the water by penetrating the cavities around the molecules, turning darker the surroundings of the organic material. Often times the specimen presents both positive and negative staining, making interpretation of complex structures very difficult. Furthermore, it has been argued [220] that what is seen on the micrographs is the stain and not the biological material. Nevertheless, staining is very useful for the earlier stages of research to get a first glimpse of the structure.

(ii) Chemical fixation and plastic embedding preparation involves various steps: chemical fixation, dehydration in organic solvents, embedding in resin or plastic, sectioning into slices, and staining with heavy metal salts. The chemical fixation step can cause structural rearrangements within the specimen and, along with the dehydration step, it can promote leakage of some cytoplasmic components and the formation of artifacts [220, 259].

(iii) Rapid freezing or 'cryofixation' involves freezing the specimen very rapidly to reach a temperature below $-140°C$ and avoiding the formation of crystals. The objective in cryofixation is to immobilize all constituents of the specimen before any significant structural rearrangement occurs, and whereby the specimen will be embedded in vitreous (amorphous) ice in near physiological state[3] [8, 94, 220]. For specimens of up to a few hundred μm high pressure freezing (HPF) is required[4], by which the sample is pressurized and frozen by jets of liquid nitrogen [252]. This technique is currently the best method for structural preservation of most cells and tissues in thick sections [95, 234, 241]. However, it has the main disadvantage[5] that contrast between ice and biological macromolecules is very low, making it necessary to employ enough electrons in order to reach a statistically reliable image [46, 152, 173, 190, 236, 300, 311, 318, 335]. This goes in detriment of the specimen's integrity since it is extremely sensitive to the electron beam[6] [355].

(iv) Rapid freezing with freeze-substitution (RF/FS) and plastic embedding is an improvement over chemical fixation and plastic embedding [184, 235, 339]. The steps involved in this preparation are: rapid freezing or HPF, freeze-substitution of water by an organic solvent[7] containing chemical fixatives at temperature around $-90°C$, embedding in resin or plastic at temperature below $-40°C$, sectioning into slices, and staining with heavy metal salts. Despite the improvements, this technique still

[3]If the specimen is thawed after using this method, a large portion of its cells will continue to grow and divide [205, 239].

[4]This follows from the fact that the volume of water increases during crystallization.

[5]It has been also argued [96] that vitreous sections suffer from deformation during the cutting process, but that this effect takes place without loss of information provided that the information is homogeneous.

[6]Exposure of the specimen to the electrons induces ionization, breaking of chemical bonds, and formation of free radicals (radiolysis) [220]. Thus, the accumulated electron dose over all projection views should not exceed the limit of 2000 e^-/nm^2 [119, 122]. For details on the 'dose fractionation theorem' the reader should refer to the early work by Hegerl and Hoppe [164], and consult [99, 122, 141, 142, 190, 219, 265, 300, 335] and the references therein for further information on the physics behind specimen damage.

[7]This is a slow process that takes from two to three days [171].

produces aggregation artifacts [95] and limited resolution [220]. This limitation is due to stain rearrangement, formation of stain aggregates during electron irradiation, and difficulty to differentiate stain from biological material [239].

(v) Cryopreparation and cryosectioning (sectioning at low temperature) comprises plunge freezing the specimen (prior to sectioning) with no additional preparation, to investigate the sample in the frozen-hydrated state [93]. Even though this technique allows the study of biological material near physiological state, it is only suitable for studying relatively thin specimens, up to 500 nm. Also, since the sample is kept on the grid for a few second before freezing, the surface tension of water may induce flattening in the direction perpendicular to the grid [220]. In addition, cryosectioning is a source of several artifacts such as knife marks, crevasses, and compression [7].

2.3 Electron Microscopy

2.3.1 Instrumentation

Modern ET setups (see Fig. 2.1) consist of a transmission electron microscope (TEM) equipped with: (i) a field-emission gun (FEG) and a computer-controlled stage, (ii) an energy filter, and (iii) a charge-couple device (CCD) camera[8] [78, 104, 200, 194, 220, 336].

(i) FEG microscopes have the main advantage of producing high spatial and temporal coherence electron beam [242]. They achieve the preservation of high-resolution information in low contrast objects, like frozen-hydrated biological samples, thanks to the minimal attenuation of the contrast-transfer function (CTF). Thick samples require imaging at intermediate (200-600 keV) and high ($\geq$ 800 keV) voltages for the electron beam to penetrate them.

[8]This is usually a slow scan CCD camera (SSC). There are also available the high-end electron multiplying charge-coupled device (EMCCD) cameras and the intensified charge-coupled device (ICCD) cameras.

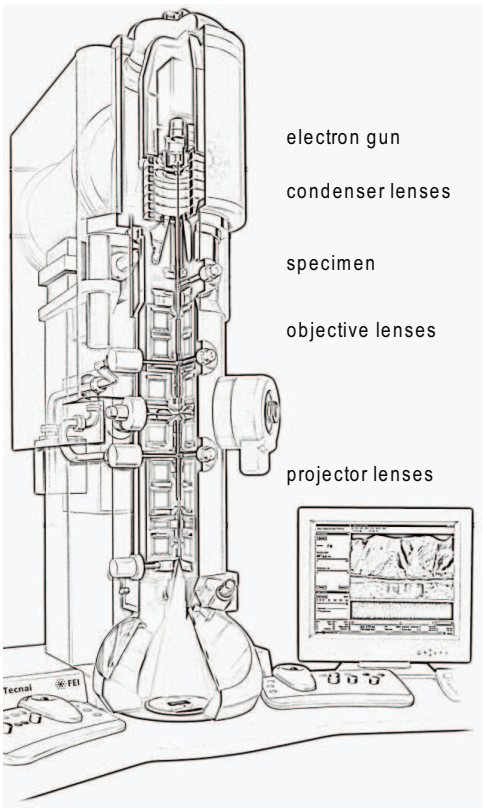

Figure 2.1: Schematic representation of a TEM with its basic parts: high voltage source, electron gun, condenser lenses, specimen holder, objective lenses, projector lenses, and imaging device. Adapted from an original image courtesy of Amanda Charr Englund (FEI Company). Reproduced with permission.

(ii) Energy filters are necessary when imaging thick specimens. Inelastic scattering events are inevitable when electrons interact with these samples, leading to energy exchange between them. This is usually experienced in the form of energy loss from the primary beam, where energy is transferred to the sample through the excitation of modes specific to the specimen [49]. The most noticeable effect of inelastic scattering is strong blurring [220]. Energy filters allow the reduction of chromatic aberration (polyenergetic imaging) in TEM, and the imaging of thick section at relatively higher signal-to-noise (SNR) ratio.

(iii) Current CCD cameras for ET record an electron image in three stages [108]: 1) Electrons are converted into photons in an electron scintillator, 2) Photons are transported to the CCD array via lens coupling [104] or fiber optic coupling [78, 200, 194, 107], and 3) Photons are converted into well-electrons and these are read out in the CCD. The disadvantage of this detection process is that backscattering of electrons in the scintillator degrades the performance of the CCD camera, specially for higher accelerating voltages. This stage is currently unavoidable since the CCD is severely damage if exposed to the electrons directly. A better recording device for EM would be the one that detects electrons directly. Unfortunately, this technology has not been widely adopted due to some practical issues [103, 105, 108].

2.3.2 Data Acquisition and Image Formation

Data acquisition involves the recording of a series of micrographs. This was made possible by the development of automated procedures that acquire a tilt series under low-dose conditions [85, 86, 87, 150, 351]. The automated acquisition of a tilt series comprises three steps, (i) tracking, (ii) autofocusing, and (iii) exposure.

(i) The tracking procedure determines possible lateral displacement of the specimen as compared to the previous tilt angle.

(ii) The autofocusing step determines possible defocus change by comparing micrographs at different beam tilts [191, 406].

(iii) Once the necessary adjustments have been determined, the final image is recorded under normal-dose conditions. The previous two steps are executed under very low-dose conditions, at positions that are shifted along the tilt axis in reference to the exposure location, to minimize the electron dose received by the region of interest (ROI) [220].

The data acquired in the aforementioned process show the projections of the elec-

trostatic density in the sample, *i.e.*, each pixel represents the total energy along a straight line[9] perpendicular to the imaging plane [39] (see Fig. 2.2). Image formation (contrast-forming mechanism) in a TEM depends on the specimen preparation. For stained specimens, image formation mainly arises from amplitude contrast. In this case the projections of the electrostatic density of the sample are proportional to the logarithm of the micrograph pixel values [220]. For nonstained specimens, image formation is mainly due to phase contrast which results from the quantum superposition of the crest of the single wave as it passes through the specimen [106]. In this case the micrograph is a projection of the specimen's electrostatic density, convolved with the inverse Fourier transform of the CTF, in which the CTF describes the imaging conditions and the TEM properties[10].

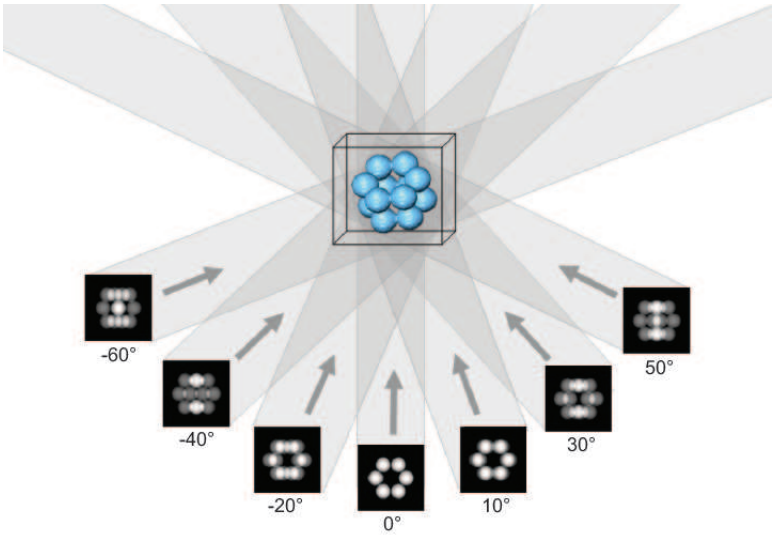

Figure 2.2: 3D reconstruction of an object from its projections by using the weighted-backprojection method. Original image courtesy of José-Jesús Fernández (University of Almeria). Reproduced with permission.

[9]In reality electrons travel along a curved helical orbit as they pass through the microscope column [48, 202].

[10]The optical system has to be modeled since it is the optics that converts the phase contrast to visible amplitude contrast.

2.4 Volume Computation

The two basic steps involved in the 3D reconstruction of an specimen from its projections are: (i) alignment of the different micrographs to a common coordinate system, and (ii) merging of the aligned micrographs into a tomogram.

(i) The most common alignment procedure employs fiducial markers[11] (typically colloidal gold), to keep track of small specimen movements within the image field [89, 202, 232, 236, 309]. Ideally, the method will be able to determine the angle of the tilt axis, lateral shifts, magnification changes, and image rotations, for it to accomplish an accurate alignment. The alignment model is then computed using least-square procedures.

(ii) The Fourier transform of a micrograph corresponds to a central slice in the 3D Fourier space of the sample being imaged (see Fig. 2.3). This is the basic rationale behind the recovering of 3D data from its projections. Most reconstruction algorithms are performed in the real space as opposed to the Fourier space, due to the notorious difficulties involved with the former approach. The most common 3D reconstruction method employed in ET is the weighted (or filtered) backprojection (WBD/FBP) [76, 139, 304, 306, 356]. This is a very simple, linear transformation approach [264, 354], in which the aligned micrographs are projected back to form a 3D reconstruction of the specimen. In this method, the weighting is performed in the Fourier space and the actual reconstruction is done in the real space [109]. Alternatives to the WBP/FBP method are the algebraic reconstruction technique (ART) [148, 225] also known as the Kaczmarz method, the simultaneous iterative reconstruction technique (SIRT) [138] also known as Landweber iteration, and the series expansion reconstruction

[11] Other approaches such as utilizing naturally existing features in the micrographs [50, 51] and cross-correlation functions between the various micrographs [123] are difficult to use in low-dose ET, due to the poor contrast and high noise level in the micrographs.

(SER) methods [209, 233]. ART and SIRT are iterative methods that are gaining in popularity as computationally faster implementations are being developed [110]. SER employs blob basis functions that provide the series expansion method with an implicit regularization mechanism which makes it well suited for noisy conditions [110, 113].

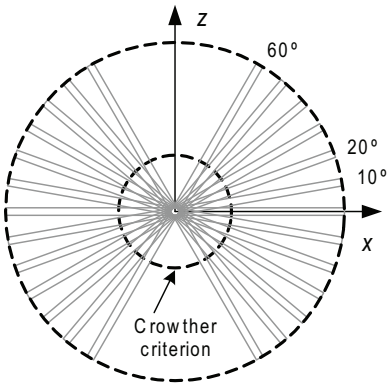

Figure 2.3: Each projection of an object with thickness h corresponds to a central slice of thickness $1/h$ in the Fourier space. Therefore, outside of the missing wedge, the 3D information of the object can be retrieved homogeneously up to a frequency limited by the Crowther criterion. Adapted from an original image by Anton Hillebrand (Max Planck Institute of Biochemistry). Reproduced with permission.

One of the principal limitations of all the 3D reconstruction algorithms in ET is the limited tilt range ($\pm 70°$). This is due to the design of the specimen holder[12] and leaves an unsampled wedge-shaped region in Fourier space ('missing-wedge'). When reconstructed, the missing-wedge causes nonisotropic resolution where objects appear elongated in the beam direction, and some structural elements are not resolved at all [220]. Some of these issues can be attenuated by double-tilt acquisition. This consists of two single-tilt series recording where the specimen is rotated by 90°, and allows sampling the structural components of the objects more isotropically. The procedure still leaves a pyramid-shaped region in Fourier space that remains unsampled, and

[12]The specimen holder that allows us to change the positioning of the specimen relative to the optical axis of the microscope is termed 'goniometer' [106].

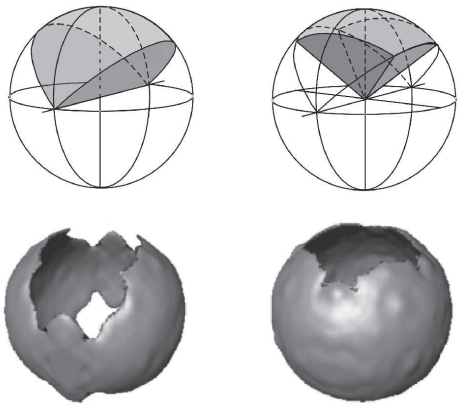

Figure 2.4: The upper illustrations represent the sectors in the Fourier domain that remain unsampled due to the limited tilt range, $\pm 70°$. In the case of the single-axis tilting (*left*), there is a 'missing wedge,' while in the case of the double-axis tilting (*right*), there is a 'missing pyramid.' The resulting missing information in real space is shown in the lower illustrations. Original image courtesy of Vladan Lučić (Max Planck Institute of Biochemistry). Reproduced with permission.

the SNR decreases to avoid damaging the samples with the longer exposure to the electron beams (see Fig. 2.4). Even in the case of double-tilt imaging, limitations on the range of the tilt angle still leads to severe ill-posedness for the inverse problem [61, 264, 280, 287, 300].

2.5 Image Analysis and Interpretation

The analysis and interpretation of tomograms require that the 3D image be decomposed into its structural components. This is usually accomplished via image segmentation and feature extraction. A manual assignment of features is the typical approach since, currently, there is no better judgement than the one done by the (trained) human eye [159, 167, 192, 212, 237]. Although, automated (or semi-automated) segmentation and feature extraction has the advantage of being faster and more objective [21, 120, 367]. The ability to perform efficient segmentation and feature extraction, either manual or automated, and subsequent visualization

and interpretation of the tomogram is hampered by the very low SNR. There have been many attempts during the last few years to address this limitation [117]. The simplest noise removal techniques use diverse linear filtering operations, such as low-pass filtering either in the real or the Fourier space. More sophisticated approaches employ techniques such as wavelet transformation [340], bilateral filtering [178], or anisotropic nonlinear diffusion [111, 119]. Anisotropic nonlinear diffusion is particularly useful when the enhancement of edges is desired. This is the topic of chapter 3. When the artificial enhancement of edges is to be avoided, the methods of choice are total variation-based noise removal models. We introduce this technique to image processing for ET in chapter 4.

2.6 Characterization of the Noise

2.6.1 Nature and Statistics of the Noise

In the electron detection process using a CCD camera in ET, there are at least two types of noise[13]: Poisson noise (predominantly multiplicative noise) and Gaussian noise (predominantly additive noise) [106, 410]. The shot noise in the original electron image[14], the shot noise of the dark current[15], and the CCD bias (gain[16] image) are assumed to follow Poisson's statistics [71, 175, 238, 394]. The CCD read out noise is assumed to be Gaussian distributed[17] [394, 410]. Both types of noise are considered

[13]For noise models that can be applied to more conventional CCD cameras the reader is referred to [162, 391].

[14]The shot noise that occurs in the scintillator once convolved with the PSF of the detector is called the 'Fano noise.'

[15]Dark currents are (spontaneous) thermally generated electrons in the CCD. This can be subtracted but the noise associated with dark currents remains [177].

[16]The gain of the camera is a ratio that relates the initial number of electrons in a pixel to the final number of counts reported by the camera software. The noise in the gain image introduces a systematic bias that can be treated as a systematic error and can be ignored (as a source of noise) for the purpose of image restoration [410].

[17]Alternatively, some authors prefer to approximate the read out Gaussian noise with variance σ^2 with a Poisson noise of mean σ^2, and treat it as an offset to the intensity [410].

as white noise[18] and the read out noise and the dark current noise are also considered independent from the illumination [394]. In the most general sense we can consider the recorded image as a combination of the original electron image and its interaction with the detector. Therefore, the recorded image is highly dependant on the detector's characteristics. In practice, this relationship results in a blurry and noisy image. For a linear detector, the recorded intensity u_0, at pixel $\mathbf{x} = (x, y)$, is proportional to the signal and plus the background [410] and can be cast as

$$u_0(\mathbf{x}) = L(\mathbf{x})\, F(\mathbf{x}) + B(\mathbf{x}) + N(\mathbf{x}, F), \tag{2.1}$$

where N is the noise introduced by the detector[19], L is the linear gain of the detector, and B is the background noise[20]. For a homogeneous detector the signal F is a convolution of the original electron image[21] and the PSF of the detector.

To the best of our knowledge, all the models employed in ET assume only additive stochasticity for the data, see *e.g.*, [122, 405]. This is a reasonable assumption when we are dealing with high counts. However, in cases when we have a low number of counts, such as in data from low-dose ET, more accurate models for the stochasticity of the data are required [106]. In low-dose ET, the Poisson stochasticity becomes the dominant degrading factor, challenging the applicability of the classic models that consider only additive noise [151, 152, 223, 236, 311, 405, 410]. The strong influence of the Poisson stochasticity in low-dose ET explains why some authors are starting to consider the degradation present in the micrographs as 'speckle noise.' It has been conjectured in [67] that the shot noise in ET presents "fluctuating gran-

[18] White noise is frequency independent in a wide interval of frequency [43].

[19] The noise performance of the detector is often characterized by the 'detector quantum efficiency' (DQE), which is the squared ratio of output SNR to input SNR [174].

[20] Background noise is a consequence of spurious events due to x-rays or cosmic rays to which the CCD is also sensitive.

[21] The original electron image is the quantum mechanical probability of detecting an electron at the position $\mathbf{x}$.

ular pattern very similar to that observed in speckle noise." The authors in [106] presented a survey of the recent approaches employed in combination with the reconstruction obtained from WBP/FBP in order to "remove speckle and enhance image features" [119, 163, 262, 361]. Images generated by coherent imaging systems are always degraded by speckle noise [134, 322, 397]. Coherent imaging systems are very common in many applications such as synthetic aperture radar (SAR), ultrasound, and laser imaging. As mentioned in subsection 2.3.1, FEG microscopes produce high spatial and temporal coherent electron beam [242]. However, there are two factors that lead to only partial coherence. The inelastic scattering of electrons gives rise to partial spatial coherence, while chromatic aberration of the objective lens produces partial temporal coherence. For more details on this topic the reader can consult [122, 161, 162, 250, 251, 288, 308, 335] and the references therein.

An *a priori* estimate of the data error introduced by the complex stochasticity involved in the ET processes is far from obvious. In subsection 2.6.2 we adopt a noise model that attempts to consider some of the elements from the nature of noise in ET discussed here. There are, though, many elements that are left out in the interest of tractability and that are problem specific. For example, in the study of mitochondria we usually deal with thick-section specimens. That gives rise to an anomaly referred to as 'variable defocus' in the specimen [122, 162, 388]. This simply refers to the fact that parts of the specimen (especially at high tilt angles), are in different focus with respect to the objective lens. Another issue that presents itself when dealing with 3D reconstructions in general, and 3D reconstructions from thick sections in particular, is the 'full tomographic problem' [106, 128, 172, 264, 285, 286]. In other words, the problem of quantifying the noise in the final 3D reconstruction, given what we know (or do not know) about the noise in the micrographs. In general, performing an image degradation analysis considering the true stochasticity of the data is still an

open question, mainly due to the severe ill-posedness of this problem.

2.6.2 Adopted Noise Model

In subsection 2.6.1 we discussed the nature of the noise in ET. The complex stochasticity of the signal is such that it is difficult to produce a standard by which noise can be measured [216, 238]. Nonetheless, we propose to model the noise in ET by a combination of additive and multiplicative noise,

$$u_0(\mathbf{x}) = m(\mathbf{x}) f(\mathbf{x}) + \eta(\mathbf{x}). \tag{2.2}$$

Eq. (2.2) is a simplified version of Eq. (2.1) where $N(\mathbf{x}, F)$ has been decomposed into its multiplicative and additive components, and the different terms are bundled together to form a simpler model. The down-side of adopting this over-simplified noise model is that we no longer have a clear understanding of the distributions involved in the model. What we do know is that the additive and multiplicative noise components are functions of the electron dose. When high electron dose is used the additive component of the noise becomes predominant, while for low-dose conditions the multiplicative noise prevails.

This noise model can also take into account other practical aspects of the image degradation in ET. For example, the PSF of the detector introduces some correlation among the data recorded at different pixels even though the count events at the scintillator and the pixels at the CCD are independent [106]. Also, when a number of images are combined to yield a 3D reconstruction, there is some form of averaging that causes the noise to be reduced [354]. Therefore, the original assumptions made in subsection 2.6.1 are difficult to propagate through the 3D reconstruction. In spite of these limitations, we can borrow some results from other imaging fields that can help us make reasonable assumptions.

For the case of low electron dose it is reasonable to assume that the signal is mainly corrupted by speckle-like degradation. Speckle can be either partially or fully developed depending on the scatter number density [1]. Fully developed speckle has the characteristics of random multiplicative noise [134, 147, 322, 368, 397]. Most researchers agree that the noise in a single image corrupted by speckle follows a negative exponential distribution [146, 147, 166, 352, 368]. When speckle is reduced by image integration, such as in multi-look averaging (SAR) (and perhaps image WBP/FBP in EM), the resultant speckle is characterized as following either a Gamma distribution [3, 98, 116, 146, 166, 352, 368] or a Log-normal distribution[22] [4, 134, 322]. In the case of multi-look images, it has been stated [134] that using either the Gamma distribution or the Log-normal distribution to model the speckle does not result in a significant difference in the filter performance.

Most of the multiplicative noise reduction techniques employ some variation of Oppenhein's homomorphic systems [275]. Oppenhein introduced the idea of a canonical form of a system comprising a point operation to convert the signal and noise combination to an additive one. Then, he applied a linear system to suppress the now additive noise, and finally an inverse point operation to return the processed signal and noise to the original intensity domain[23]. In the present, a number of methods (using this approach) exist to address the problem of speckle noise including median filtering [77, 136], temporal averaging [35, 134], geometry-based filtering [75], nonlinear multiscale filtering [408], adaptive speckle reduction [17, 115, 132, 198, 199, 204, 217, 263, 271], homomorphic Wiener filtering [10, 134, 135, 176], wavelet [133, 134, 154, 166, 203, 272, 317], and curvelet [316, 317, 338, 353].

However, care must be taken when applying approaches based on additive noise

[22] As the number of images integrated tends to infinity, the speckle intensity tends to follow a Gaussian distribution [13, 147].

[23] Cole [70] might have been the first to apply this methodology for image processing.

models directly to a log-transformed signal. The logarithmic transformation is a nonlinear operation that can completely change the statistics of the image [397]. This issue has been addressed by a few authors [168, 181, 397] and the probability density function, mean value, and variance that characterize the log-transformed speckle have been devised [397]. It has been also found that applying the logarithmic transformation to the signal perturbed by fully developed speckle is very close to Gaussian distribution[24] [1, 98, 155]. This implies, that after an image integration, the Log-normal distribution could be safely used to approximate the intensity distribution of the speckle [322].

The noise degradation of a multiplicative nature can be interpreted as each sample of the true signal being multiplied by a random noise element. A 3D tomogram can be represented as

$$u_0(\mathbf{x}) = m(\mathbf{x})\, f(\mathbf{x}),$$

where in this case $\mathbf{x} = (x, y, z)$, $u_0(\mathbf{x})$ is the observed degraded image, $f(\mathbf{x})$ is the true image, and $m(\mathbf{x})$ is the multiplicative noise with unit-mean following a Gamma (or Log-normal) probability distribution. Applying the natural logarithmic transform (homomorphic system) to the observed corrupted image we can write

$$\begin{aligned} \ln u_0(\mathbf{x}) &= \ln f(\mathbf{x}) + \ln m(\mathbf{x}) \\ &= \ln f(\mathbf{x}) + \bar{m}(\mathbf{x}). \end{aligned} \tag{2.3}$$

Adding and subtracting the mean of $\bar{m}$, $\mu_{\bar{m}}$, from the right-hand side of Eq. (2.3) we have

$$\ln u_0(\mathbf{x}) = \ln f(\mathbf{x}) + \mu_{\bar{m}} + \bar{m}(\mathbf{x}) - \mu_{\bar{m}},$$

which can be written as

$$\bar{u}_0(\mathbf{x}) = \bar{f}(\mathbf{x}) + \bar{\eta}(\mathbf{x}). \tag{2.4}$$

[24]It has been conjectured that the Gaussian distribution approximation can be also considered in the case of partially developed speckle [1, 98].

In Eq. (2.4), $\bar{\eta}(\mathbf{x})$ is a random zero-mean noise process [350] (very close to Gaussian distribution [1, 98, 155]) and $\bar{f}(\mathbf{x}) = \ln f(\mathbf{x}) + \mu_{\bar{m}}$. The variance and mean of $\bar{m}$ have been derived in [397] for an integer number of looks, L:

$$\mu_{\bar{m}} = -\gamma_{EM} - \ln(L) + \sum_{k=1}^{L-1} \frac{1}{k}, \tag{2.5}$$

$$\sigma_{\bar{m}}^2 = \frac{\pi^2}{6} - \sum_{k=1}^{L-1} \frac{1}{k^2}. \tag{2.6}$$

In Eq. (2.5), $\gamma_{EM} = 0.577215664901...$ is the Euler-Mascheroni constant. We will make use of the assumptions considered in this subsection when presenting one of the total variation-based noise removal methods in chapter 4.

2.7 Experimental Materials and Methods

The electron tomogram employed in our experiments corresponds to a HeLa cell[25] and was obtained from a 250 nm semi-thick section across a mitochondrion expressing cytochrome c-GFP. In the interest of research not discussed here, apoptosis was induced in the mitochondria with 100μM etoposide for 15 hours. The imaging occurred before the release of cytochrome c or loss of membrane potential allowing the maintenance of normal mitochondrion profiles; however, the treatment caused elongation of the crista junctions. The use of a semi-thick section is advantageous because it allows accurate depiction of the inner membrane topology of the mitochondrion.

The microscope used was the FEI Tecnai 12 transmission electron microscope with magnification set at 11000×. The EM tomography single-tilt series 3D reconstruction was obtained from the semi-thick sample by progressively tilting the specimen and recording images using a Teitz 214 digital camera with an image pixel size of 1.27 nm.

[25] A HeLa cell is an immortal cell line used in medical research. The cell line was derived from cervical cancer cells taken from Henrietta Lacks, who died from cancer on October 4, 1951 [348].

The tilting was conducted in increments of 2 degrees over an angular range of $\pm 60°$; the angular range is limited by the geometry of the apparatus that holds the sample. Once the tilt-series was collected on the digital camera, the IMOD Software Suite [192] was used to process the images and obtain the 3D reconstruction of the electron tomogram.

2.8 Concluding Remarks

The main procedures used to reconstruct, model, and interpret large biological material volumes via ET are subject to noise and artifacts. Accurate modeling of every image degradation introduced during the ET processes is a daunting task. From an image processing standpoint, we are most interested in the interaction between the electron image and the detector, which generates the recorded image. Even within this narrower scope, the noise introduced by the complex stochasticity involved in the process is far from obvious. We propose to model the noise in ET by a combination of additive and multiplicative noise, $u_0(\mathbf{x}) = m(\mathbf{x}) f(\mathbf{x}) + \eta(\mathbf{x})$. For high counts, the image is predominantly perturbed by additive noise. In low-dose ET, it is more accurate to assume that the image is degraded by multiplicative noise. The simplicity of this noise model for ET makes it very attractive for employing basic techniques, adapted from classic and well established PDE-based image processing methodologies.

Chapter 3

Anisotropic Nonlinear Diffusion Models

3.1 Introduction

Analysis of image features in early vision presents two almost mutually exclusive requirements. On the one hand, it is desirable to smooth homogeneous regions of the image, and on the other hand, we wish to preserve the location of the object boundaries (edges) accurately. In an effort to achieve both goals, the classic multiscale analysis theory due to Marr and Hildreth [229], later formalized by Witkin [392], Koenderink [189] and Canny [60], uses a low-pass filtering obtained by convolving the image with Gaussian kernels of increasing variance, then traces back the position of the edges from finer scales. Koenderink [189] soon realized that the convolution of the image with a Gaussian kernel at each scale is equivalent to the solution of the heat equation with the image as initial state[1]. Thus, given the observed (noisy) image $u_0(\mathbf{x})$, where $\mathbf{x} = (x, y)$ denotes space coordinates, the scale-space analysis associated

[1]For a 'hand-waving' proof of this assertion please refer to Appendix B.

with u_0 consists in solving the system[2]

$$u_t - \nabla^2 u = 0, \tag{3.1}$$

for $t > 0$, on an infinite domain Ω, and initial condition $u(\mathbf{x}, 0) = u_0(\mathbf{x})$. This system has a unique solution [373]

$$u(\mathbf{x}, t) = \begin{cases} u_0(\mathbf{x}) & t = 0 \\ \left(G_{\sqrt{2t}} * u_0\right)(\mathbf{x}) & t > 0, \end{cases} \tag{3.2}$$

provided that (i) the function satisfies $\|u(\mathbf{x}, t)\| \leq M \exp\left(a |\mathbf{x}|^2\right)$, $M > 0$, (ii) it depends continuously on the initial condition u_0 with respect to $\|\cdot\|_{L^\infty(\mathbb{R}^2)}$, and (iii) it meets the maximum-minimum principle $\inf_{\mathbb{R}^2} u_0 \leqslant u(\mathbf{x}, t) \leqslant \sup_{\mathbb{R}^2} u_0$ on $\mathbb{R}^2 \times [0, \infty)$. In Eq. (3.2), $G_{\sqrt{2t}}$ is a Gaussian kernel of width $\sqrt{2t}$, and '$*$' indicates convolution. For tracing back the position of the edges, the point $\mathbf{x}$ is an edge for the scale t, in places where[3] $|\nabla u(\mathbf{x}, t)|$ is large and $\nabla^2 u(\mathbf{x}, t)$ changes sign.

The simplicity and effectiveness of the Gaussian smoothing makes it an attractive tool for image noise removal. However, it also presents at least a couple of serious drawbacks: (i) Gaussian smoothing does not only smooth the noise but it also smoothes everything else along with it, and (ii) Gaussian smoothing tends to dislocate edges when we move from finer to coarser scale [392, 393]. Most of the shortcomings of linear diffusion processes can be attenuated through nonlinear diffusion models.

[2]Unless stated otherwise, $\nabla\cdot$ and $\nabla^2\cdot$ involve derivatives with respect to the spatial variables (x, y). We are adopting the notation where $u_t \equiv \partial u/\partial t$, $u_x \equiv \partial u/\partial x$, $u_y \equiv \partial u/\partial y$, represent the partial derivatives of u with respect to time (scale) and spatial variables (x, y), respectively.

[3]We are adopting the notation where $|\nabla u| \equiv \sqrt{u_x^2 + u_y^2}$ represents the magnitude of the gradient of u at point (x, y).

3.2 Nonlinear Diffusion Models in Image Processing

3.2.1 Inhomogeneous Nonlinear Diffusion

Nonlinear diffusion is a very powerful image processing technique used for the reduction of noise and enhancement of structural features. It was first introduced in the context of image processing by Perona and Malik [294], as an attempt to overcome the shortcomings of linear diffusion processes, namely the blurring of edges and other localization problems. Their model accomplishes this by applying a process that reduces the diffusivity in areas of the image with higher likelihood of belonging to edges. This likelihood is measured by a function of the (current[4]) local gradient $|\nabla u|$. Their model can be written as

$$u_t - \nabla \cdot \left(g\left(|\nabla u|^2 \right) \cdot \nabla u \right) = 0, \tag{3.3}$$

for $t > 0$, on a closed domain Ω, with the observed image as initial condition, $u(\mathbf{x}, 0) = u_0(\mathbf{x})$, and homogeneous Neumann boundary conditions[5], $\langle g \cdot \nabla u, \mathbf{n} \rangle = 0$, on the boundary $\partial\Omega$. In this model the diffusivity has to be such that $g\left(|\nabla u|^2 \right) \to 0$ when $|\nabla u| \to \infty$, and $g\left(|\nabla u|^2 \right) \to 1$ when $|\nabla u| \to 0$. One of the diffusivities Perona and Malik proposed is (see Fig. 3.1)

$$g\left(|\nabla u|^2 \right) = \frac{1}{1 + |\nabla u|^2 / \lambda^2}, \tag{3.4}$$

where $\lambda > 0$ is a threshold (contrast) parameter that separates forward ($|\nabla u| \leqslant \lambda$, low contrast) and backward ($|\nabla u| > \lambda$, high contrast) diffusion areas [373]. Their model accomplishes the long sought effect of blurring small fluctuations (possible

[4]Fritsch, Pizer and Coggins [130] and Fritsch [129] included *a priori* information about the image in the form of an edge detector based on $|\nabla u_0|$.

[5]We are adopting the notation where $\mathbf{n}$ denotes the outward normal to the domain's boundary $\partial\Omega$, and $\langle g \cdot \nabla u, \mathbf{n} \rangle$ indicates the inner product $\int_{\partial\Omega} (g \cdot \nabla u) \cdot \mathbf{n}\, ds$.

noise) while preserving (and enhancing) edges. The results obtained by Perona and Malik were visually very impressive.

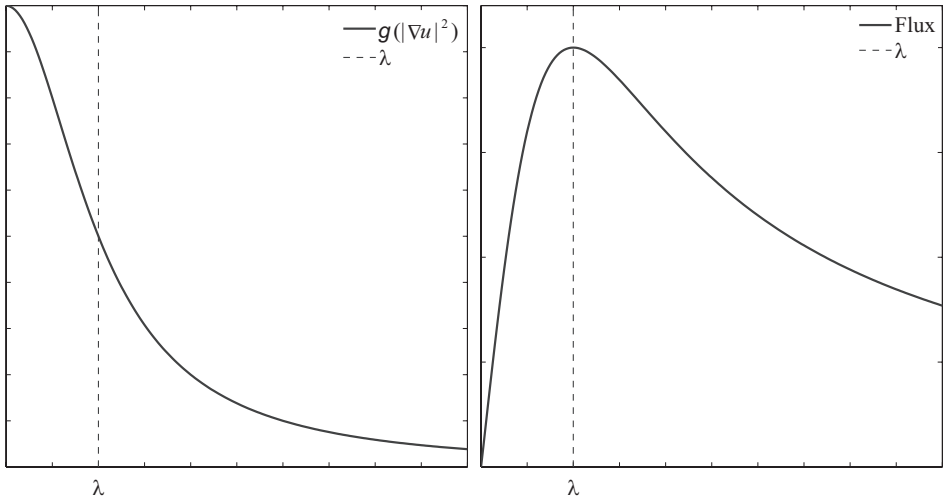

Figure 3.1: (*left*) Behavior of the Perona-Malik diffusivity, Eq. (3.4), for the parameter $\lambda = 0.4$. The diffusivity is such that $0 \leq g\left(|\nabla u|^2\right) \leq 1$ and it goes to zero very rapidly as $|\nabla u|$ increases. In practice, the higher the gradient (*i.e.*, near edges), the lower the diffusion for all values of λ, and the higher the parameter λ, the higher the diffusivity for the same gradient. (*right*) The contrast parameter, λ, separates forward ($|\nabla u| \leqslant \lambda$, low contrast) and backward ($|\nabla u| > \lambda$, high contrast) diffusion areas.

Notwithstanding the practical success of the Perona-Malik model, it presents some serious theoretical problems: (i) None of the classic well-posedness frameworks is applicable to the Perona-Malik model, *i.e.*, we can not ensure well-posedness results [268, 383]; (ii) Uniqueness and stability with respect to the initial image should not be expected, *i.e.*, solvability is a difficult problem, in general [62, 169, 170, 185, 295]; (iii) The regularizing effect of the numerical discretization plays too much of an important role in the solution [36, 131]. The latter is perhaps the key element in the success or failure of the model. Most practical applications work very well provided that the numerical schemes stabilize the process through some implicit (or explicit) regularization.

This observation motivated an enormous amount of research towards the incorporation of the regularization directly into the PDE, to avoid excessive reliance on the numerical schemes [62, 268]. A variety of spatial, spatio-temporal, and temporal regularization procedures have been proposed over the years [11, 27, 62, 74, 211, 268, 369, 373, 379, 385]. We present here only the works that serve as background for our proposed methods. The one model that has attracted much attention within the image processing community is the mathematically sound formulation due to Catté, Lions, Morel and Coll [62]. They proposed to replace the diffusivity $g\left(|\nabla u|^2\right)$ of the Perona-Malik model by a slight variation, $g\left(|\nabla u_\sigma|^2\right)$, with $u_\sigma = G_\sigma * u$, where G_σ is a smooth kernel (Gaussian). Their model can be written

$$u_t - \nabla \cdot \left(g\left(|\nabla u_\sigma|^2\right) \cdot \nabla u\right) = 0, \tag{3.5}$$

for $t > 0$, on a closed domain Ω, with the observed image as initial condition, $u\left(\mathbf{x}, 0\right) = u_0\left(\mathbf{x}\right)$, and homogeneous Neumann boundary conditions, $\langle g \cdot \nabla u, \mathbf{n} \rangle = 0$, on the boundary $\partial\Omega$. We should note that this spatial regularization model belongs to a class of well-posed problems[6], and that its successful implementation is contingent on the choosing of an appropriate value for the additional regularization parameter σ. Whitaker and Pizer [385] and Li and Chen [211] suggested making the parameters σ and λ time-dependent, and Benhamouda [36] performed a systematic study of the influence of these parameters for the one-dimensional (1D) case.

As for the diffusivity $g\left(|\nabla u_\sigma|^2\right)$, it has to be chosen as a (rapidly) decreasing function of the edge detector $|\nabla u_\sigma|$. Weickert [379] proposed to use (see Fig. 3.2)

$$g\left(|\nabla u_\sigma|^2\right) = \begin{cases} 1 & |\nabla u_\sigma| = 0 \\ 1 - \exp\left(\frac{-c}{\left(|\nabla u_\sigma|/\lambda\right)^8}\right) & |\nabla u_\sigma| > 0, \end{cases} \tag{3.6}$$

for which we can ensure that the flux increases for $|\nabla u_\sigma| \leq \lambda$ and decreases for

[6]Existence, uniqueness, and regularity of a solution for $\sigma > 0$ were proven in [62].

$|\nabla u_\sigma| > \lambda$, by choosing $c \approx 3.31488$. After some time this filter creates segmentation-like results which are piecewise almost constant [378]. For $t \to \infty$, however, the image becomes completely flat [375]. Well-posedness results for this filter can be found in [62, 375], and a scale-space interpretation in terms of an extremum principle as well as decreasing variance, decreasing energy, and increasing entropy is given in [375].

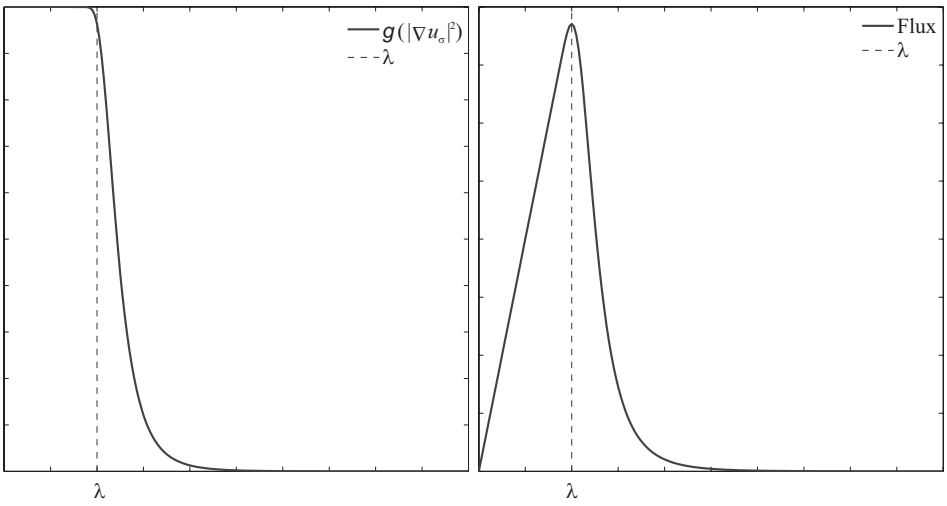

Figure 3.2: (*left*) Behavior of the Weickert diffusivity, Eq. (3.6), for the parameter $\lambda = 0.4$. The diffusivity is such that $0 \leq g\left(|\nabla u|^2\right) \leq 1$ and it goes to zero very rapidly when $|\nabla u| > \lambda$. (*right*) The contrast parameter, λ, separates forward ($|\nabla u| \leqslant \lambda$, low contrast) and backward ($|\nabla u| > \lambda$, high contrast) diffusion areas.

Another interesting variation to the Perona-Malik model has been proposed by Nordström [269], who considered diffusion-reaction methods for the restoration of degraded images. Such an approach leads to Euler-Lagrange equations of the form

$$u_t - \nabla \cdot \left(g\left(|\nabla u_\sigma|^2\right) \cdot \nabla u\right) = \beta\left(u - u_0\right), \tag{3.7}$$

for $t > 0$, on a closed domain Ω, with the observed image as initial condition, $u\left(\mathbf{x}, 0\right) = u_0\left(\mathbf{x}\right)$, and homogeneous Neumann boundary conditions, $\langle g \cdot \nabla u, \mathbf{n} \rangle = 0$, on the boundary $\partial\Omega$. This is identical to the models we have been considering but with

an additional bias term $\beta(u - u_0)$. In principle, the bias term should spare the user from choosing a stopping time[7], by the choosing of an additional free parameter β. This type of diffusion-reaction models has been studied further and improved upon in [73, 74, 137, 303, 320].

3.2.2 Inhomogeneous Nonlinear Diffusion and Bilateral Filter Model

In the Catté-Lions-Morel-Coll model, Eq. (3.5), the diffusivity term inside the divergence, $g\left(|\nabla u_\sigma|^2\right)$, is a function of the gradient of the solution of the heat equation at scale σ, with $u(\mathbf{x}, 0)$ as the initial state. Consequently, it is equivalent to using an estimate of the gradient of u at point $\mathbf{x}$, obtained by the classic scale-space theory [11]. In practice, after the Gaussian (domain) filtering is performed, the term $g\left(|\nabla u_\sigma|^2\right)$ allows for the detection of the positions of the main edges and prevents excessive diffusion at these locations. By the same token, the small fluctuations (noise) will be sufficiently smooth and not be mistaken for edges, and can be diffused away.

In previous work [33] we proposed using a refined estimate of the gradient of u at point $\mathbf{x}$, obtained by applying a bilateral filter (BF) in place of the Gaussian kernel. Bilateral filtering is a technique for smoothing images while preserving edges. The first application of this method is attributed to Aurich and Weule [15], and it was subsequently rediscovered by Smith and Brady [329] and Tomasi and Manduchi [349]. Since its introduction, the bilateral filter has been successfully employed in various contexts [9, 18, 37, 97, 100, 102, 214, 274, 298, 307, 390]. The bilateral filter's characteristics and behavior have been the subjects of extensive theoretical studies that have made bilateral filtering a fairly well understood process [25, 26, 58, 97, 101, 256, 283, 330, 357, 358]. The basic idea underlying bilateral filtering is to combine

[7] In practice, the bias term forces the steady-state solution to stay close to the observed image.

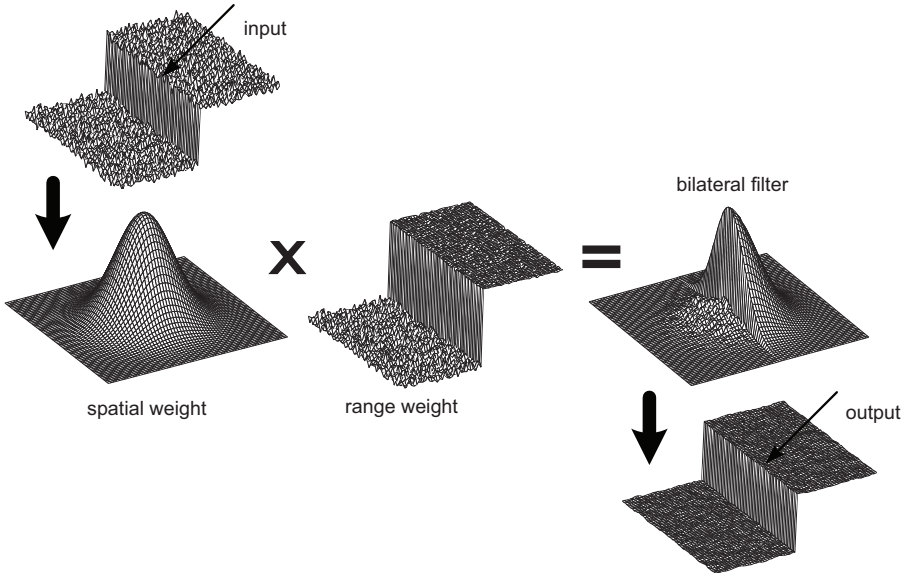

Figure 3.3: In the bilateral filtering each pixel is replaced by a weighted average of its neighboring pixels. Each neighboring pixel is weighted by a spatial component that penalizes distant pixels, and a range component that penalizes pixels with disparate intensities. Both components are multiplied to obtain a kernel that ensures the contribution of only nearby analogous pixels. (A similar image originally appeared in [97].)

domain and range filtering, thereby enforcing both geometric and photometric locality (see Fig. 3.3). The model can be expressed as

$$G_{bf} * u(\mathbf{x}) = \frac{1}{W(\mathbf{x})} \int_{\Omega} G_{\sigma_d}(\xi, \mathbf{x})\, G_{\sigma_r}(u(\xi), u(\mathbf{x}))\, u(\xi)\, d\xi, \tag{3.8}$$

with the normalization constant

$$W(\mathbf{x}) = \int_{\Omega} G_{\sigma_d}(\xi, \mathbf{x})\, G_{\sigma_r}(u(\xi), u(\mathbf{x}))\, d\xi. \tag{3.9}$$

Typically, G_{σ_d} will be a spatial Gaussian that decreases the influence of distant pixels, while G_{σ_r} will be a range Gaussian that decreases the influence of pixels $u(\xi)$, with intensity values that are very different from those of $u(\mathbf{x})$, *e.g.*,

$$G_{\sigma_d} = \exp\left(-\frac{|\xi - \mathbf{x}|^2}{2\sigma_d^2}\right), \qquad G_{\sigma_r} = \exp\left(-\frac{|u(\xi) - u(\mathbf{x})|^2}{2\sigma_r^2}\right). \tag{3.10}$$

Parameters σ_d and σ_r dictate the amount of filtering applied in the domain and the range of the image, respectively. This filtering technique, as presented thus far, has the possible objection that it might consist of an expensive proposition. Fortunately, several authors have addressed this limitation and devised very efficient implementations of the method [68, 283, 299, 384]. In our application we use the fast approximation due to Paris and Durand [283] which employs downsampling in the domain and range, which achieves important acceleration of the bilateral filtering.

The proposed model is therefore

$$\begin{aligned} &u_t - \nabla \cdot \left(g\left(|\nabla u_{bf}|^2 \right) \cdot \nabla u \right) = 0, \qquad \text{on } \Omega \times [0, \infty), \\ &u(\mathbf{x}, 0) = u_0(\mathbf{x}), \qquad \text{on } \Omega, \\ &\langle g \cdot \nabla u, \mathbf{n} \rangle = 0, \qquad \text{on } \partial\Omega \times (0, \infty), \end{aligned} \tag{3.11}$$

where $u_{bf} = G_{bf} * u$ is the domain- and range-filtered image, and $g\left(|\nabla u_{bf}|^2\right) \geqslant 0$ is a smooth nonincreasing function with $g\left(|\nabla u_{bf}|^2\right) \to 1$ as $|\nabla u_{bf}| \to 0$, and $g\left(|\nabla u_{bf}|^2\right)$ tending to zero at infinity. We should recall here that the main purpose of the function g is to provide 'intelligent' smoothing. It should not only inhibit diffusion at edges and allow it far from them, but it should also precisely locate the position of the main edges. By design, this is exactly what bilateral filtering accomplishes. It provides image smoothing with strict preservation of the edges without artificially enhancing them.

The practical success of the proposed model has its roots in the connection that exists between bilateral filtering and the Perona-Malik-based methods. Buades, Coll and Morel [59] have established the existing link between bilateral filtering and well-known PDE models such as the heat equation and the Perona-Malik equation. They have proven that for small neighborhoods, bilateral filtering using a box function as spatial weight, asymptotically behaves as the Perona-Malik model. In a discrete setting, Durand and Dorsey [97] have shown that the bilateral filter, if constrained to the

four neighbors of each pixel, corresponds to a discrete version of the Perona-Malik filter. Subsequently, Barash [25] used adaptive smoothing as a link between anisotropic diffusion and bilateral filtering, each of which can be viewed as a generalization of the former; while Elad [101] and Barash and Comaniciu [26] have shown that bilateral filtering is equivalent to a sum of several Perona-Malik filters at different scales.

3.2.3 Numerical Experiments for the Inhomogeneous Nonlinear Diffusion and Bilateral Filter Model

In order to compare the performance of the proposed model we implemented the three models below using finite differencing, and a simple performance measure based on the correlation between the noise-free image and the three filtered images[8]. Model 1 is the classic Perona-Malik model, Eq. (3.3),

$$\begin{aligned}
&u_t - \nabla \cdot \left(g\left(|\nabla u|^2 \right) \cdot \nabla u \right) = 0, \qquad \text{on } \Omega \times [0, \infty), \\
&u(\mathbf{x}, 0) = u_0(\mathbf{x}), \qquad \text{on } \Omega, \\
&\langle g \cdot \nabla u, \mathbf{n} \rangle = 0, \qquad \text{on } \partial\Omega \times (0, \infty), \\
&g\left(|\nabla u|^2 \right) = \frac{1}{1 + |\nabla u|^2 / \lambda^2}, \qquad \lambda = 10^{-2}.
\end{aligned} \tag{3.12}$$

The parameter $\lambda = 10^{-2}$ was estimated as an average of the 'robust scale' proposed in [41, 42], using the initial state of the images employed in our tests.

Model 2 is the Perona-Malik variant by Catté, Lions, Morel and Coll, Eq. (3.5),

$$\begin{aligned}
&u_t - \nabla \cdot \left(g\left(|\nabla u_\sigma|^2 \right) \cdot \nabla u \right) = 0, \qquad \text{on } \Omega \times [0, \infty), \\
&u(\mathbf{x}, 0) = u_0(\mathbf{x}), \qquad \text{on } \Omega, \\
&\langle g \cdot \nabla u, \mathbf{n} \rangle = 0, \qquad \text{on } \partial\Omega \times (0, \infty), \\
&g\left(|\nabla u_\sigma|^2 \right) = \frac{1}{1 + |\nabla u_\sigma|^2 / \lambda^2}, \qquad \lambda = 10^{-2}, \\
&u_\sigma = G_\sigma * u, \qquad \sigma = 1.
\end{aligned} \tag{3.13}$$

[8] We refer the reader to chapter 5 for a description of the algorithms to implement these models.

It has been shown [253] that $\sigma = 1$ is sufficient for a large interval of noise variances, provided that the noise in neighboring pixels is uncorrelated and that the grid size is one.

Model 3 is the proposed model, Eq. (3.11),

$$
\begin{aligned}
& u_t - \nabla \cdot \left(g\left(\left| \nabla u_{bf} \right|^2 \right) \cdot \nabla u \right) = 0, \qquad \text{on } \Omega \times [\,0, \infty), \\
& u\left(\mathbf{x}, 0\right) = u_0\left(\mathbf{x}\right), \qquad \text{on } \Omega, \\
& \langle g \cdot \nabla u, \mathbf{n} \rangle = 0, \qquad \text{on } \partial\Omega \times (0, \infty), \\
& g\left(\left| \nabla u_{bf} \right|^2 \right) = \frac{1}{1 + \left| \nabla u_{bf} \right|^2 / \lambda^2}, \qquad \lambda = 10^{-2}, \\
& u_{bf} = G_{bf} * u, \qquad \sigma_d = 3, \qquad \sigma_r = 10^{-2}.
\end{aligned}
\tag{3.14}
$$

The parameters σ_d and σ_r are chosen according to the desired amount of low-pass filtering and desired amount of combination of pixel values, respectively [349]. We loosely followed the recommendations given in [214] for choosing σ_d, and the ones in [284] for choosing σ_r. They give us a compact kernel that allows a very fast execution of the bilateral filtering.

The experiment consisted in running the three models using an explicit Euler method with a time step[9] of $\delta t = 10^{-2}$, and trying to restore the noise-free image, f, that has been perturbed by additive Gaussian white noise. Figs. 3.4, 3.6, 3.8, 3.10, and 3.12 show the images of Lena, the Clown, the Boats, the Baboon, and the Cameraman, respectively, both the noise-free and noisy images after perturbing them with Gaussian white noise of zero mean and variance 0.01. These are benchmark images that will be used throughout this work in comparative experiments. In the experiment, the three models were run for 50 iterations and the correlation coefficient between the noise-free image and each of the filtered images was measured at each

[9]Weickert, Romeny, and Viergever [381] have shown that for explicit discretization schemes, the stability condition (assuming $\delta \mathbf{x} = 1$ and $\forall s : g\left(s\right) \leqslant 1$) is $\delta t < 1/(2d)$, with d being the number of dimensions of the data, which for a 2D image $d = 2$.

iteration. For every case, we observe that the best image restored by the proposed model is closer to the noise-free image than the best images restored by the other two models tested (see Figs. 3.5, 3.7, 3.9, 3.11 and 3.13 and table 3.1). We can also observe that the proposed model performs 'in between' the other two models in terms of speed of restoration. The Catté-Lions-Morel-Coll model accomplishes the fastest restoration, *i.e.*, it attains its best restored image in fewer iterations than the other two methods. The classic Perona-Malik model achieves a better restoration if we were to iterate beyond the optimal stopping times of the three models, *i.e.*, reaching 50 iterations in this case. Lastly, in order for any of the three models to accomplish its best possible restoration, we have to be able to stop the diffusion process at the peak of its performance, in the absence of the noise-free image. In general, this remains an open problem. In subsection 3.2.4 we propose a procedure that works very well with all the models considered in this work.

Table 3.1: Similarity Performance by Model

Experiment	Perona-Malik	Catté *et al.*	Bazán-Blomgren
Lena	0.9584	0.9556	0.9593
the Clown	0.9763	0.9762	0.9771
the Boats	0.9537	0.9498	0.9549
the Baboon	0.8979	0.8947	0.8992
the Cameraman	0.9785	0.9736	0.9795

Figure 3.4: (*left to right*) Noise-free image of Lena along with the noisy image of Lena which has been perturbed by Gaussian white noise with zero mean and variance 0.01. The correlation coefficient between the noise-free image and the noisy image, corr (f, u_0), is 0.8661.

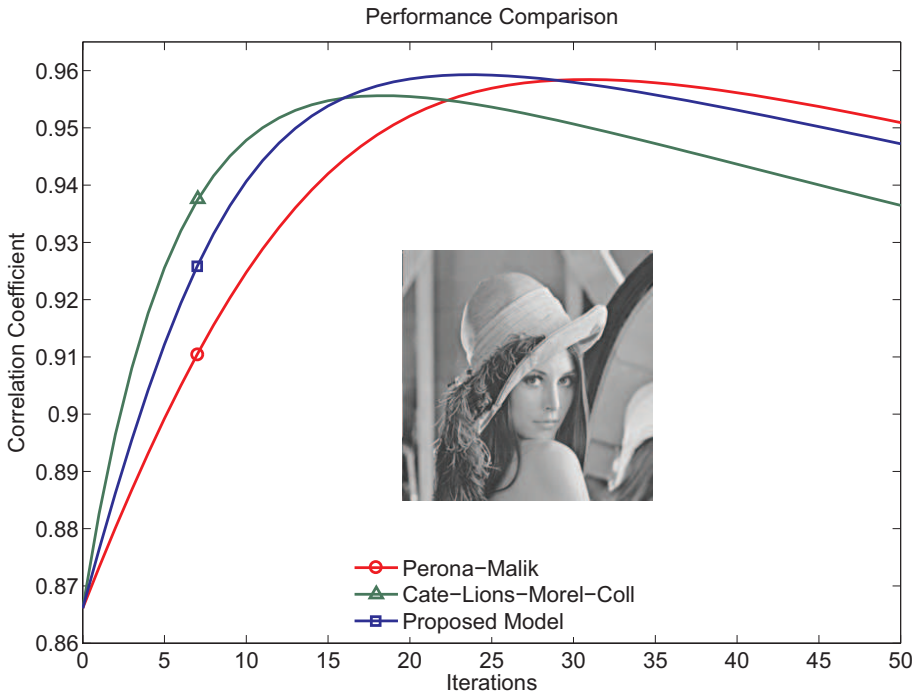

Figure 3.5: Correlation coefficient between the noise-free image of Lena and the filtered image of Lena at each iteration, along with the noise-free image of Lena. The maximum value of the correlation coefficient for each model is as follows: Perona-Malik, 0.9584; Catté-Lions-Morel-Coll, 0.9556; Proposed Model, 0.9593.

Figure 3.6: (*left to right*) Noise-free image of the Clown along with the noisy image of the Clown which has been perturbed by Gaussian white noise with zero mean and variance 0.01. The correlation coefficient between the noise-free image and the noisy image, corr (f, u_0), is 0.9301.

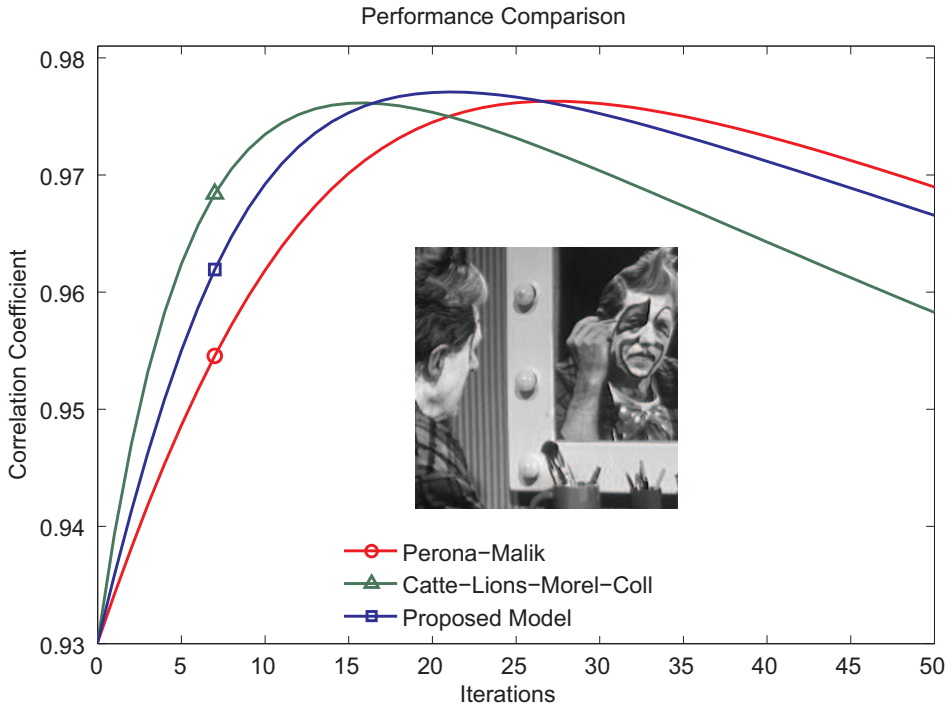

Figure 3.7: Correlation coefficient between the noise-free image of the Clown and the filtered image of the Clown at each iteration, along with the noise-free image of the Clown. The maximum value of the correlation coefficient for each model is as follows: Perona-Malik, 0.9763; Catté-Lions-Morel-Coll, 0.9762; Proposed Model, 0.9771.

Figure 3.8: (*left to right*) Noise-free image of the Boats along with the noisy image of the Boats which has been perturbed by Gaussian white noise with zero mean and variance 0.01. The correlation coefficient between the noise-free image and the noisy image, corr (f, u_0), is 0.8692.

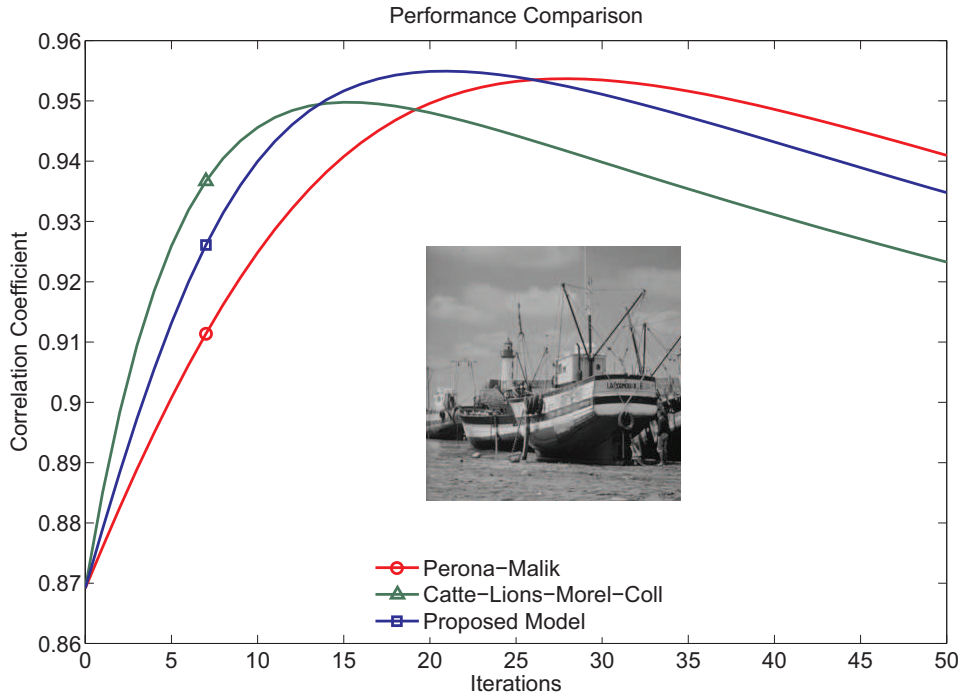

Figure 3.9: Correlation coefficient between the noise-free image of the Boats and the filtered image of the Boats at each iteration, along with the noise-free image of the Boats. The maximum value of the correlation coefficient for each model is as follows: Perona-Malik, 0.9537; Catté-Lions-Morel-Coll, 0.9498; Proposed Model, 0.9549.

Figure 3.10: (*left to right*) Noise-free image of the Baboon along with the noisy image of the Baboon which has been perturbed by Gaussian white noise with zero mean and variance 0.01. The correlation coefficient between the noise-free image and the noisy image, corr (f, u_0), is 0.8381.

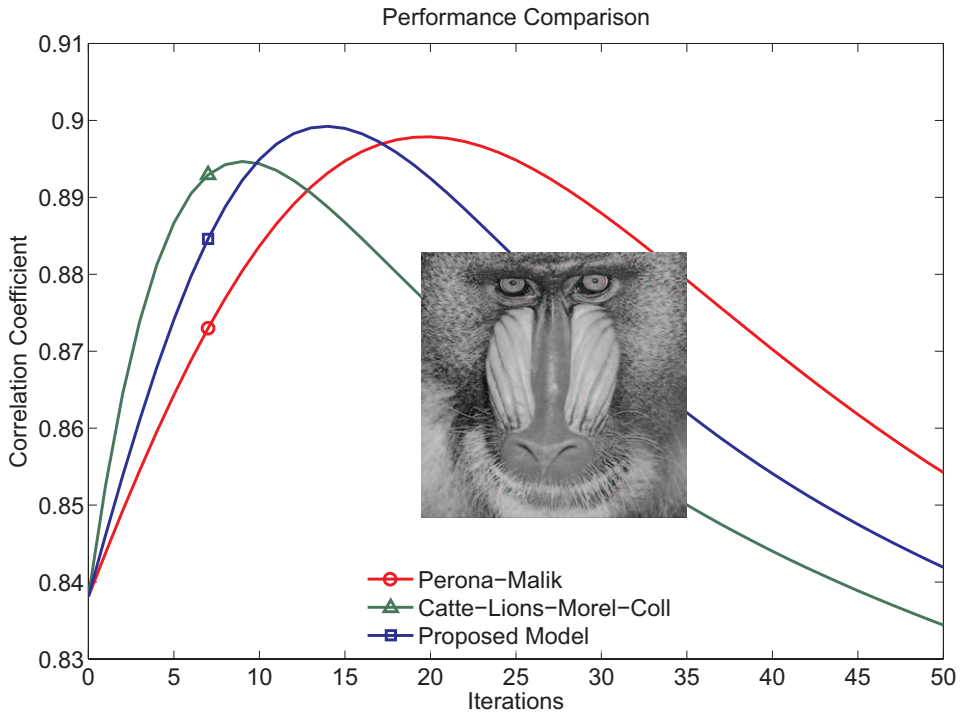

Figure 3.11: Correlation coefficient between the noise-free image of the Baboon and the filtered image of the Baboon at each iteration, along with the noise-free image of the Baboon. The maximum value of the correlation coefficient for each model is as follows: Perona-Malik, 0.8979; Catté-Lions-Morel-Coll, 0.8947; Proposed Model, 0.8992.

Figure 3.12: (*left to right*) Noise-free image of the Cameraman along with the noisy image of the Cameraman which has been perturbed by Gaussian white noise with zero mean and variance 0.01. The correlation coefficient between the noise-free image and the noisy image, corr (f, u_0), is 0.9280.

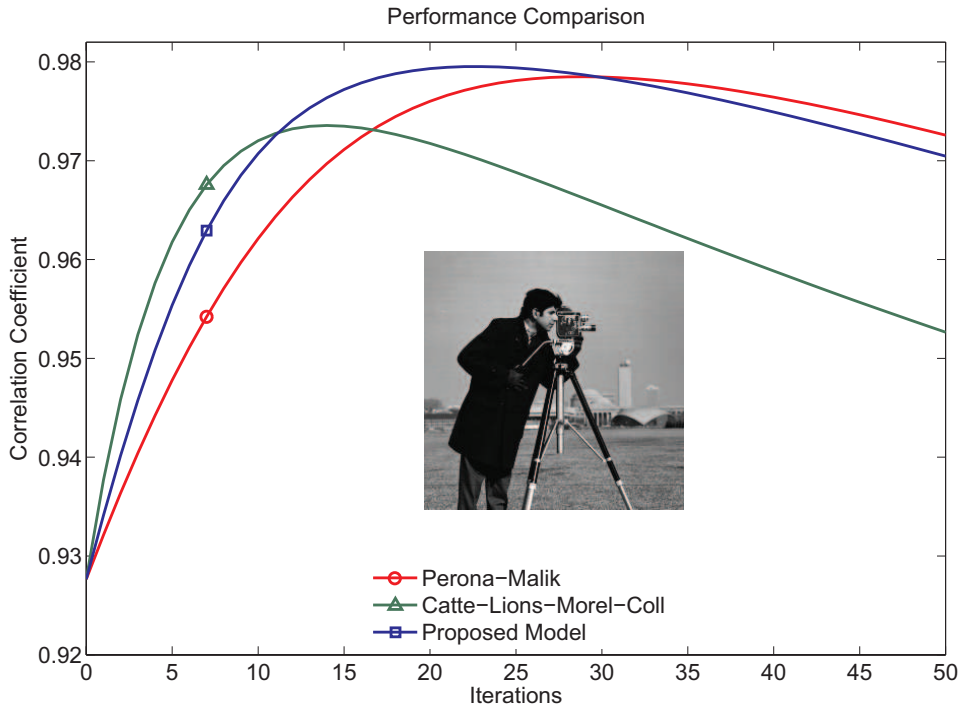

Figure 3.13: Correlation coefficient between the noise-free image of the Cameraman and the filtered image of the Cameraman at each iteration, along with the noise-free image of the Cameraman. The maximum value of the correlation coefficient for each model is as follows: Perona-Malik, 0.9785; Catté-Lions-Morel-Coll, 0.9736; Proposed Model, 0.9795.

3.2.4 Diffusion Stopping Criterion

Determining when the diffusion process should be stopped is crucial for obtaining a good image restoration. Several authors have addressed this issue in the past in an attempt to devise an optimal stopping criterion. Sporring and Weickert [337] focused on the maximum entropy change by scale to estimate the size of image structures. They argued that the minimum change by scale indicates especially stable scales with respect to evolution time, and conjectured that these scales could be good candidates for stopping times in nonlinear diffusion processes. Weickert [377] also pointed out that the monotonically decreasing 'relative variance,' $0 \leqslant \mathrm{var}\,(u)/\mathrm{var}\,(u_0) \leqslant 1$, could be used to measure the distance of u from the initial state u_0 and, by prescribing an appropriate value for the relative variance, it can constitute a good criterion for stopping the nonlinear diffusion.

Dolcetta and Ferretti [92] formulated a stopping criterion within the framework of optimal control theory. They considered the minimization of the performance index

$$E\,(t) = \int_0^t (E_c + E_\alpha)\, dt,$$

where E_c is the computing cost and E_α is the stopping cost, which encourages diffusion for small values of the scale factor. The authors in [92] argued that a careful balancing of the two terms is necessary for achieving good results, and suggested to take $E_c = c$ and $E_\alpha = -\left(\int_\Omega |u - u_0|^2\, d\mathbf{x}\right)^{\alpha/2}$, for some positive constants c and α. Mrázek [254] developed a new interesting time-selection strategy based on the correlation between the signal and the noise. He argued that, if the noise-free image and the noise were uncorrelated, it is appropriate to require that their artificial substitutes, u and $(u_0 - u)$, share the same property, and select the stopping time such that $T = \arg\min_t \mathrm{corr}\,(u_0 - u, u)$. The author in [254] also pointed out that the assumption about the noise-free image and the noise being uncorrelated holds initially, but it does

not necessarily hold for the filtered image, u, and the filtering noise, $(u_0 - u)$. Solo [331] derived a Stein's unbiased risk estimate (SURE) -based criterion for selecting the scale that minimizes the prediction error PE(t) under L_2 loss, assuming independent and identically-distributed (i.i.d.) Gaussian noise of known variance and quadratic penalty. More recently, Papandreou and Maragos [282] studied this problem in a statistical model selection framework and used cross-validation techniques to address it in a principled way. The computational cost seems to be a principal concern in these types of formulations. Awate and Whitaker [16] found empirically that entropy reduction by gradient descent reduces the randomness introduced by the noise faster than it reduces the inherent randomness in the signal. They suggested that an efficient stopping time would be when the relative rate of change of entropy, within two consecutive iterations, falls below some threshold to be chosen.

We proposed [33] a new (very simple) diffusion-stopping criterion inspired by observation of the behavior of the correlation between the noise-free image and the filtered image, corr (f, u), and the correlation between the noisy image and the filtered image, corr (u_0, u). Although the former measure is only available in experimental settings it helps validate the usefulness of the latter. The nonlinear diffusion process starts from the noisy image, $u_0(\mathbf{x})$, and creates a set of filtered images, $u(\mathbf{x}, t)$, by gradually removing noise and details from scale to scale until, as $t \to \infty$, the image converges to a constant value. During this process the correlation between the noise-free image and the filtered image increases as the filtered image moves closer to the noise-free image. This behavior continues until it reaches a peak from where the measure decreases as the filtered image moves slowly towards a constant value. During the same process, the correlation between the noisy image and the filtered image decreases gradually from a value of 1.0 (perfect correlation), to a constant value, as the filtered image becomes smoother (see Fig. 3.14). By comparing both measures,

we observe that as corr (f, u) reaches its maximum (the best possible restored image), the curvature of corr (u_0, u) changes sign. This suggests that a good stopping point of the diffusion process is where the second derivative of corr (u_0, u) reaches a maximum.

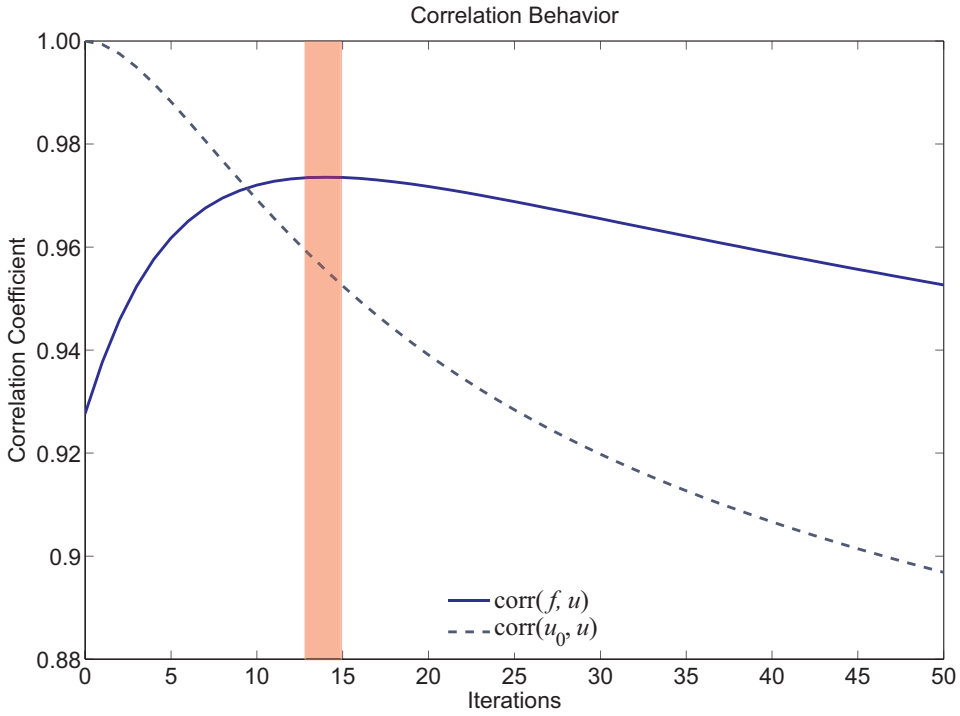

Figure 3.14: The correlation coefficient between the noise-free image and the filtered image increases as the filtered image moves closer to the noise-free image. When the measure reaches a peak it decreases as the filtered image moves slowly towards a constant value. The correlation coefficient between the noisy image and the filtered image decreases gradually from a value of 1.0 (perfect correlation), to a constant value as the filtered image becomes smoother. The shaded region corresponds to good stopping points for the diffusion process.

3.2.5 Numerical Experiments for the Diffusion Stopping Criterion

The performance of the proposed stopping criterion can be observed below along with the restored images of Lena (Figs. 3.15, 3.16 and 3.17), the Boats (Figs. 3.21, 3.22

and 3.23), the Clown (Figs. 3.18, 3.19 and 3.20), the Baboon (Figs. 3.24, 3.25 and 3.26), and the Cameraman (Figs. 3.27, 3.28 and 3.29). We observe that the stopping criterion is almost optimal, allowing the diffusion process to stop near the point where the three filtering methods reach their best possible image restorations. In our experiments, we also observed that the stopping criterion overestimate or underestimate the stopping time in two cases: when the noisy image has 'excess' details, *e.g.*, the Baboon, the stopping criterion tends to stop a little too late, causing some loss of details. (This phenomenon has been also observed in [253].) When the noisy image is a cartoon-like image, *e.g.*, the Cameraman, the stopping criterion tends to stop a little too soon (but only for the proposed model), causing a premature output. This is due to the design of the filter which prevents diffusion across edges. A summary of the results for the stopping criterion vs. optimal stopping time experiments are shown in table 3.2.

Table 3.2: Stopping Criterion Performance by Model

Experiment	Perona-Malik	Catté *et al.*	Bazán-Blomgren
Lena	Criterion: 28 Optimal: 31	Criterion: 15 Optimal: 18	Criterion: 19 Optimal: 24
the Boats	Criterion: 29 Optimal: 28	Criterion: 15 Optimal: 16	Criterion: 19 Optimal: 21
the Clown	Criterion: 29 Optimal: 27	Criterion: 15 Optimal: 16	Criterion: 19 Optimal: 21
the Baboon	Criterion: 38 Optimal: 20	Criterion: 17 Optimal: 9	Criterion: 25 Optimal: 14
the Cameraman	Criterion: 27 Optimal: 29	Criterion: 15 Optimal: 14	Criterion: 17 Optimal: 23

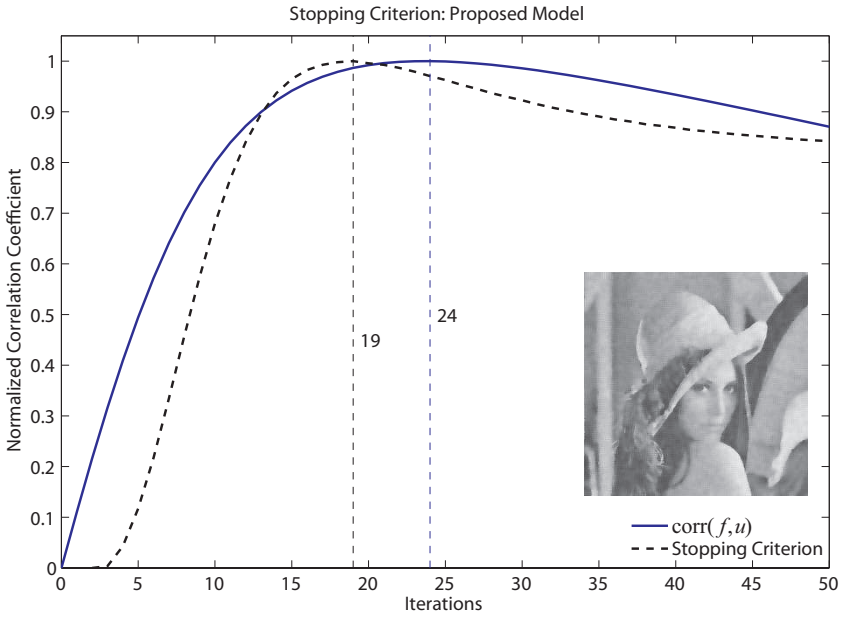

Figure 3.15: Stopping criterion performance along with the restored image of Lena using the proposed model. The measure corr (f, u) suggests stopping the diffusion process after 24 iterations, while the proposed stopping criterion suggests stopping it after 19 iterations.

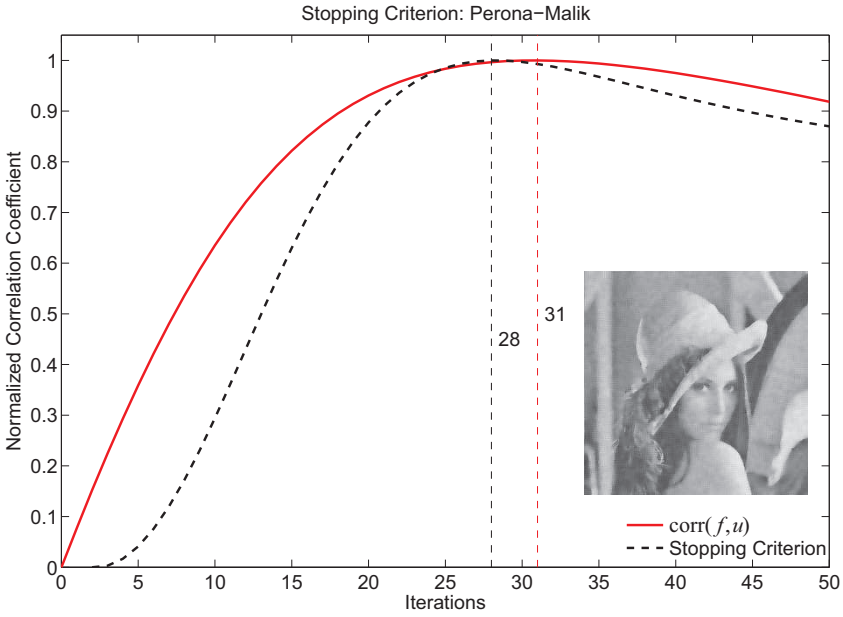

Figure 3.16: Stopping criterion performance along with the restored image of Lena using the Perona-Malik model. The measure corr (f, u) suggests stopping the diffusion process after 31 iterations, while the proposed stopping criterion suggests stopping it after 28 iterations.

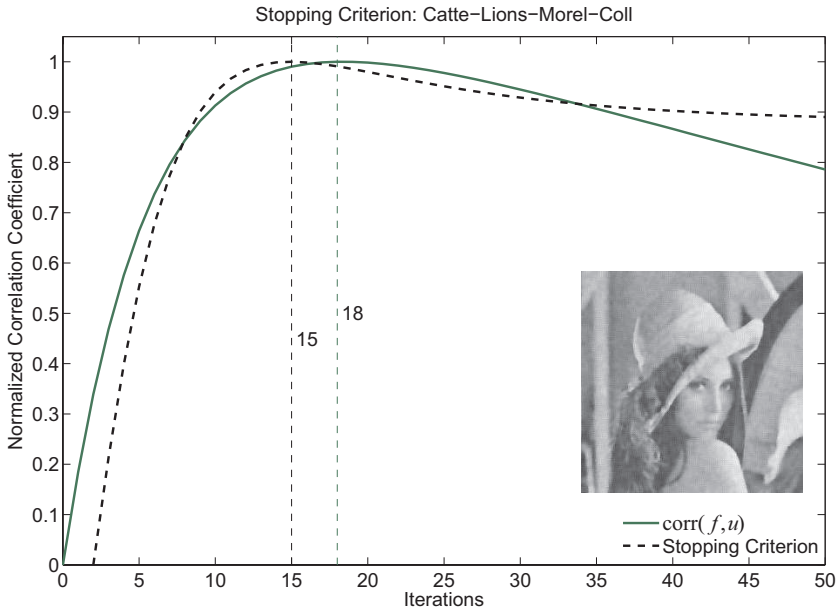

Figure 3.17: Stopping criterion performance along with the restored image of Lena using the Catté-Lions-Morel-Coll model. The measure $\mathrm{corr}\,(f,u)$ suggests stopping the diffusion process after 18 iterations, while the proposed stopping criterion suggests stopping it after 15 iterations.

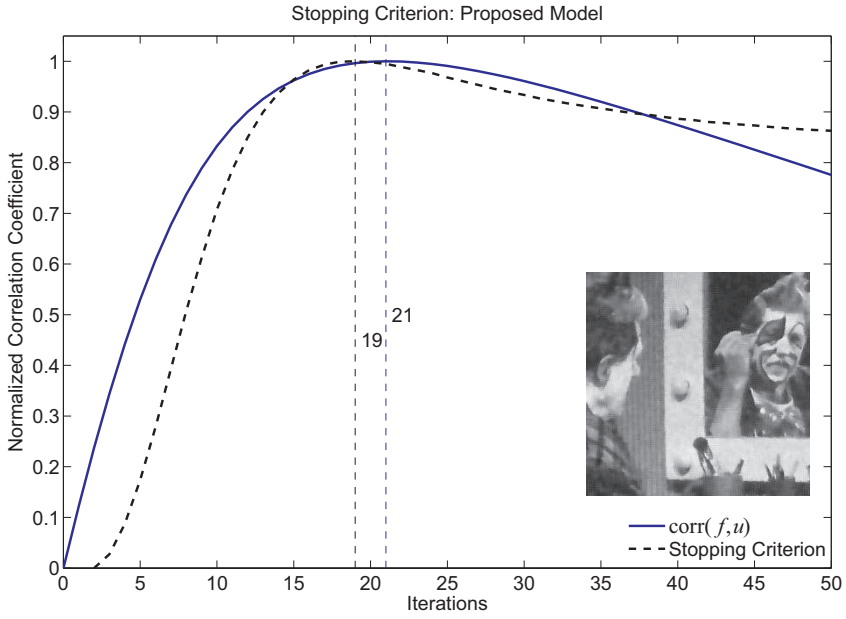

Figure 3.18: Stopping criterion performance along with the restored image of the Clown using the proposed model. The measure $\mathrm{corr}\,(f,u)$ suggests stopping the diffusion process after 21 iterations, while the proposed stopping criterion suggests stopping it after 19 iterations.

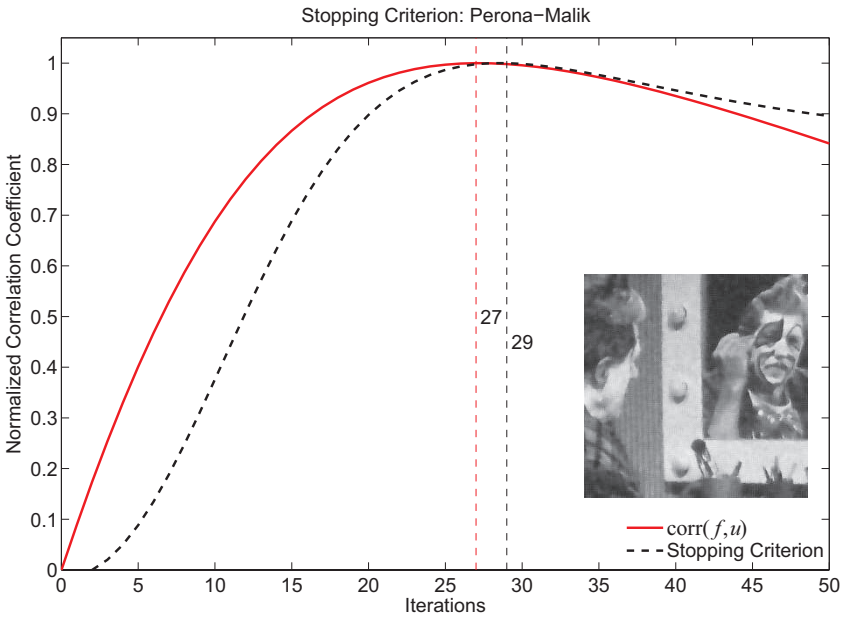

Figure 3.19: Stopping criterion performance along with the restored image of the Clown using the Perona-Malik model. The measure corr (f, u) suggests stopping the diffusion process after 27 iterations, while the proposed stopping criterion suggests stopping it after 29 iterations.

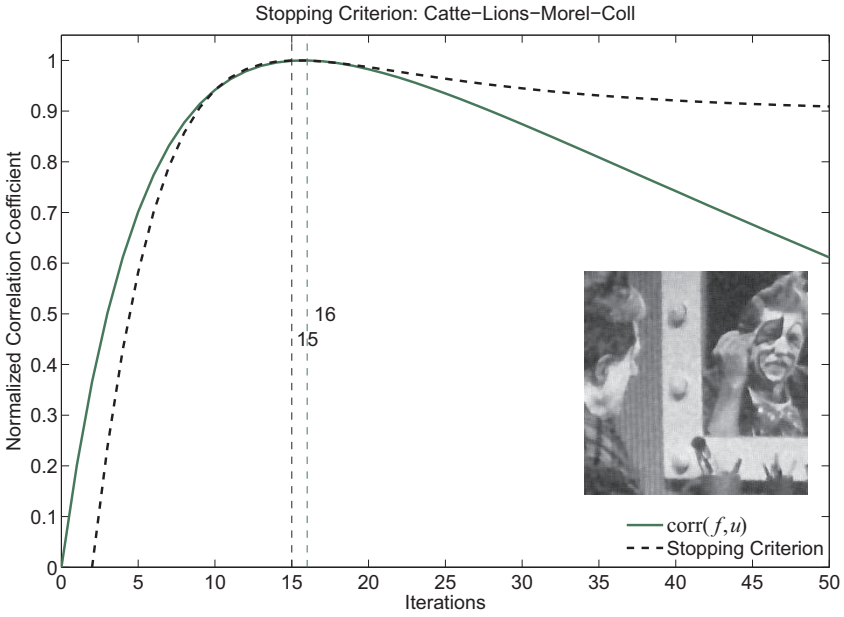

Figure 3.20: Stopping criterion performance along with the restored image of the Clown using the Catté-Lions-Morel-Coll model. The measure corr (f, u) suggests stopping the diffusion process after 16 iterations, while the proposed stopping criterion suggests stopping it after 15 iterations.

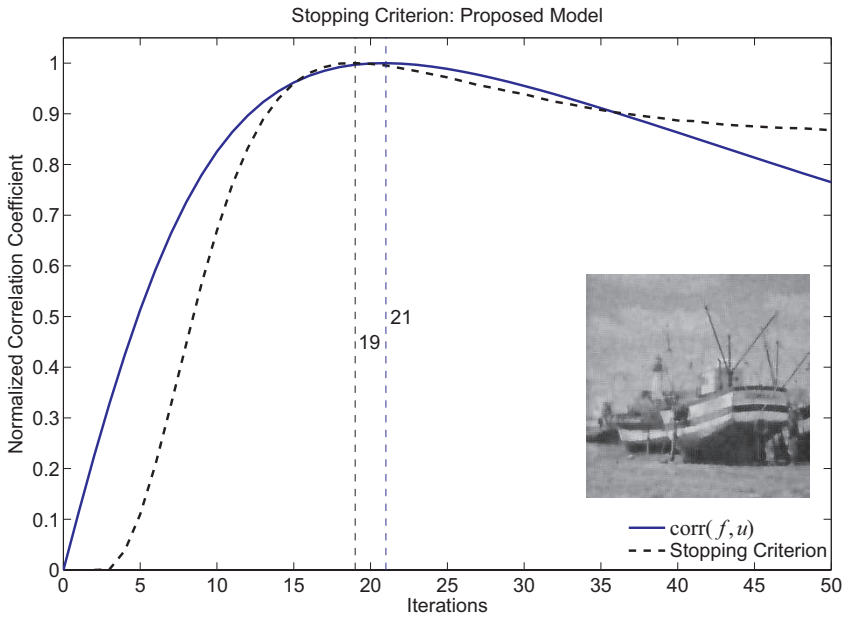

Figure 3.21: Stopping criterion performance along with the restored image of the Boats using the proposed model. The measure corr (f, u) suggests stopping the diffusion process after 21 iterations, while the proposed stopping criterion suggests stopping it after 19 iterations.

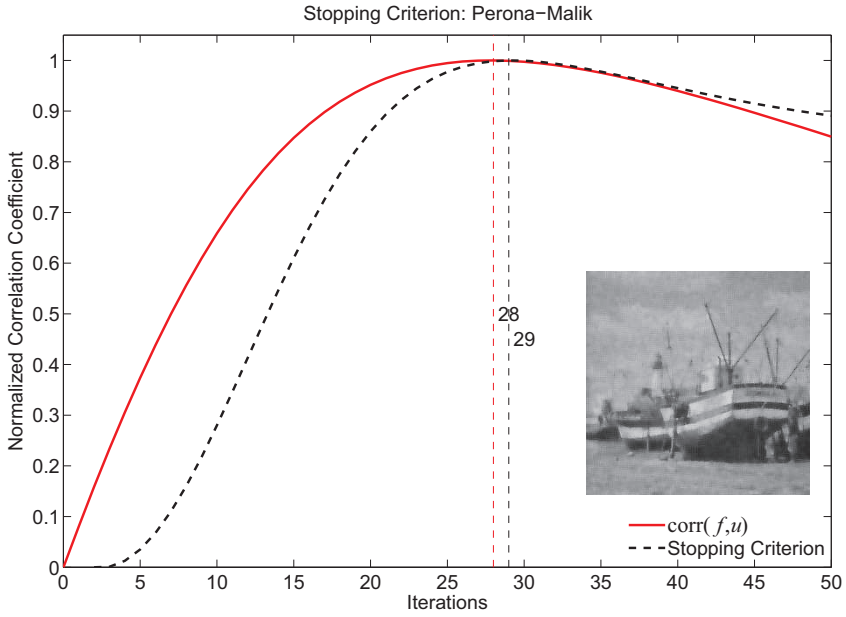

Figure 3.22: Stopping criterion performance along with the restored image of the Boats using the Perona-Malik model. The measure corr (f, u) suggests stopping the diffusion process after 28 iterations, while the proposed stopping criterion suggests stopping it after 29 iterations.

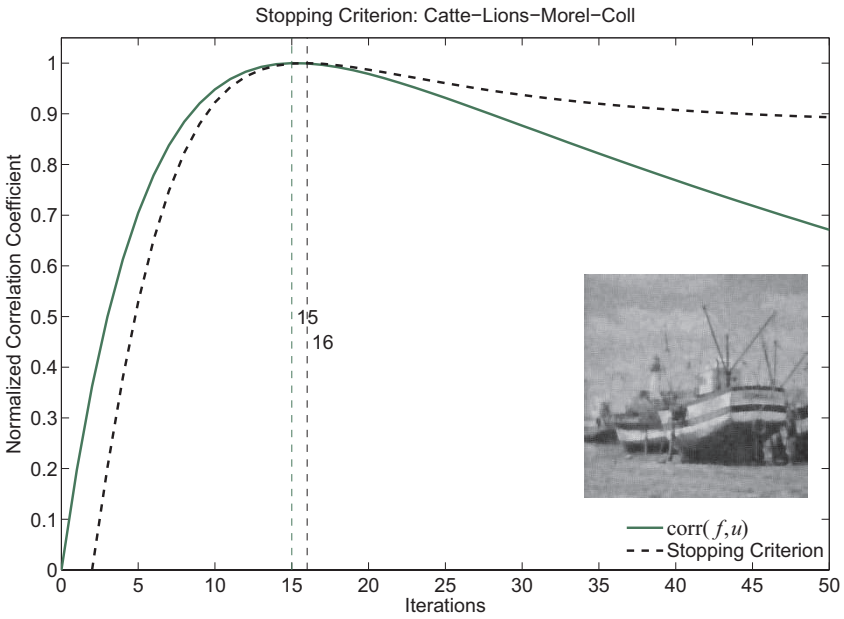

Figure 3.23: Stopping criterion performance along with the restored image of the Boats using the Catté-Lions-Morel-Coll model. The measure $\mathrm{corr}\,(f,u)$ suggests stopping the diffusion process after 16 iterations, while the proposed stopping criterion suggests stopping it after 15 iterations.

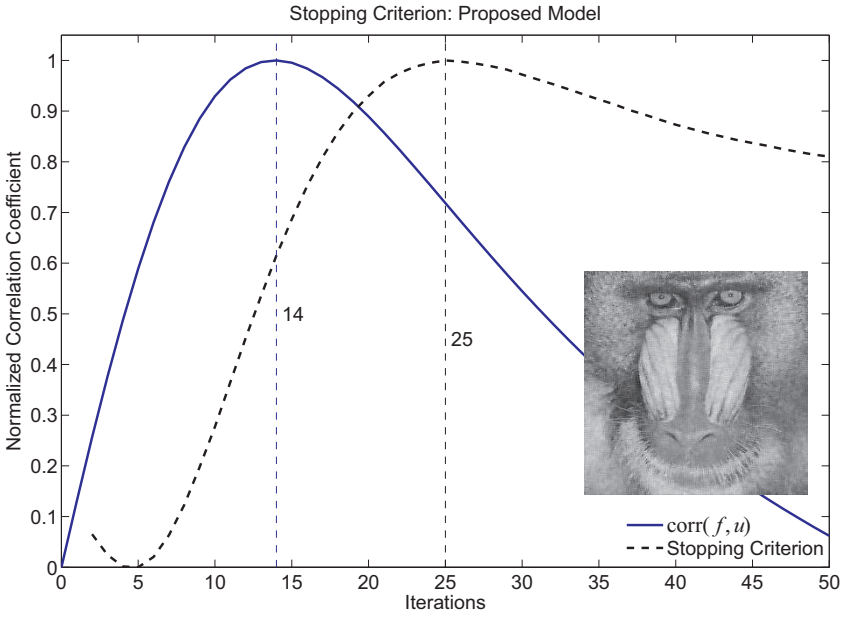

Figure 3.24: Stopping criterion performance along with the restored image of the Baboon using the proposed model. The measure $\mathrm{corr}\,(f,u)$ suggests stopping the diffusion process after 14 iterations, while the proposed stopping criterion suggests stopping it after 25 iterations.

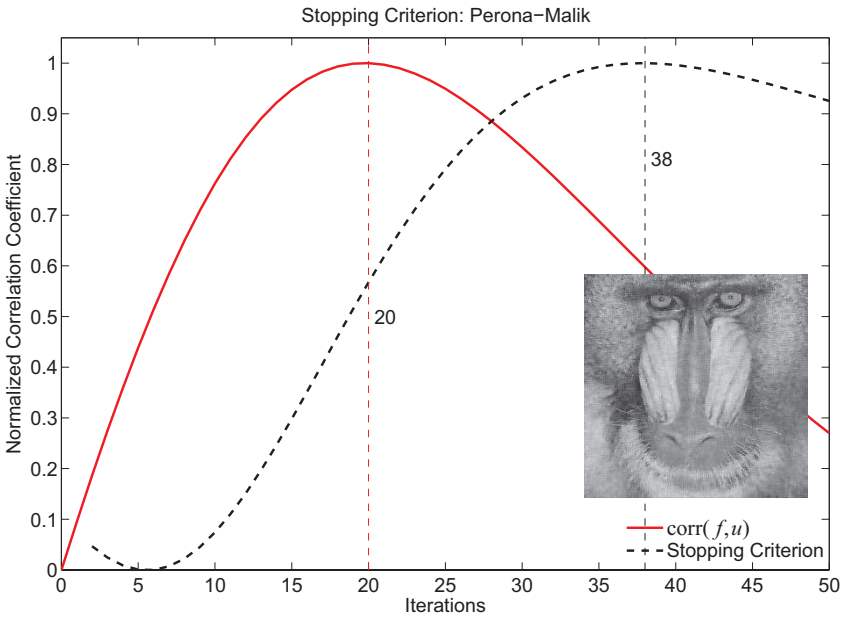

Figure 3.25: Stopping criterion performance along with the restored image of the Baboon using the proposed model. The measure corr (f, u) suggests stopping the diffusion process after 20 iterations, while the proposed stopping criterion suggests stopping it after 38 iterations.

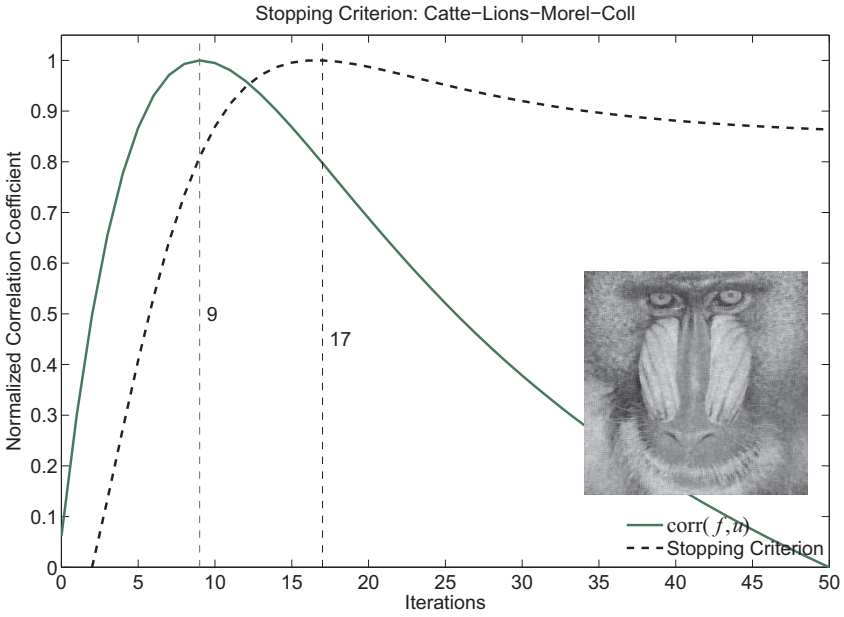

Figure 3.26: Stopping criterion performance along with the restored image of the Baboon using the proposed model. The measure corr (f, u) suggests stopping the diffusion process after 9 iterations, while the proposed stopping criterion suggests stopping it after 17 iterations.

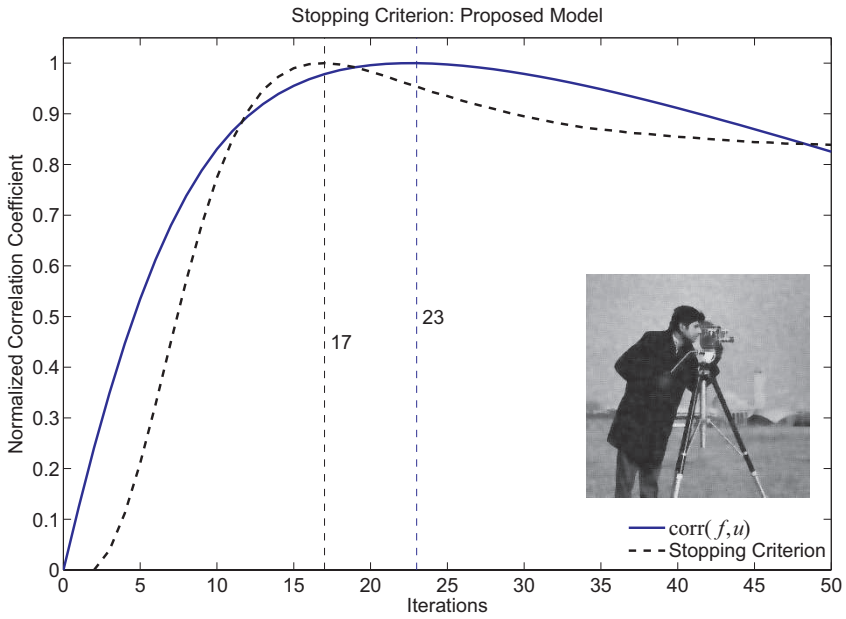

Figure 3.27: Stopping criterion performance along with the restored image of the Cameraman using the proposed model. The measure corr (f, u) suggests stopping the diffusion process after 23 iterations, while the proposed stopping criterion suggests stopping it after 17 iterations.

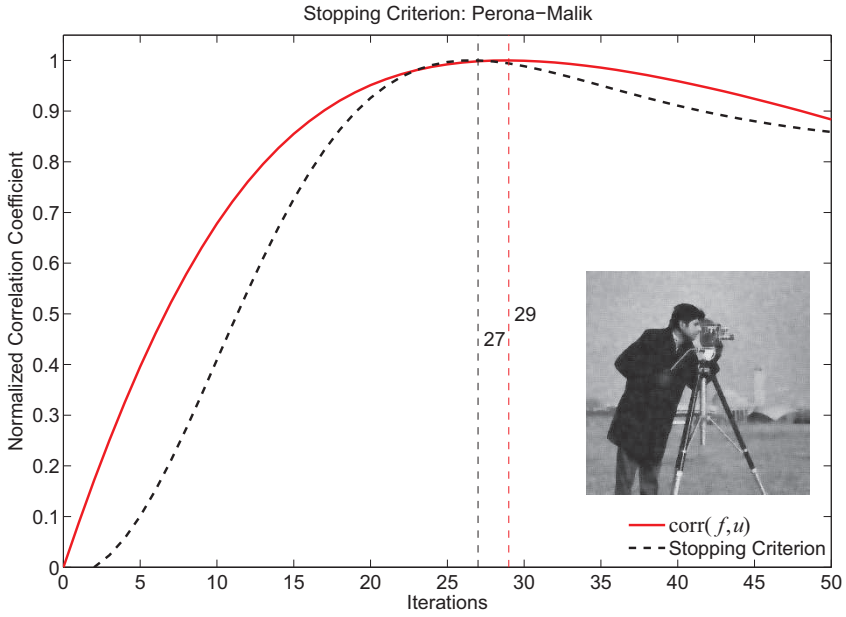

Figure 3.28: Stopping criterion performance along with the restored image of the Cameraman using the proposed model. The measure corr (f, u) suggests stopping the diffusion process after 29 iterations, while the proposed stopping criterion suggests stopping it after 27 iterations.

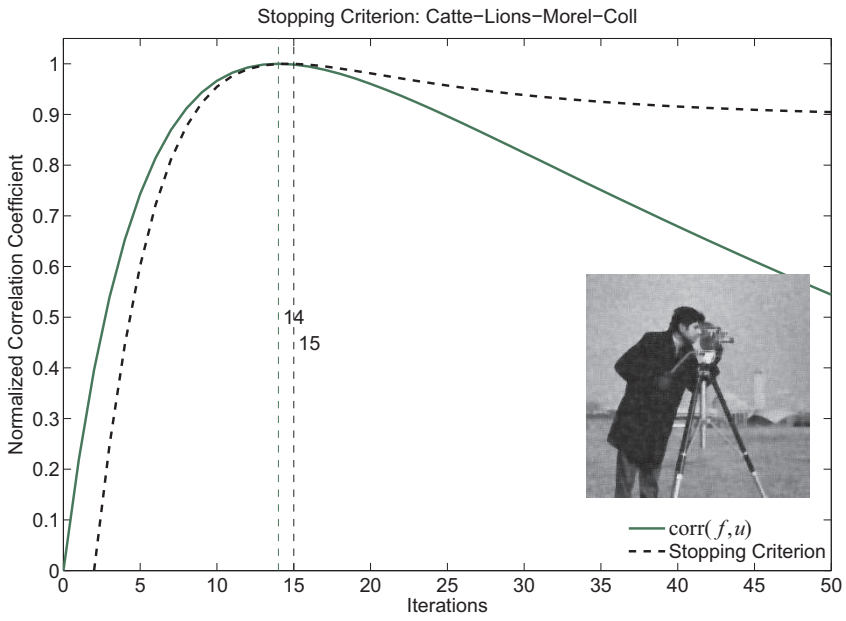

Figure 3.29: Stopping criterion performance along with the restored image of the Cameraman using the proposed model. The measure $\mathrm{corr}\,(f, u)$ suggests stopping the diffusion process after 14 iterations, while the proposed stopping criterion suggests stopping it after 15 iterations.

3.3 Anisotropic Nonlinear Diffusion Models in Electron Tomography

A different way of introducing regularization to the Perona-Malik model is through anisotropic diffusion. We should note that the Perona-Malik model is actually (inhomogeneous) isotropic, since it utilizes a scalar-valued diffusivity, g, which is adapted to the underlying image structure. The main advantage of anisotropic diffusion models over their isotropic counterparts is that they not only account for the modulus of the edge detector, but also its directional information. Isotropic diffusion will inhibit diffusion near edges, making it hard to eliminate noise near them. Anisotropic diffusion, on the other hand, will allow diffusion parallel to the edges while avoiding diffusing perpendicular to them.

Förstner and Gülch [114] and Bigün and Granlund [40], concurrently introduced the matrix field of the structure tensor for image processing, and it is the basis for today's anisotropic diffusion models. The main idea behind these models is to construct the orthogonal system of eigenvectors $\mathbf{v}_1$, $\mathbf{v}_2$, of the diffusion tensor $\mathbf{D}_\sigma$ in such way that they will reveal the presence of edges, *i.e.*, $\mathbf{v}_1 \parallel \nabla u_\sigma$ (parallel) and $\mathbf{v}_2 \perp \nabla u_\sigma$ (perpendicular). Then we choose appropriate (corresponding) eigenvalues that will allow smoothing parallel to the edges and avoid doing so across them. Thus, the diffusion tensor $\mathbf{D}_\sigma$ steers the diffusion process in such a way that the eigenvectors prescribe the diffusion directions and the corresponding eigenvalues determine the amount of diffusion along these directions. Cottet and Germain [74] and Weickert [371, 374] were among the first authors to propose anisotropic nonlinear diffusion models for image processing. Weickert [370] has also provided a mathematical foundation for continuous anisotropic nonlinear diffusion filtering as a scale-space transformation, adequate for simplifying images without renouncing the edge enhancing capability.

Anisotropic nonlinear diffusion (AND) in electron microscopy was introduced by Frangakis and Hegerl [118, 119] . They proposed solving

$$\begin{aligned} u_t - \nabla \cdot (\mathbf{D}_\sigma \cdot \nabla u) &= 0, \qquad \text{on } \Omega \times [0, \infty), \\ u(\mathbf{x}, 0) &= u_0(\mathbf{x}), \qquad \text{on } \Omega, \\ \langle \mathbf{D}_\sigma \cdot \nabla u, \mathbf{n} \rangle &= 0, \qquad \text{on } \partial\Omega \times (0, \infty), \end{aligned} \tag{3.15}$$

where the diffusivity matrix $\mathbf{D}_\sigma$ is structured as follows:

$$\mathbf{D}_\sigma = \begin{bmatrix} \mathbf{v}_1 & \mathbf{v}_2 & \mathbf{v}_3 \end{bmatrix} \begin{bmatrix} \lambda_1 & 0 & 0 \\ 0 & \lambda_2 & 0 \\ 0 & 0 & \lambda_3 \end{bmatrix} \begin{bmatrix} \mathbf{v}_1 & \mathbf{v}_2 & \mathbf{v}_3 \end{bmatrix}^{\mathrm{T}}. \tag{3.16}$$

The vectors $\mathbf{v}_i$ are the eigenvectors of the image's structure tensor $\mathbf{J}_\sigma = \nabla u_\sigma \cdot \nabla u_\sigma^{\mathrm{T}}$ or its convolved version $\mathbf{J}_\rho = G_\rho * \mathbf{J}_\sigma$, where G_ρ is a Gaussian kernel of width ρ. The parameters λ_i are functions of the eigenvalues $\mu_1 \geq \mu_2 \geq \mu_3$, of the structure tensor $\mathbf{J}_\sigma$ (or $\mathbf{J}_\rho$). Together, the eigenvalues μ_i and the eigenvectors $\mathbf{v}_i$, characterize the local structural features of the image u within a neighborhood of size $O(\rho)$. Each eigenvalue μ_i reflects the variance of the gray level in the direction of the corresponding eigenvector $\mathbf{v}_i$, while each parameter λ_i controls the diffusion flux in the direction of $\mathbf{v}_i$, and has to be chosen carefully.

Based on the works of Weickert [375, 376, 377, 382], the authors in [118, 119] chose the parameters λ_i to create a hybrid model that combines both edge enhancing diffusion (EED) and coherence enhancing diffusion (CED). EED is based on the directional information of the eigenvectors of the structure tensor $\mathbf{J}_\sigma$, and its aim is to preserve and enhance edges. CED is based on the directional information of the eigenvectors of the convolved structure tensor $\mathbf{J}_\rho$, and is intended for improving flow-like structures and curvilinear continuities. For EED, the parameters λ_i are chosen following the Perona-Malik model [294] with

$$\begin{aligned} \lambda_1 &= \lambda_2 = g\left(|\nabla u_\sigma|^2\right), \\ \lambda_3 &= 1, \end{aligned} \tag{3.17}$$

while for CED they are defined according to

$$\lambda_1 = \lambda_2 = \alpha,$$
$$\lambda_3 = \begin{cases} \alpha & \text{if } \mu_1 = \mu_3 \\ \alpha + (1-\alpha)\exp\left(-C/(\mu_1-\mu_3)^2\right) & \text{else,} \end{cases} \tag{3.18}$$

with user-defined free parameters α (regularization constant, typically set to 10^{-3}) and $C > 0$. Structures with $(\mu_1 - \mu_3)^2 > C$ will be regarded as line-like patterns and will be enhanced.

To combine the advantages of EDD and CED the approach presented in [118, 119] uses a switch based on comparing an *ad hoc* threshold parameter[10] to the local relation between structure and noise $(\mu_1 - \mu_3)$. EDD is used when the difference $(\mu_1 - \mu_3)$ is smaller than the threshold parameter. When it is larger, the model would switch to CED. In a separate communication, Frangakis, Stoschek and Hegerl [121] applied the hybrid model to 2D and 3D synthetic data and compared it with conventional methods as well as with wavelet transform filtering. They concluded that the model exhibits excellent performance at lower frequencies, achieving considerable improvement in the SNR, but that due to the low-pass characteristics of the diffusion and the discretization stencil, high frequencies components of the signal are irreversibly degraded. They also applied the model to volumetric data as obtained by electron tomography. A considerable SNR improvement was achieved for both of the examples presented. Thus, it greatly facilitated the posterior segmentation and visualization. It was again noted that the method acts as a low-pass filter, and that this is an expected, yet unwanted, effect of the theoretical considerations involved.

Fernández and Li [111, 112] proposed a variant to the model in [118, 119] for ET filtering by anisotropic nonlinear diffusion, capable of reducing noise while preserving both planar and curvilinear structures. They provided their model with a background

[10]The threshold is computed from the mean value of $(\mu_1 - \mu_3)$ in a subvolume of the image containing only noise.

filtering mechanism that highlights the interesting biological structural features and a new criterion for stopping the iterative process. The CED model in Eq. (3.18) diffuses unidirectionally along the direction of minimum change, $\mathbf{v}_3$, and efficiently enhances line-like structures (where $\mu_1 \approx \mu_2 \gg \mu_3$). It was argued in [111] that a significant number of structural features from biological specimens resemble plane-like structures at local scale. Therefore, the authors in [111, 112] defined a set of metrics to discern whether the features are plane-like, line-like, or isotropic. The metrics defined are:

$$P_1 = \frac{\mu_1 - \mu_2}{\mu_1}, \qquad P_2 = \frac{\mu_2 - \mu_3}{\mu_1}, \qquad P_3 = \frac{\mu_3}{\mu_1}, \tag{3.19}$$

which satisfy $0 \leq P_i \leq 1$, $\forall\, i$ and $P_1 + P_2 + P_3 = 1$. In Eq. (3.19), μ_1, μ_2, and μ_3 are the eigenvalues of the convolved structure tensor, $\mathbf{J}_\rho$. These metrics are such that when $P_1 > P_2$ and $P_1 > P_3$, we have a plane-like structure; when $P_2 > P_1$ and $P_2 > P_3$, we have a line-like structure; and when $P_3 > P_1$ and $P_3 > P_2$, we have an isotropic structure. To achieve planar enhancing diffusion, Eq. (3.18) is modified as follows:

$$\begin{aligned}
\lambda_1 &= \alpha, \\
\lambda_2 &= \begin{cases} \alpha & \text{if } \mu_1 = \mu_2 \\ \alpha + (1-\alpha)\exp\left(-C_2/(\mu_1 - \mu_2)^2\right) & \text{else,} \end{cases} \\
\lambda_3 &= \begin{cases} \alpha & \text{if } \mu_1 = \mu_3 \\ \alpha + (1-\alpha)\exp\left(-C_3/(\mu_1 - \mu_3)^2\right) & \text{else.} \end{cases}
\end{aligned} \tag{3.20}$$

For the case of isotropic structure the model employs what Fernández and Li call 'background diffusion', based on Gaussian smoothing.

To address the crucial question of when to stop the filtering process Fernández and Li proposed two different criteria. In [111], they proposed a stopping criterion based on the evolution of the variance in the noise-only subvolume, V, from which the EED/CED threshold's switch was obtained. They devised a ratio similar to the

one proposed in [377], the relative noise variance

$$r_V(t) = \frac{\operatorname{var}(u)_V}{\operatorname{var}(u_0)_V},$$

where $\operatorname{var}(u_0)_V$ and $\operatorname{var}(u)_V$ represent the variance of the gray values of the subvolume V at time 0 and t, respectively. Since $r_V(t)$ decreases monotonically from 1 to 0, a suitable threshold can be set based on the desired noise reduction factor. However, since this criterion does not consider the entire volume, it can not guarantee that the signal will not be affected by the diffusion. To avoid this, they proposed a different criterion [112] similar to the one proposed in [255]. The noise-estimate variance criterion states that the optimal stopping time is the time (iteration) in which $\operatorname{var}(u_0 - u)$ reaches $\operatorname{var}(u_0)_V$, which can be expressed analytically as

$$T = \arg\min_t \left\{ \left| \operatorname{var}(u_0)_V - \operatorname{var}(u_0 - u) \right| \right\},$$

where u_0 and u represent the gray values of the whole volume at time 0 and t, respectively.

The clever AND for the ET approach mentioned above also presents a drawback. Brox and Weickert [54] argued that the linear structure tensor $\mathbf{J}_\rho$, derived from $\mathbf{J}_\sigma$ by smoothing each component using a Gaussian kernel with standard deviation ρ, closes structures of a certain scale very well and removes the noise appropriately. However, it only preserves orientation discontinuities and does not preserve magnitude discontinuities, causing object boundaries to dislocate. Brox, van den Boomgaard, Lauze, van de Weijer, Weickert, Mrázek, and Kornprobst [53] argued that as soon as the orientation in the local neighborhood is not homogeneous, the local neighborhood induced by the Gaussian filter integrates ambiguous structure information. This information might not belong together and could lead to erroneous estimations. In [53] the authors proposed two alternatives to overcome this problem. The first solution

involves the use of robust statistics for choosing one of the ambiguous orientations [360]. The second solution is to adapt the neighborhood to the data by using the Kunahara-Nagao operator [22, 201, 260]. van den Boomgaard [359] showed that the classic Kunahara-Nagao operator can be regarded as a 'macroscopic' version of a PDE image evolution that combines linear diffusion with morphologic sharpening. Other similar approaches involve the choosing of the local neighborhood via adaptive Gaussian windows [245, 246, 261], and the use of nonlinear diffusion that can perform data-adaptive smoothing that prevents the integration of ambiguous data [55, 56, 380].

Brox and Weickert [54] proposed to address the aforementioned problem by replacing the Gaussian convolution by a discontinuity preserving diffusion method. This is obtained by considering the structure tensor $\mathbf{J}_\sigma$, as an initial matrix field that is evolved under the diffusion equation

$$\partial_t u_{ij} - \nabla \cdot \left(\mathbf{D} \left(\left(\nabla_\sigma \sqrt[4]{\sum_{k,l} u_{kl}^2} \right) \cdot \left(\nabla_\sigma \sqrt[4]{\sum_{k,l} u_{kl}^2} \right)^{\mathrm{T}} \right) \cdot \nabla u_{ij} \right) = 0, \qquad (3.21)$$

$\forall\, i, j$, where the evolving matrix field $u_{ij}(\mathbf{x}, t)$ uses $\mathbf{J}_\sigma(\mathbf{x})$ as the initial condition for $t = 0$. The matrix $\mathbf{D}(A) = \mathbf{T}(g(\lambda_i)) \cdot \mathbf{T}^{\mathrm{T}}$ is the diffusion tensor for $A = \mathbf{T}(\lambda_i) \cdot \mathbf{T}^{\mathrm{T}}$. The latter represents a principal axis transformation of A with the eigenvalues λ_i as the elements of a diagonal matrix, $\mathrm{diag}(\lambda_i)$, and the normalized eigenvectors as the columns of the orthogonal matrix, $\mathbf{T}$. For the diffusivity they suggested $g\left(|\nabla u_\sigma|^2\right) = 1 - \exp\left(-3.31488/(|\nabla u_\sigma|/\lambda)^8\right)$, for $c > 0$, and λ is the contrast parameter. In Eq. (3.21), ∇_σ denotes the ∇ operator where Gaussian derivatives with standard deviation σ are employed. This approach tends to prevent boundary dislocations while keeping the desirable properties of the linear structure tensor. In section 3.4 we introduce a new approach based on anisotropic nonlinear diffusion and bilateral filter for electron tomography. It allows noise removal and structure closure at certain scales, while preserving both the orientation and magnitude of discontinuities.

3.4 Anisotropic Nonlinear Diffusion and Bilateral Filter Model in Electron Tomography

In section 3.3 we discussed the application of anisotropic nonlinear diffusion in electron tomography. The approach used in [111, 112, 118, 119] is based on a hybrid EED/CED denoising mechanism that performs very well on data containing low- to mid-frequency signal components. The technique greatly facilitates image enhancement for subsequent segmentation and improved visualization of complex biological specimens. In this section, we propose a new image smoothing and edge detection technique for electron tomography, as an extension to the model we proposed in [33]. This approach employs a combination of anisotropic nonlinear diffusion and bilateral filter. Jiang, Baker, Wu, Bajaj and Chiu [178] introduced bilateral filtering for the removal of noise from biological electron microscopy data. They have shown that bilateral filtering is a very effective mechanism for suppressing the noise in tomograms, while preserving high resolution secondary structure features.

To the best of our knowledge, Bajaj, Wu and Xu [19] and Bajaj and Yu [20] were the first ones to experiment with bilateral filtering coupled to an evolution driven anisotropic geometric diffusion PDE. They called their method 'volumetric anisotropic diffusion model' and it is based on a level set formulation that uses bilateral filtering as a pre-filtering step, in order to obtain more precise curvature information. For the enhancement of 2D features, the model requires the selection of two free parameters that control the diffusion rate, and a threshold switch associated with the image. Our proposed model aims at incorporating the best of both approaches, anisotropic nonlinear diffusion and bilateral filter, in a single computationally robust implementation. The model requires neither the choosing of parameters nor the setting of threshold switches, and it preserves both the orientation and magnitude of discontinuities. The

model is also equipped with the diffusion stopping criterion proposed in [33], based on the second derivative of the correlation between the noisy image and the filtered image.

3.4.1 Local Structure Analysis

The structure tensor of a 3D tomogram u, is a symmetric positive semidefinite matrix given by the product $\mathbf{J}_\sigma = \nabla u_\sigma \cdot \nabla u_\sigma^{\mathrm{T}}$, with $u_\sigma = G_\sigma * u$ where G_σ is a Gaussian kernel of width σ [371, 374]. This structure tensor is the most stable and reliable descriptor of the local structure of an image [372]. Similar to our approach in [33], we propose using a refined estimate of the gradient of u at voxel $\mathbf{x} = (x, y, z)$, obtained by applying a bilateral filter in place of the Gaussian kernel. We have seen above the advantages of BF as a technique for smoothing images while preserving edges. The new structure tensor is therefore

$$\mathbf{J}_{bf} = \nabla u_{bf} \cdot \nabla u_{bf}^{\mathrm{T}} = \begin{bmatrix} (u_{bf})_x^2 & (u_{bf})_x (u_{bf})_y & (u_{bf})_x (u_{bf})_z \\ (u_{bf})_x (u_{bf})_y & (u_{bf})_y^2 & (u_{bf})_y (u_{bf})_z \\ (u_{bf})_x (u_{bf})_z & (u_{bf})_y (u_{bf})_z & (u_{bf})_z^2 \end{bmatrix}. \tag{3.22}$$

The image's local structure features can be determined by performing the eigen-analysis of the structure tensor:

$$\mathbf{J}_{bf} = \mu_1 \mathbf{v}_1 \cdot \mathbf{v}_1^{\mathrm{T}} + \mu_2 \mathbf{v}_2 \cdot \mathbf{v}_2^{\mathrm{T}} + \mu_3 \mathbf{v}_3 \cdot \mathbf{v}_3^{\mathrm{T}}, \qquad \mu_1 \geqslant \mu_2 \geqslant \mu_3, \tag{3.23}$$

where, as before, μ_i are the eigenvalues providing the average contrast along the eigen-directions, and $\mathbf{v}_i$ are the corresponding eigenvectors that give the preferred local orientations.

To further analyse the basic local structures of the 3D tomogram, we can decompose the structure tensor $\mathbf{J}_{bf}$ into three parts: the linear part, $\mathbf{J}_{bf_1}$, the planar part, $\mathbf{J}_{bf_2}$, and the isotropic part, $\mathbf{J}_{bf_3}$, as

$$\mathbf{J}_{bf} = \mathbf{J}_{bf_1} + \mathbf{J}_{bf_2} + \mathbf{J}_{bf_3}, \tag{3.24}$$

where

$$\begin{aligned}
\mathbf{J}_{bf_1} &= (\mu_1 - \mu_2)\, \mathbf{v}_1 \cdot \mathbf{v}_1^{\mathrm{T}}, \\
\mathbf{J}_{bf_2} &= (\mu_2 - \mu_3) \left(\mathbf{v}_1 \cdot \mathbf{v}_1^{\mathrm{T}} + \mathbf{v}_2 \cdot \mathbf{v}_2^{\mathrm{T}} \right), \\
\mathbf{J}_{bf_3} &= \mu_3 \left(\mathbf{v}_1 \cdot \mathbf{v}_1^{\mathrm{T}} + \mathbf{v}_2 \cdot \mathbf{v}_2^{\mathrm{T}} + \mathbf{v}_3 \cdot \mathbf{v}_3^{\mathrm{T}} \right).
\end{aligned} \tag{3.25}$$

This decomposition helps us interpret, visually, the relative contributions of the basic local structures: linear, planar, and isotropic [386]. Fig. 3.30 shows a tensor glyph for each of the following three cases: when $\mathbf{J}_{bf_1}$ is dominant, linear; when $\mathbf{J}_{bf_2}$ is dominant, planar; and when $\mathbf{J}_{bf_3}$ is dominant, isotropic.

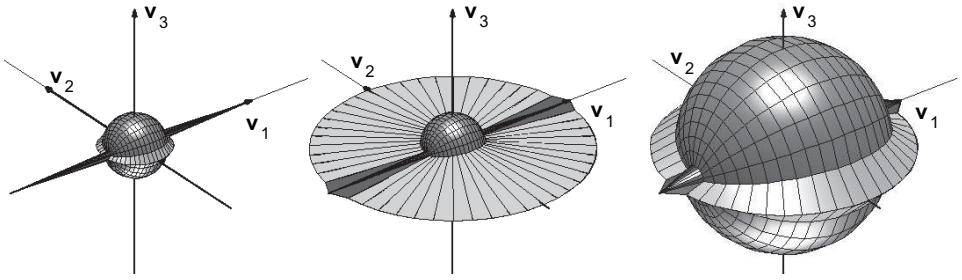

Figure 3.30: The tensor glyphs reveal the basic local structures for the cases: linear, when $\mathbf{J}_{bf_1}$ is dominant; planar, when $\mathbf{J}_{bf_2}$ is dominant; and isotropic, when $\mathbf{J}_{bf_3}$ is dominant. The vectors $\mathbf{v}_1$, $\mathbf{v}_2$, and $\mathbf{v}_3$ are the corresponding eigenvectors to the eigenvalues μ_1, μ_2, and μ_3, respectively. The figure was rendered using the tensor visualization tool T-FLASH [386].

We can also use the equivalent interpretation given in [111] where, based on the relative magnitudes of the eigenvalues, they characterize the three basic local structures as: (i) Linear structures, $\mu_1 \approx \mu_2 \gg \mu_3$, have a preferred direction along eigenvector $\mathbf{v}_3$, while eigenvectors $\mathbf{v}_1$ and $\mathbf{v}_2$ are perpendicular to the linear structure; (ii) Planar structures, $\mu_1 \gg \mu_2 \approx \mu_3$, have two preferred directions along eigenvectors $\mathbf{v}_2$ and $\mathbf{v}_3$, while eigenvector $\mathbf{v}_1$ is perpendicular to the planar structure; (iii) Isotropic structures, $\mu_1 \approx \mu_2 \approx \mu_3$, have no preferred direction. We will take advantage of the above interpretation of the information provided by the structure tensor at each voxel $\mathbf{x}$ to devise a robust AND image restoration model for 3D electron tomograms

of mitochondria. Images of mitochondria contain many flow-like patterns and they are usually of very poor quality. For it is necessary to enhance them by closing interrupted structures. To exploit the coherence and curvilinear continuity, while connecting possible interrupted lines and planes, we average the structure tensor $\mathbf{J}_{bf}$, over a region by applying bilateral filtering in the form $\overline{\mathbf{J}}_{bf} = G_{bf} * \mathbf{J}_{bf}$. The directional information is thereby averaged, although the structure of the region is still maintained by the discontinuity preserving bilateral filtering.

3.4.2 Diffusion Tensor Construction

The diffusion tensor $\mathbf{D}_{bf} \in \mathbb{R}^{3\times3}$, controls the smoothing across the 3D tomogram. We define the diffusion tensor as a function of the structure tensor $\overline{\mathbf{J}}_{bf}$,

$$\mathbf{D}_{bf} = \begin{bmatrix} \mathbf{v}_1 & \mathbf{v}_2 & \mathbf{v}_3 \end{bmatrix} \begin{bmatrix} \lambda_1 & 0 & 0 \\ 0 & \lambda_2 & 0 \\ 0 & 0 & \lambda_3 \end{bmatrix} \begin{bmatrix} \mathbf{v}_1 & \mathbf{v}_2 & \mathbf{v}_3 \end{bmatrix}^{\mathrm{T}}, \tag{3.26}$$

where $\mathbf{v}_i$ are the structure tensor's eigenvectors. The eigenvalues of the diffusion tensor, λ_i, define the strength of the smoothing along the eigen-directions $\mathbf{v}_i$, and allow the application of different diffusion processes: (i) Linear diffusion or Gaussian smoothing is applied when $\lambda_i = 1, \forall\, i$, (ii) Nonlinear diffusion is applied if $\lambda_i = g\left(|\nabla u|^2\right), \forall\, i$, (iii) Anisotropic nonlinear diffusion can be applied by setting the values λ_i so they reflect the image's underlying local structure. We have already mentioned the strengths and weaknesses of the three diffusion processes.

As mentioned in section 3.3, it is now common to use a hybrid approach that switches the diffusion process from EED to CED and *vice versa*, based on selected *ad hoc* thresholds [118, 119]. Switching to a third diffusion mode, Gaussian diffusion (GD), in areas where the image becomes predominantly isotropic (based on another *ad hoc* threshold) has also been suggested [111, 112]. We propose to use the anisotropic diffusion process where the model switches among the three modes, EED/CED/GD,

automatically based on information extracted locally from the signal. The model can be regarded as 'structure enhancing diffusion' (SED), where the eigenvalues are defined as[11]

$$\begin{aligned}
\lambda_1 &= g\left(|\nabla u_{bf}|^2\right), \\
\lambda_2 &= \begin{cases} g\left(|\nabla u_{bf}|^2\right) & \text{if } \mu_1 = \mu_2 \\ g\left(|\nabla u_{bf}|^2\right) + \left(1 - g\left(|\nabla u_{bf}|^2\right)\right) \exp\left(-C_2/(\mu_1 - \mu_2)^2\right) & \text{else,} \end{cases} \\
\lambda_3 &= \begin{cases} g\left(|\nabla u_{bf}|^2\right) & \text{if } \mu_1 = \mu_3 \\ g\left(|\nabla u_{bf}|^2\right) + \left(1 - g\left(|\nabla u_{bf}|^2\right)\right) \exp\left(-C_3/(\mu_1 - \mu_3)^2\right) & \text{else.} \end{cases}
\end{aligned} \tag{3.27}$$

The coherence measures $(\mu_1 - \mu_2)^2$ and $(\mu_1 - \mu_3)^2$ are computed based on the eigenvalues of the averaged structure tensor $\overline{\mathbf{J}}_{bf}$, and the parameters C_2 and C_3 act as thresholds such that structures where $(\mu_1 - \mu_2)^2 > C_2$ and $(\mu_1 - \mu_3)^2 > C_3$ are regarded as planar patterns, while structures where $(\mu_1 - \mu_2)^2 < C_2$ and $(\mu_1 - \mu_3)^2 > C_3$ are regarded as linear patterns. These preferred orientations are summarized in table 3.3.

Table 3.3: Structure Patterns Based on Coherence Measures

$(\mu_1 - \mu_2)^2$	$(\mu_1 - \mu_3)^2$	**Local Structure**
$> C_2$	$> C_3$	Planar
$< C_2$	$< C_3$	Linear

In Eq. (3.27), $g\left(|\nabla u_{bf}|^2\right)$ is a monotonically decreasing function such as Perona-Malik's [294]

$$g\left(|\nabla u_{bf})\,|^2\right) = \frac{1}{1 + |\nabla u_{bf}|^2/\lambda^2}, \tag{3.28}$$

with $\lambda > 0$ the typical contrast threshold parameter. There are several ways to set this parameter. Perona and Malik [294] suggested using the idea presented by Canny [60] and set λ as a percentile, p, of the image gradient magnitudes at each iteration.

[11] In practice, the logical 'if $\mu_1 = \mu_2$ then' and 'if $\mu_1 = \mu_3$ then' are unnecessary if we use $\exp\left(-C_2\Big/\left((\mu_1 - \mu_2)^2 + \varepsilon\right)\right)$ and $\exp\left(-C_3\Big/\left((\mu_1 - \mu_3)^2 + \varepsilon\right)\right)$, for small ε.

(The recommended value is commonly $p = 90\%$.) A by-product of this approach is a decreasing λ, which has an stabilizing effect on the diffusion process [253]. Black, Sapiro, Marimont and Heeger [42] and Black and Sapiro [41] recommended using robust statistics to globally or locally estimate λ. They proposed computing

$$\lambda = 1.4826 \text{ median}\left(\left||\nabla u_{bf}| - \text{median}\left(|\nabla u_{bf}|\right)\right|\right), \tag{3.29}$$

where the constant 1.4826 arrives from the fact that a normal distribution with unit variance has a median absolute deviation (MAD) of roughly $0.6745 = 1/1.4826$. A local estimate of the parameter, λ_l, can be set by considering $\lambda_l = \max(\lambda, \lambda_e)$, where λ_e is computed locally by applying Eq. (3.29) on a small predefined region. We will apply the former recommendation in our experiments.

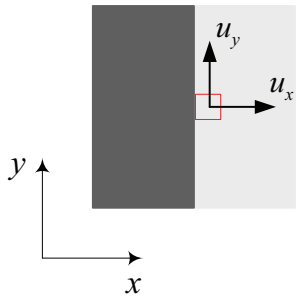

Figure 3.31: Fragment of an image where an edge pixel's gradients has components $u_y = 0$ and $0 < |u_x| \leqslant 1$, depending on the gray values in the two regions.

The advantages of the proposed definitions for the diffusion tensor's eigenvalues become evident when we perform a 2D analysis of the behavior of λ_1 and λ_2. Assume we are standing on an edge pixel as shown in Fig. 3.31. In this case $u_y = 0$ and $0 < |u_x| \leqslant 1$, depending on the gray values in the two regions. The typical hybrid approach will use a chosen threshold to switch between EED and CED (see Eq. (3.17) and Eq. (3.20)), and set the diffusion tensor's eigenvalues to either $\lambda_1 = g\left(|\nabla u|^2\right)$ or $\lambda_1 = \alpha$; and either $\lambda_2 = 1$ or $\lambda_2 = \alpha + (1-\alpha)\exp\left(-C/(\mu_1 - \mu_2)^2\right)$. Assuming,

e.g., the values[12] $\alpha = 10^{-3}$ and $C = 4.5 \times 10^{-4}$, and considering that $(\mu_1 - \mu_2)^2 = \left(u_x^2 - u_y^2\right)^2 + 4\left(u_x u_y\right)^2$, we can plot λ_1 and λ_2 along $u_y = 0$ and interpret the following (see Fig. 3.32):

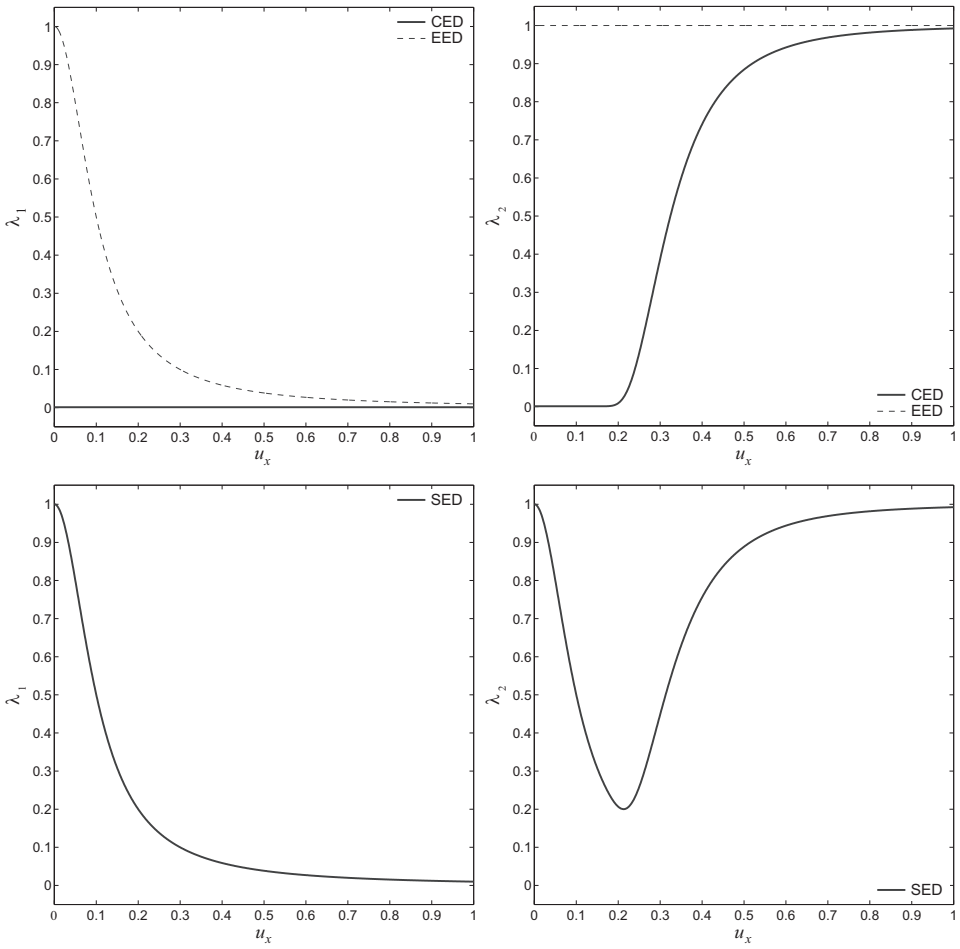

Figure 3.32: Eigenvalues λ_1 and λ_2 for the EED, CED, and SED models. The hybrid EED/CED model switches sharply between the EED and CED curves based on an *ad hoc* threshold.

(i) For low gradient $|u_x| \to 0$, we want the model to assume GD mode (recall that $|u_y| = 0$). In this case, the hybrid EED/CED model will assume EED mode where $\lambda_1 \approx 1$ and $\lambda_2 = 1$. Similarly, the SED model will assume $\lambda_1 \approx 1$ and $\lambda_2 \approx 1$.

[12]Parameter C is typically set to 1/100 of the root-mean-square contrast of the image [119]. The value $C = 4.5 \times 10^{-4}$ comes when considering one of the mitochondrion tomograms used in our experiments.

(ii) For mid-range gradients $0 < |u_x| < 1$, the values for λ_1 must decrease to prevent diffusing across the edge. In the hybrid EED/CED model, λ_1 will decrease monotonically until it suddenly switches from EED to CED where $\lambda_1 = \alpha$. In the SED model, λ_1 will decrease monotonically to zero. Also, for mid-range gradients, $0 < |u_x| < 1$, the values for λ_2 must decrease to prevent creating artificial edges. In the hybrid EED/CED model, $\lambda_2 = 1$ until the model switches sharply from EED mode to CED mode where $\lambda_2 < 1$. In the SED model, λ_2 decreases gradually.

(iii) For high gradients $|u_x| \to 1$, we want the model the assume low values for λ_1 (no diffusion across the edge), and large values for λ_2 (full diffusion along the edge). In this case, the hybrid EED/CED will be in CED mode and will assume the correct values for λ_1 and λ_2. The SED model will continuously assume the correct values for λ_1 and λ_2.

(iv) The above rationale for the 2D case extends naturally to 3D. Also, if a voxel belongs to a linear structure, $\mu_1 \approx \mu_2 \gg \mu_3$, then $(\mu_1 - \mu_2) \to 0$ and consequently the term $\exp\left(-C_2/(\mu_1 - \mu_2)^2\right) \to 0$, making the hard switch between planar and linear structures unnecessary.

3.4.3 Contour Extraction Using the Level Set Method

Osher and Sethian [278] developed a framework relying on a PDE approach for modeling propagating interfaces. These methods have been applied to recover shapes of 2D and 3D objects from visual data, as shown by Malladi, Sethian and Vemuri [222]. This modeling scheme makes no *a priori* assumptions about the object's shape and starts with an arbitrary function, propagating it in the direction normal to the curve along its gradient field with a certain speed, to recover shapes in the image.

The level set formulation allows both forward and backward motion of the initial front through the creation of a higher dimensional function $\phi(\mathbf{x}, t)$ where the initial

position of the front is embedded as the zero level set. The evolution of the function $\phi(\mathbf{x}, t)$ is then linked to the propagation of the front itself through a time-dependent initial value problem. Thus, at any time t, the position of the front is given by the zero level set of the time-dependent level set function $\phi(\Gamma(t) = \{\mathbf{x} \,|\, \phi(\mathbf{x}, t) = 0\})$. The evolution equation, or level set equation [323], for ϕ given in [278] can be written as follows:

$$\phi_t + F|\nabla\phi| = 0, \qquad \text{given } \phi(\mathbf{x}, 0). \tag{3.30}$$

Many implementations [5, 222, 277, 323, 324] of the level set method utilize a zero (or initial) level set such that $\phi(\mathbf{x}, 0) = \pm d(\mathbf{x})$, where $\pm d(\mathbf{x})$ is the signed distance to $\Gamma(0)$. This choice of ϕ allows for both conceptual simplifications and computational savings [277, section 4.2]. Throughout the evolution of the front, in order to avoid the formation of shocks, very flat shapes, and/or very sharp shapes, a re-initialization process is often used periodically to restore a signed distance function. One approach widely used for re-initialization is to solve the equation

$$\phi_t = \text{sign}(\phi_0)(1 - |\nabla\phi|), \tag{3.31}$$

given the function to be re-intialized ϕ_0 and the sign function $\text{sign}(\phi)$ [277]. The process of re-initialization, using the PDE-based method above or similar variation, can be complicated and expensive. There is no simple way to determine how and when the level set function should be re-initialized to a signed distance function.

Li, Xu, Gui and Fox [210] presented a variational formulation whose propagating front is an approximate signed distance function yet does not require re-initialization. The variational energy functional consists of both an internal energy term that forces the level set function to be kept as an approximate signed distance function, and an external energy term that drives the zero level set toward the sought object contours

in the image. The total energy functional is given by

$$\mathcal{E}(\phi) = \mu\mathcal{P}(\phi) + \mathcal{E}_{g,\lambda,\nu}(\phi). \tag{3.32}$$

The first term in the sum is the internal energy. It helps prohibit the deviation of ϕ from a signed distance function, where $\mu > 0$ is the parameter controlling the effect of the penalizing the deviation. $\mathcal{P}(\phi)$ is a metric that characterizes how close ϕ is to a signed distance function whose definition follows from Eq. (3.31):

$$\mathcal{P}(\phi) = \frac{1}{2}\int_{\Omega} (|\nabla\phi| - 1)^2 \, d\mathbf{x}. \tag{3.33}$$

The second term in the sum of Eq. (3.32) is the external energy term that moves the zero level curve toward the object boundaries. Given an image u we can define the following edge indicator function where G_σ is the Gaussian kernel with standard deviation σ:

$$g = \frac{1}{1 + |\nabla G_\sigma * u|^2}. \tag{3.34}$$

With this we can further specify our external energy term:

$$\mathcal{E}_{g,\lambda,\nu}(\phi) = \lambda\mathcal{L}_g(\phi) + \nu\mathcal{A}_g(\phi), \tag{3.35}$$

for terms $\mathcal{L}_g(\phi) = \int_\Omega g\delta(\phi)|\nabla\phi| d\mathbf{x}$ and $\mathcal{A}_g(\phi) = \int_\Omega gH(-\phi)\, d\mathbf{x}$, where $\delta(\cdot)$ is the univariate Dirac function and $H(\cdot)$ is the Heaviside function, and constants $\lambda > 0$ and ν. The energy term $\mathcal{L}_g(\phi)$ computes the length of the zero level curve of ϕ while $\mathcal{A}_g(\phi)$ is the weighted area on the interior of the zero level set and speeds up the curve evolution. The coefficient ν serves to control both the speed and direction of the curve propagation and should be chosen appropriately depending on the relative location of the initial contour to the object of interest. For an initial contour outside the object, ν should be a negative value so that the contours may shrink to the object boundary; whereas, a positive value should be chosen for ν if the initial contour is inside the object so that the contours might expand to the boundary.

The use of this energy functional completely eliminates the need for the expensive re-initialization as the evolution of the level set function is the gradient flow that minimizes the overall energy functional. The internal energy term maintains the level set function as an approximate signed distance function while the external energy term drives the propagation. The evolution equation is determined using calculus of variations to differentiate $\mathcal{E}$ and setting its Gâteaux derivative equal to zero, yielding the steepest descent process for minimization of the functional $\mathcal{E}$:

$$\frac{\partial \phi}{\partial t} = \mu \left(\nabla^2 \phi - \nabla \cdot \left(\frac{\nabla \phi}{|\nabla \phi|} \right) \right) + \lambda \delta (\phi) \nabla \cdot \left(g \frac{\nabla \phi}{|\nabla \phi|} \right) + \nu g \delta (\phi) . \tag{3.36}$$

We will use this approach to extract the main contours of the mitochondrion structure, which will facilitate the 3D rendering of the structure.

3.4.4 Numerical Experiments for the Anisotropic Nonlinear Diffusion and Bilateral Filter Model in Electron Tomography

After the 3D tomogram of the HeLa cell mitochondrion has been reconstructed, we apply the algorithm described in section 3.4 for the removal of noise and the enhancement of the structural features[13]. This step is critical for the posterior segmentation and extraction of the structure-defining contours. The problem to solve is

$$\begin{aligned} & u_t - \nabla \cdot (\mathbf{D}_{bf} \cdot \nabla u) = 0 \qquad \text{on } \Omega \times [0, \infty) , \\ & u(\mathbf{x}, 0) = u_0 (\mathbf{x}) \qquad \text{on } \Omega, \\ & \langle \mathbf{D}_{bf} \cdot \nabla u, \mathbf{n} \rangle = 0 \qquad \text{on } \partial\Omega \times (0, \infty) . \end{aligned} \tag{3.37}$$

Adopting the following notation for the components of the diffusion tensor:

$$\mathbf{D}_{bf} = \lambda_1 \mathbf{v}_1 \cdot \mathbf{v}_1^{\mathrm{T}} + \lambda_2 \mathbf{v}_2 \cdot \mathbf{v}_2^{\mathrm{T}} + \lambda_3 \mathbf{v}_3 \cdot \mathbf{v}_3^{\mathrm{T}} = \begin{bmatrix} d_{11} & d_{12} & d_{13} \\ d_{21} & d_{22} & d_{23} \\ d_{31} & d_{32} & d_{33} \end{bmatrix} , \tag{3.38}$$

[13] We refer the reader to chapter 5 for a description of the algorithm to implement this model.

we can expand Eq. (3.37) and write

$$\begin{aligned} u_t - \partial_x \left(d_{11} u_x + d_{12} u_y + d_{13} u_z \right) \\ - \partial_y \left(d_{21} u_x + d_{22} u_y + d_{23} u_z \right) \\ - \partial_z \left(d_{31} u_x + d_{32} u_y + d_{33} u_z \right) = 0, \end{aligned} \tag{3.39}$$

for $t > 0$, with the observed image as initial condition, and homogeneous Neumann boundary conditions. We can apply the standard explicit finite difference scheme using central difference to approximate the spatial derivatives, and forward difference to approximate the time derivative. The condition for stability is given by $\delta t \leq 1/6$ [381]. The update will be

$$\begin{aligned} u_{t+1} = u_t + \delta t \, [\, \partial_x \left(d_{11} u_x + d_{12} u_y + d_{13} u_z \right) \\ + \partial_y \left(d_{21} u_x + d_{22} u_y + d_{23} u_z \right) \\ + \partial_z \left(d_{31} u_x + d_{32} u_y + d_{33} u_z \right)] \, . \end{aligned} \tag{3.40}$$

Before applying the proposed SED model to a 3D electron tomogram of a mitochondrion, we apply the model to a more familiar set of 2D images below. These experiments demonstrate the excellent performance of the proposed model, where the structures of the images have been enhanced while most the noise has been removed. Figs. 3.4, 3.6 and 3.10 show the noise-free images of Lena, the Clown, and the Baboon and their corresponding noisy images. We ran the three models EED, CED, and SED to the points of maximum similarity between the noise-free images and each of their filtered images. The similarity was measured by the correlation coefficient between the noise-free image and each of the filtered images, $\mathrm{corr}\,(f, u)$. In Figs. 3.33, 3.34 and 3.35 we can observe that the SED model not only enhances the structures of the images, but also removes sufficient noise for the filtered images to move very close to the noise-free images.

Fig. 3.36 shows some results of the SED model applied to the 3D electron tomogram of the HeLa cell mitochondrion. The proposed approach achieves excellent noise

Figure 3.33: (*left to right*) Filtered images of Lena by EED and CED, respectively. The maximum correlation coefficients between the noise-free image and the filtered images are 0.9621 and 0.9197, respectively. Filtered image of Lena by SED. The maximum correlation coefficient between the noise-free image and the filtered image is 0.9703.

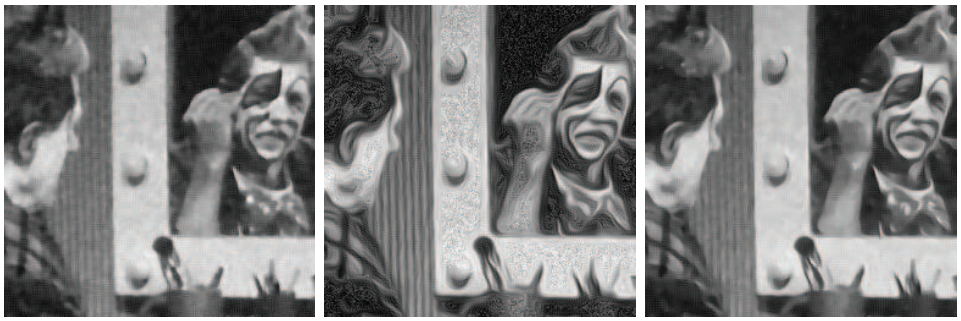

Figure 3.34: (*left to right*) Filtered images of the Clown by EED and CED, respectively. The maximum correlation coefficients between the noise-free image and the filtered images are 0.9782 and 0.9613, respectively. Filtered image of the Clown by SED. The maximum correlation coefficient between the noise-free image and the filtered image is 0.9817.

reduction while preserving the salient edge features. In order to facilitate extraction of the structures, we synthetically enhance the contrast by applying the confidence connected segmentation algorithm [244]. In this context, this simple region-growing segmentation method produces sufficiently good results for the extraction stage, but more flexible methods such as the watershed technique [367] or the Chan-Vese [66] algorithm can easily be substituted. After segmentation, the features are extracted using the level set approach described in subsection 3.4.3. One significant advantage of this formulation is the liberty allowed in selecting the initial level set function.

Figure 3.35: (*left to right*) Filtered images of the Baboon by EED and CED, respectively. The maximum correlation coefficients between the noise-free image and the filtered images are 0.8987 and 0.8757, respectively. Filtered image of the Baboon by SED. The maximum correlation coefficient between the noise-free image and the filtered image is 0.9065.

Traditionally, using level set methods requires the initial level set to be a signed distance function ϕ_0 so that re-initialization can be applied. However, with this need eliminated, a much simpler initial function may be defined:

$$\phi_0(\mathbf{x}) = \begin{cases} -\eta & \mathbf{x} \in \Omega_0 - \partial\Omega_0 \\ 0 & \mathbf{x} \in \partial\Omega_0 \\ \eta & \Omega - \Omega_0, \end{cases} \tag{3.41}$$

given arbitrary Ω_0, a subset in the image domain Ω where $\partial\Omega_0$ is the set of points on the boundary of Ω_0, and $\eta > 0$. For our implementation $\eta = 4$ is selected; however, most any constant would work. For the purposes here, in Eq. (3.36), we use a Dirac function that is slightly smoothed. We define the regularized Dirac function $\delta_\epsilon(\mathbf{x})$ as follows

$$\delta_\epsilon(\mathbf{x}) = \begin{cases} 0 & |\mathbf{x}| > \epsilon \\ \frac{1}{2\epsilon}\left(1 + \cos(\frac{\pi \mathbf{x}}{\epsilon})\right) & |\mathbf{x}| \leq \epsilon, \end{cases} \tag{3.42}$$

and utilize $\epsilon = 1.5$ for our implementation.

In implementing the proposed level set method we carefully selected both our time-step τ and coefficient μ to be safely within the range required for stability ($\tau\mu < \frac{1}{4}$ as explained in [210]), $\tau = 5$ and $\mu = 0.04$. The level set functions were initialized as the function ϕ_0 defined by Eq. (3.31) with $\eta = 4$ using selected regions Ω_0. Fig. 3.38

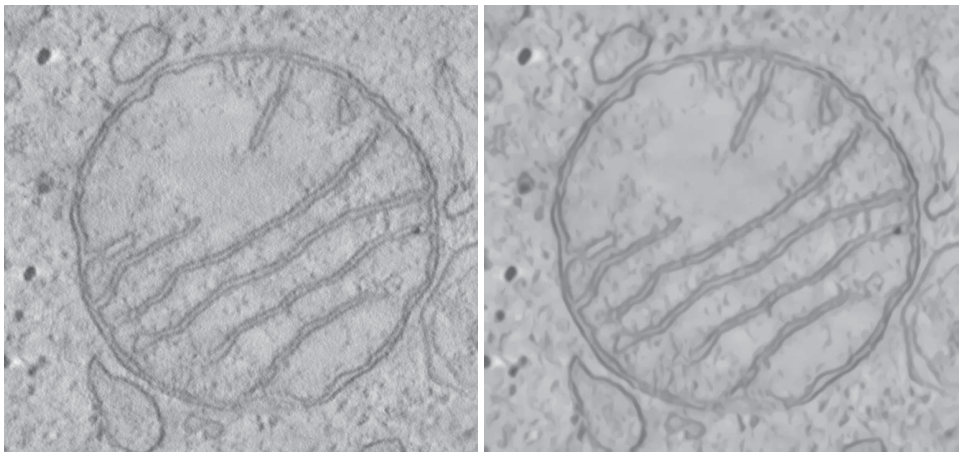

Figure 3.36: Results of the proposed approach as a slice taken from the 3D electron tomogram of the HeLa cell mitochondrion. (*left*) The noisy image. (*right*) The filtered image after applying the SED model. We observe the good denoising capability of the proposed approach along with its excellent ability of preserving the edges.

shows the successful extraction of both the crista structures and outer membrane of the mitochondrion image. Identification of the interior structures was conducted separately from the identification of the outer membrane due to the required opposite direction of contour evolution for each. In order that the initial contour expand to identify the inner structures ν was chosen to be -25 and the evolution required 53 iterations, whereas for the second initial contour, used to shrink and identify the outer membrane, η was chosen to be 10 and the evolution required 38 iterations. These selections allowed accurate visualization of the boundaries of interest. Note that the algorithm was run on the image in Fig. 3.37 (*left*) and the resulting contours have been displayed on the original electron tomogram image slice. The extracted contours are visualized in Fig. 3.38. The left panel shows the successful result of extracting both the outer membrane and the inner structures; in the right panel we show a 3D rendering of a 'stack' consisting of 25 extracted contours.

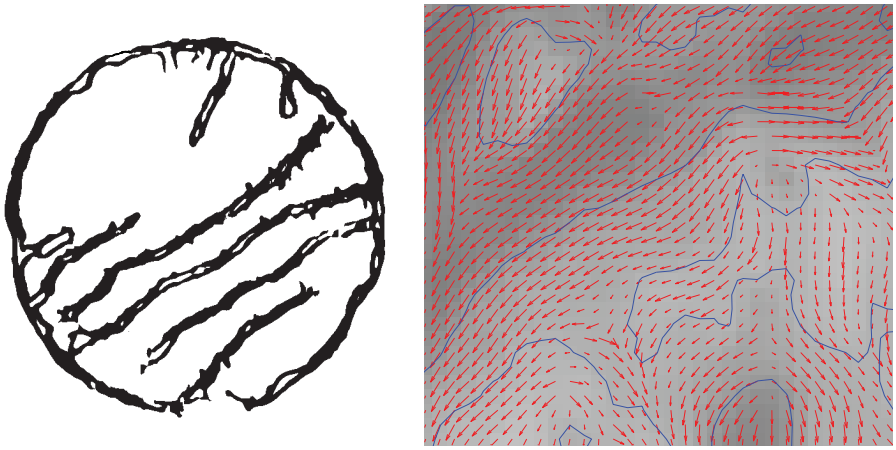

Figure 3.37: Results of the proposed approach as a slice taken from the 3D electron tomogram of the HeLa cell mitochondrion. (*left*) The image segmented with the 'confident connected' segmentation algorithm. (*right*) A fragment of the image's contours over which the structure tensor's term $\lambda_2 \mathbf{v}_2 \cdot \mathbf{v}_2^{\mathrm{T}}$ was superimposed.

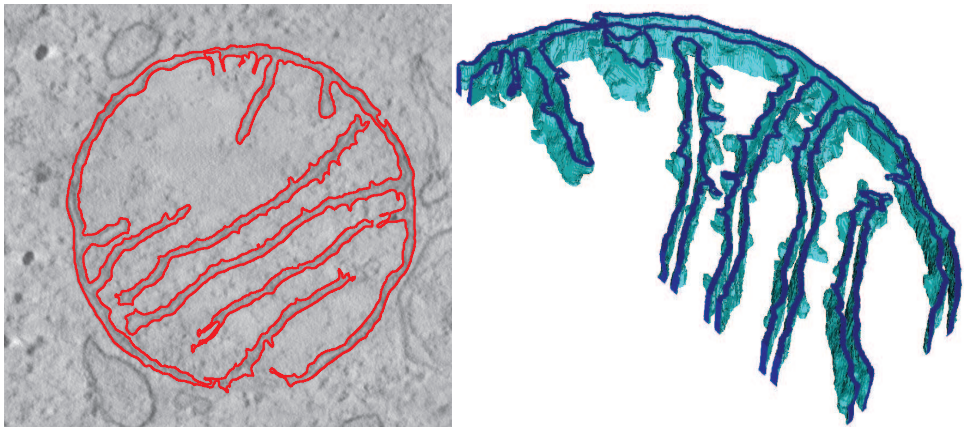

Figure 3.38: (*left*) Results of extraction of the interior structures and outer membrane of a mitochondrion in an ET image. Algorithm was applied twice to the segmented image (Fig. 3.36) using parameters: $\lambda = 5.0$, $\mu = 0.04$, $\tau = 5.0$, $\nu = -25$ for interior initial contour and $\nu = 10$ for outer initial contour. Final contours were plotted on the original ET image slice. (*right*) Fragment of the 3D rendering of the structural contours extracted from the mitochondrion image.

3.5 Concluding Remarks

We have presented a multi-stage approach for extracting the mitochondria structures from electron tomograms. In the initial restoration, or noise reduction phase, we propose a structure enhancing anisotropic nonlinear diffusion strategy: the local structure tensor $\mathbf{J}_{bf}$ is formed from the gradient information of a bilaterally smoothed version of the current image. In order to close gaps in structures caused by imaging limitations, the local structure tensor is further smoothed with a bilateral filter, forming a smoothed version of the structure tensor, $\overline{\mathbf{J}}_{bf}$. The eigenvectors $\mathbf{v}_i$, of the smoothed structure tensor form the basis for the diffusion tensor $\mathbf{D}_{bf}$, where the eigenvalues are prescribed so that there is a smooth interpolation, rather than a hard threshold switching of the diffusion characteristics between image areas of differing structure properties.

After the noise reduction phase, we synthetically enhance the contrast by applying the confident-connected segmentation algorithm. Following which, structures are extracted using a level set formulation which includes a term that drives the level set function toward a signed distance function. This both simplifies the initialization of the algorithm and removes the need for re-initialization. The results are very encouraging and this computational approach is potentially much faster, and is more robust and unbiased than the hand-tracing of structures.

Chapter 4

Total Variation-Based Models

4.1 Introduction

Rudin, Osher and Fatemi [314] proposed removing noise from images by minimizing the total variation (TV) norm of the estimated solution[1]. They derived a constrained minimization algorithm as a time-dependent nonlinear PDE, where the constraints are determined by the noise statistics. They stated that the space of bounded (total) variation (BV) is the proper class for many basic image processing tasks. Thus, given a noisy image $u_0 = f + \eta$, where the true image f has been perturbed by additive white noise η, the restored image $u \approx f$ is the solution of

$$\min_{u \in \mathrm{BV}(\Omega)} \mathrm{TV}\left(u\right) = \min_{u \in BV(\Omega)} \int_{\Omega} \left|\nabla u\right| d\mathbf{x}, \tag{4.1}$$

subject to the following constraints involving the noise:

$$\begin{aligned} \frac{1}{2} \int_{\Omega} \left(u - u_0\right)^2 d\mathbf{x} &= \frac{1}{2} \left|\Omega\right| \sigma^2, \\ \frac{1}{\left|\Omega\right|} \int_{\Omega} u_0 d\mathbf{x} &= \frac{1}{\left|\Omega\right|} \int_{\Omega} u d\mathbf{x}. \end{aligned} \tag{4.2}$$

The first constraint uses *a priori* information that the standard deviation of the noise is σ, while the second constraint assumes that the noise has zero mean[2]. The TV-

[1] The TV-based image noise removal model was originally developed in the late 80's [313] and the method was used by the U.S. Government.

[2] It can also be shown that Eqs. (4.1) and (4.2) imply that the noise is normally distributed [64].

norm does not penalize discontinuities in u, and therefore it allows the recovery of the edges in the observed image u_0.

To solve this minimization problem we would usually solve its Euler-Lagrange equation (see complete derivation in Appendix C), namely

$$-\nabla \cdot \left(\frac{\nabla u}{|\nabla u|} \right) + \lambda \left(u - u_0 \right) = 0, \tag{4.3}$$

on a closed domain Ω, and subject to homogeneous Neumann boundary conditions on the boundary $\partial\Omega$. The solution procedure proposed in [314] employs a parabolic equation with time as an evolution (scale) parameter, or equivalently, the gradient descent method, *i.e.*,

$$u_t - \nabla \cdot \left(\frac{\nabla u}{|\nabla u|} \right) + \lambda \left(u - u_0 \right) = 0, \tag{4.4}$$

for $t > 0$, on a closed domain Ω, with the observed image as initial condition, $u\left(\mathbf{x}, 0\right) = u_0\left(\mathbf{x}\right)$, and homogeneous Neumann boundary conditions, $\left\langle g \cdot \nabla u, \mathbf{n} \right\rangle = 0$, on the boundary $\partial\Omega$. For the parameter λ, they suggested a dynamic value $\lambda\left(t\right)$ estimated by Rosen's gradient-projection method, which as $t \to \infty$ converges to

$$\lambda = -\frac{1}{2\left|\Omega\right|\sigma^2} \int_{\Omega} \left[\left|\nabla u\right| - \frac{\nabla u_0^{\mathrm{T}} \nabla u}{\left|\nabla u\right|} \right] d\mathbf{x}. \tag{4.5}$$

Existence and uniqueness results for this nonlinear PDE have been obtained by Lions, Osher and Rudin [213]. Other successful implementations of this minimization problem include the second order cone programming [144], convex programming [72], duality [63], and a fast and exact minimization method based on graph cuts [79, 80].

4.2 Total Variation-Based Models in Image Processing

Rudin, Lions and Osher [312] have argued that there is a number of reasons for preferring TV-based models over their counterparts. TV-based algorithms are relatively

simple to implement and result in minimal ringing (non-oscillatory) while recovering sharp edges (noninvasive). In other words, the TV-norm allows piecewise smooth functions with jumps and is the proper space for the analysis and recovery of discontinuous functions. Also, the TV-based formulations make *a priori* assumptions about the noise, and therefore they can be tailored to address the specific image restoration problem at hand. Furthermore, empirical evidence suggests that 'the human vision favors the L^1-norm' [84]. In other words, the TV-based formulations seem to be the proper approach for restoring piecewise continuous functions from noisy and blurry signals.

Nonetheless, the Rudin-Osher-Fatemi model, in its original form, presents several practical challenges [2]. This evolution scheme is not trivial to implement since it is highly nonlinear and not well-posed [332]. When the scheme converges it does it at a linear rate[3]. It can also run into trouble when $|\nabla u| \to 0$ beyond machine accuracy. In practice, it is very common to use a slightly modified version of the TV-norm [2]

$$\int_{\Omega} \sqrt{|\nabla u|^2 + \varepsilon}\, d\mathbf{x}, \tag{4.6}$$

where ε is a small positive number which 'smoothes out the corner' at $|\nabla u| = 0$. The two other practical (observable) limitations presented by the Rudin-Osher-Fatemi original model are the loss of contrast [65, 342] and the 'staircase' effect, *i.e.*, a strong preference for piecewise constant patches [221, 228]. The Rudin-Osher-Fatemi model has been extensively studied and improved upon by many scientists [2, 44, 65, 69, 145, 208, 228, 276, 279, 312, 321, 332, 341, 342, 364, 365]. We will present here only the works that serve as background for our research. In our opinion, three of the most relevant improvements to the method were proposed by (i) Marquina and Osher [228], (ii) Blomgren, Chan and Mulet [44], and (iii) Rudin, Lions and Osher [312].

[3]The Courant-Friedrichs-Lewy (CFL) condition for the Rudin-Osher-Fatemi model is $\delta t / \delta x^2 \leqslant cF(|\nabla u|)$, with $c > 0$ [332].

(i) Marquina and Osher [228] proposed a different version of the transient parabolic equation that helps speed up the convergence of the time-marching scheme[4]. The new evolution equation is

$$u_t - |\nabla u| \nabla \cdot \left(\frac{\nabla u}{|\nabla u|} \right) + |\nabla u| \lambda G_\sigma * (G_\sigma * u - u_0) = 0, \tag{4.7}$$

for $t > 0$, on a closed domain Ω, with the observed image as initial condition, $u(\mathbf{x}, 0) = u_0(\mathbf{x})$, and homogeneous Neumann boundary conditions, $\langle g \cdot \nabla u, \mathbf{n} \rangle = 0$, on the boundary $\partial\Omega$, and where G_σ is a blurring operator (Gaussian kernel). This approach fixes the staircase problem of the original scheme and is used for the removal of both blur and noise.

(ii) Blomgren, Chan and Mulet [44] introduced a new approach that considers a regularizing functional of the type $\int |\nabla u|^p \, d\mathbf{x}$, for $p \in [1, 2]$. For an exponent $p = 1$, the model admits discontinuous solutions while when $p = 2$, it presents a strong bias against discontinuous functions. This approach was studied further in [332] where the following evolution equation was proposed

$$u_t - \nabla \cdot \left(|\nabla u|^{p-2} \nabla u \right) + \lambda (u - u_0) = 0, \tag{4.8}$$

for $t > 0$, on a closed domain Ω, with the observed image as initial condition, $u(\mathbf{x}, 0) = u_0(\mathbf{x})$, and homogeneous Neumann boundary conditions, $\langle g \cdot \nabla u, \mathbf{n} \rangle = 0$, on the boundary $\partial\Omega$. The proof of the uniqueness of the solution is given in [183].

Levine, Chen and Stanich [208] and Chen, Levine and Rao [69] proposed a variant to that of Blomgren, Chan and Mulet [44], where they defined the exponent p based on the observed data u_0. Their model is

$$\min_{u \in BV(\Omega) \cap L^2(\Omega)} \int_\Omega \varphi(\mathbf{x}, \nabla u) \, d\mathbf{x} + \frac{\lambda}{2} \int_\Omega |u - u_0|^2 \, d\mathbf{x},$$

[4]The CFL condition for the Marquina-Osher model is $\delta t / \delta x^2 \leqslant c$, with $c > 0$ [332].

where

$$\varphi(\mathbf{x}, r) = \begin{cases} \frac{1}{p(\mathbf{x})} |r|^{p(\mathbf{x})} & \text{if } |r| \leqslant \gamma \\ |r| - \frac{\gamma p(\mathbf{x}) - \gamma^{p(\mathbf{x})}}{p(\mathbf{x})} & \text{if } |r| > \gamma. \end{cases}$$

Here, $\gamma > 0$ is a fixed parameter, and $p(\mathbf{x})$ is based on a smoothed version of the observed image u_0,

$$p(\mathbf{x}) = \frac{1}{1 + \kappa |\nabla G_\sigma * u_0(\mathbf{x})|^2},$$

where κ is an adjustable parameter, and G_σ is a Gaussian smoothing kernel of width σ. They showed existence and uniqueness of minimizers for this functional, and developed a numerical method for computing them based on gradient descent.

Chambolle [63] also touched upon this subject where he combined two functionals $\int |\nabla u|$ and $\int |\nabla u|^2$ as

$$J(u) = \frac{1}{2\omega} \int_{|\nabla u| < \omega} |\nabla u|^2 \, d\mathbf{x} + \int_{|\nabla u| \geqslant \omega} \left(|\nabla u| - \frac{\omega}{2} \right) d\mathbf{x} + \int_\Omega |u - u_0|^2 \, d\mathbf{x},$$

where ω is an adjustable parameter to be chosen. The Euler-Lagrange equation for this functional resembles that of the models discussed in this section. Schults, Bollt, Chartrand, Esedoglu and Vixie [321] have more recently revisited the subject and suggested to minimize the following functional,

$$J(u) = \int_\Omega |\nabla u|^{p(|\nabla u|)} \, d\mathbf{x} + \frac{\lambda}{2} \int_\Omega |u - u_0|^q \, d\mathbf{x},$$

where $q = 1$ or 2, for two cases: Case 1, $p(\mathbf{x}) = P(|\nabla (G_\sigma * u_0)(\mathbf{x})|)$; and Case 2, $p(\mathbf{x}) = P(|\nabla (G_\sigma * u)(\mathbf{x})|)$. They proved existence in both cases, and uniqueness in the case of $q = 2$.

(iii) Rudin, Lions and Osher [312] developed TV-based constrained nonlinear PDEs to restore blurry images which have been further corrupted with multiplicative noise. In their theoretical results they proved existence and uniqueness of solutions to these problems. For the pure denoising problem, where the true image has been

perturbed by multiplicative noise, $u_0 = mf$, they considered the following constraints involving the noise

$$\int_\Omega m d\mathbf{x} = |\Omega|, \qquad \int_\Omega (m-1)^2 d\mathbf{x} = |\Omega|\,\sigma^2. \tag{4.9}$$

The gradient projection method leads to the evolution equation

$$u_t - \nabla \cdot \left(\frac{\nabla u}{|\nabla u|} \right) + \lambda_1 \frac{u_0^2}{u^3} + \lambda_2 \frac{u_0}{u^2} = 0, \tag{4.10}$$

for $t > 0$, on a closed domain Ω, with the observed image as initial condition, $u(\mathbf{x}, 0) = u_0(\mathbf{x})$, and homogeneous Neumann boundary conditions, $\langle g \cdot \nabla u, \mathbf{n} \rangle = 0$, on the boundary $\partial\Omega$. For the case of images perturbed by blur and multiplicative noise, $u_0 = mA * f$ and $u_0 = A * f + mf$, the two sets of constraints they used are

$$\begin{aligned}
&\int_\Omega \left(\frac{u_0}{A * f} \right) d\mathbf{x} = |\Omega|, \qquad \frac{1}{2} \int_\Omega \left(\frac{u_0}{A * f} - 1 \right)^2 d\mathbf{x} = \frac{1}{2} |\Omega|\,\sigma^2, && \text{(a)} \\
&\int_\Omega \left(\frac{u_0 - A * f}{u} \right) d\mathbf{x} = 0, \qquad \frac{1}{2} \int_\Omega \left(\frac{u_0 - A * f}{u} \right)^2 d\mathbf{x} = \frac{1}{2} |\Omega|\,\sigma^2. && \text{(b)}
\end{aligned} \tag{4.11}$$

In this case, the gradient projection method leads to the following evolution equations

$$\begin{aligned}
&u_t - \nabla \cdot \left(\frac{\nabla u}{|\nabla u|} \right) + \lambda_1 A * \left(\frac{u_0}{(A * u)^2} \right) \left(\frac{u_0}{A * u} - 1 \right) + \\
&\qquad + \lambda_2 A * \left(\frac{u_0}{(A * u)^2} \right) = 0, && \text{(a)} \\
&u_t - \nabla \cdot \left(\frac{\nabla u}{|\nabla u|} \right) + \lambda_1 \left[A * \left(\frac{u_0 - A * u}{u^2} \right) + \frac{(u_0 - A * u)^2}{u^3} \right] + \\
&\qquad + \lambda_2 \left[A * \left(\frac{1}{u} \right) + \frac{u_0 - A * u}{u^2} \right] = 0, && \text{(b)}
\end{aligned} \tag{4.12}$$

for $t > 0$, on a closed domain Ω, with the observed image as initial condition, $u(\mathbf{x}, 0) = u_0(\mathbf{x})$, and homogeneous Neumann boundary conditions, $\langle g \cdot \nabla u, \mathbf{n} \rangle = 0$, on the boundary $\partial\Omega$. We will discuss the multiplicative noise models later in this chapter.

4.2.1 Parameter-Free Adaptive Total Variation-Based Noise Removal and Edge Strengthening Model

In previous work [31] we implemented a variation of Blomgren, Chan and Mulet's [44] version of the Rudin, Osher and Fatemi's [314] Euler-Lagrange equation as modified by Marquina and Osher [228],

$$\begin{aligned} & u_t - |\nabla u| \, \nabla \cdot \left(\mathbf{D}_{bf} \left(|\nabla u|^{p-1} \right) \cdot \nabla u \right) + \Lambda \left(u - u_0 \right) = 0, \\ & \text{on } \ \Omega \times [\, 0, \infty) \,, \\ & u \left(\mathbf{x}, 0 \right) = u_0 \left(\mathbf{x} \right), \qquad \text{on } \ \Omega, \\ & \langle \mathbf{D}_{bf} \cdot \nabla u, \mathbf{n} \rangle = 0, \qquad \text{on } \ \partial\Omega \times (0, \infty) \,. \end{aligned} \tag{4.13}$$

The model can be regarded as an 'adaptive TV-based model with morphologic convection and anisotropic diffusion.' We devised a user-independent choosing of all the parameters in the model, which starts by estimating the unknown noise level. Given the assumption that the image has been perturbed by additive white noise, $u_0 = f + \eta$, and that this noise is independent from the signal, the variance of the noisy image must to be equal to the sum of the variance of the true image and the variance of the noise, *i.e.*, $\mathrm{var}\,(u_0) = \mathrm{var}\,(G_\sigma * u_0) + \mathrm{var}\,(\eta)$. Here, the variance of the (unknown) true image is approximated by the variance of the convolved noisy image with a Gaussian kernel of width $\sigma = 1$. This parameter will be updated at every iteration which provides a positive effect. (This is discussed later.) In Appendix D we show, experimentally, the good properties of this very simple approximation.

For the forcing-term's parameter we implemented a variation of the method suggested in [314]. Instead of integrating (or summing) over the domain Ω, we assume a pixel-wise parameter as

$$\Lambda \equiv |\nabla u| \, \lambda = -\frac{1}{2\sigma^2} \left[u_x \left(u_x - (u_0)_x \right) + u_y \left(u_y - (u_0)_y \right) \right]. \tag{4.14}$$

The dynamic parameter Λ has the following attributes:

(i) The smaller the value of Λ, the more the diffusion contributed by the forcing term. Analogously, the larger the value of Λ, the lesser the diffusion contributed by the forcing term.

(ii) At the beginning of the scale-marching iterations the gradients $u_x \approx (u_0)_x$, and $u_y \approx (u_0)_y$, therefore the terms $u_x - (u_0)_x$ and $u_y - (u_0)_y$ are very small, and the forcing term tends to contribute more to the diffusion process. In areas where u_x and u_y are large (*i.e.*, near edges), these values compensate for the small values of $u_x - (u_0)_x$ and $u_y - (u_0)_y$.

(iii) As iterations evolve the terms $u_x - (u_0)_x$ and $u_y - (u_0)_y$ get larger. Near edges, the forcing term prevents diffusion and helps reach convergence.

(iv) As iterations evolve, the approximation to the variance of the noise σ^2 gets smaller, provoking the dynamic parameter Λ to increase, which reduces the diffusion and helps reach convergence.

The diffusion tensor $\mathbf{D}_{bf}\left(|\nabla u|^{p-1}\right)$ incorporates the parameter $0 \leq p \leq 1$, similar to the approach in [45]. The diffusion tensor becomes

$$\mathbf{D}_{bf}\left(|\nabla u|^{p-1}\right) = \begin{bmatrix} \mathbf{v}_1 & \mathbf{v}_2 \end{bmatrix} \begin{bmatrix} |\nabla u|^{p_1-1} & 0 \\ 0 & |\nabla u|^{p_2-1} \end{bmatrix} \begin{bmatrix} \mathbf{v}_1^{\mathrm{T}} \\ \mathbf{v}_2^{\mathrm{T}} \end{bmatrix}, \tag{4.15}$$

where p_1 and p_2 are the following adaptive parameters

$$\begin{aligned} p_1 &= g\left(|\nabla u_{bf}|^2\right), \\ p_2 &= \begin{cases} g\left(|\nabla u_{bf}|^2\right) & \text{if } \mu_1 = \mu_2 \\ g\left(|\nabla u_{bf}|^2\right) + \left(1 - g\left(|\nabla u_{bf}|^2\right)\right) \exp\left(-C/(\mu_1 - \mu_2)^2\right) & \text{else.} \end{cases} \end{aligned} \tag{4.16}$$

The dynamic parameters p_1 and p_2 have the following attributes:

(i) For every pixel in the image the parameters take values $0 \leq p_1 \leq 1$, and $0 \leq p_2 \leq 1$.

(ii) When $p_1 = 0$ or $p_2 = 0$, the model uses the TV-norm for the diffusion in the corresponding direction, and when $p_1 = 1$ or $p_2 = 1$, the model uses the L^2-norm for the diffusion in the corresponding direction.

(iii) When the parameters $0 < p_1 < 1$ and $0 < p_2 < 1$, the model interpolates between both norms.

In Eqs. (4.15) and (4.16), $g\left(|\nabla u_{bf}|^2\right) = \left(1 + |\nabla u_{bf}|^2/\lambda^2\right)^{-1}$ is the Perona-Malik-type diffusivity, $\mathbf{v}_1$ and $\mathbf{v}_2$ are the corresponding eigenvectors to the eigenvalues $\mu_1 \geq \mu_2$ of the convolved structure tensor $\bar{\mathbf{J}}_{bf}$. The parameter C is set to 1/100 of the root-mean-square contrast of the image, *i.e.*, the coherence measure $(\mu_1 - \mu_2)^2$.

Due to the high nonlinearity of the TV-based models, to ensure stability, the required time step is very small. Song [332] has shown that the CFL condition for the Rudin-Osher-Fatemi model is $\delta t/\delta x^2 \leqslant c\,|\nabla u|$, with $c > 0$. He has also shown that the CFL condition for the Marquina-Osher model is $\delta t/\delta x^2 \leqslant c$, with $c > 0$. As a rule of thumb, Gilboa [140] has suggested (assuming $\delta \mathbf{x} = 1$) setting the value of $\delta t = \varepsilon/5$, where ε is the regularization constant used in Eq. (4.6). As mentioned in chapter 3, Weickert, Romeny and Viergever [381] have shown that for explicit discretization schemes, the stability condition for the Perona-Malik-type models (assuming $\delta \mathbf{x} = 1$ and $\forall s : g(s) \leqslant 1$) is $\delta t < 1/2d$, with d being the number of dimensions of the data. Since the explicit discretization schemes used in the TV-based models produce updates of the following form

$$u^{t+1} = u^t + \delta t F\left(u^t, \nabla u^t, u_0, \nabla u_0, \lambda\right), \tag{4.17}$$

then, in practice, the smaller the time-step, the slower the restoration process. We can use the aforementioned findings to devise an 'adaptive time-step' $\delta t\,(\mathbf{x}, t)$, that will not only make the TV-based schemes more stable (smooth), but will also speed up the restoration process. The proposed adaptive time-step is[5]

$$\delta t\,(\mathbf{x}) = \frac{\varepsilon}{5} + \left(\frac{1}{2d} - \frac{\varepsilon}{5}\right)\left(\frac{\max\left(|\nabla u|\right) - |\nabla u|}{\max\left(|\nabla u|\right)}\right), \qquad \forall\, t, \tag{4.18}$$

[5]We are assuming in this case that the image's dynamic range is $(0, 255)$.

where, as before, ε is the regularization constant used in Eq. (4.6), and d is the number of dimensions of the data. The adaptive time-step has the following characteristics:

(i) The size of the time step varies across the image, $\varepsilon/5 \leqslant \delta t\,(\mathbf{x}) \leqslant 1/2d$ at every iteration.

(ii) In regions with high gradients, $|\nabla u| \to \max(|\nabla u|)$, the time-step $\delta t \to \varepsilon/5$. This is a desirable feature since we want to preserve the edges.

(iii) In regions with low gradients, $|\nabla u| \to 0$, the time-step $\delta t \to 1/2d$. This is also a desirable feature since we want to smooth the isotropic regions as soon as possible.

(iv) In regions with moderate gradients, $0 < |\nabla u| < \max(|\nabla u|)$, the time step interpolates linearly between the two extremes[6], $\varepsilon/5 < \delta t\,(\mathbf{x}) < 1/2d$.

4.2.2 Numerical Experiments for the Parameter-Free Adaptive Total Variation-Based Noise Removal and Edge Strengthening Model, Image Processing

The experiment consisted in trying to restore the noise-free image f, by finding the best approximation $u \approx f$, that each restoration model can achieve. We assume that the noise-free image has been perturbed by additive Gaussian noise, $u_0 = f + \eta$, with zero mean and unknown variance. In order to compare the performance of the proposed model we implemented the two models below using finite differencing, and a simple performance measure based on the correlation between the noise-free image and the two filtered images[7]. Model 1 is the classic Marquina-Osher model from Eq.

[6]To keep consistency with the experiments in chapter 3, we adopt the upper bound for the time-step $10^{-2} \leqslant 1/2d$.

[7]We refer the reader to chapter 5 for a description of the algorithms to implement these models.

(4.7) with $G_\sigma = \mathbf{I}$ (no blur),

$$\begin{aligned} &u_t - |\nabla u| \nabla \cdot \left(\frac{\nabla u}{|\nabla u|} \right) + |\nabla u| \lambda (u - u_0) = 0, \qquad \text{on } \Omega \times [0, \infty), \\ &u(\mathbf{x}, 0) = u_0(\mathbf{x}), \qquad \text{on } \Omega, \\ &\langle g \cdot \nabla u, \mathbf{n} \rangle = 0, \qquad \text{on } \partial\Omega \times (0, \infty). \end{aligned} \tag{4.19}$$

Model 2 is the inhomogeneous version of the proposed model from Eq. (4.13). The full anisotropic version of Eq. (4.13) is only appropriate when edge strengthing is sought, and will not be comparable to Model 1. Then,

$$\begin{aligned} &u_t - |\nabla u| \nabla \cdot \left(\frac{\nabla u}{|\nabla u|} \right) + \Lambda (u - u_0) = 0, \qquad \text{on } \Omega \times [0, \infty), \\ &u(\mathbf{x}, 0) = u_0(\mathbf{x}), \qquad \text{on } \Omega, \\ &\langle g \cdot \nabla u, \mathbf{n} \rangle = 0, \qquad \text{on } \partial\Omega \times (0, \infty). \end{aligned} \tag{4.20}$$

We set the following parameters for the two models:

Table 4.1: Adopted Parameters in Experiments

Model 1	**Model 2**
$\varepsilon = 1/255$	$\varepsilon = 1/255$
$\delta t = \varepsilon/5$	$\delta t = \frac{\varepsilon}{5} + \left(\frac{1}{2d} - \frac{\varepsilon}{5}\right) \left(\frac{\max(\lvert\nabla u\rvert) - \lvert\nabla u\rvert}{\max(\lvert\nabla u\rvert)} \right)$
$\lambda = -\frac{1}{2\lvert\Omega\rvert\sigma^2} \int_\Omega \left[\lvert\nabla u\rvert - \frac{\nabla u_0^{\mathrm{T}} \nabla u}{\lvert\nabla u\rvert} \right] d\mathbf{x}$	$\Lambda = -\frac{1}{2\sigma^2} \nabla u^{\mathrm{T}} \cdot (\nabla u - \nabla u_0)$
$\mathrm{var}(\eta) = \mathrm{var}(u_0) - \mathrm{var}(G_\sigma * u_0)$	$\mathrm{var}(\eta^{t+1}) = \mathrm{var}(u^t) - \mathrm{var}(G_\sigma * u^t)$

We apply the standard explicit finite difference scheme with central difference to approximate the spatial derivatives, and forward difference to approximate the time derivative. Results of the experiment for the Clown are shown in Figs. 4.1, 4.2 and 4.3; results of the experiment for the Baboon are shown in Figs. 4.4, 4.5 and 4.6; results of the experiment for the Cameraman are shown in Figs. 4.7, 4.8 and 4.9. In all the cases, we notice that the proposed model provides an improvement in the

quality of the restoration and a huge speed-up in the time to reach the best possible restoration. A summary of the comparative results for the three images are shown in table 4.2.

Table 4.2: Comparative Results of the Experiments

Experiment	**Model 1**	**Model 2**
The Clown	Iterations = 1779 $\text{corr}\,(f,u) = 0.9700$	Iterations = 25 $\text{corr}\,(f,u) = 0.9736$
The Baboon	Iterations = 1296 $\text{corr}\,(f,u) = 0.8859$	Iterations = 19 $\text{corr}\,(f,u) = 0.8965$
The Cameraman	Iterations = 1548 $\text{corr}\,(f,u) = 0.9647$	Iterations = 28 $\text{corr}\,(f,u) = 0.9740$

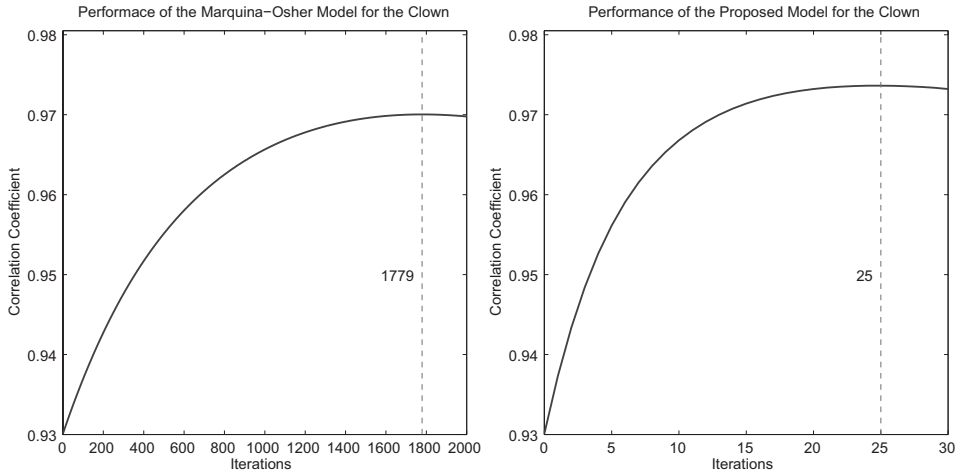

Figure 4.1: (*left*) Correlation coefficient between the noise-free image of the Clown and the filtered image of the Clown at each iteration, $\text{corr}\,(f,u)$, after applying the Marquina-Osher model. (*right*) Correlation coefficient between the noise-free image of the Clown and the filtered image of the Clown at each iteration, $\text{corr}\,(f,u)$, after applying the proposed model. The maximum value of the correlation coefficient for each model is as follows: Marquina-Osher, 0.9700, after 1779 iterations; proposed model, 0.9736, after 25 iterations.

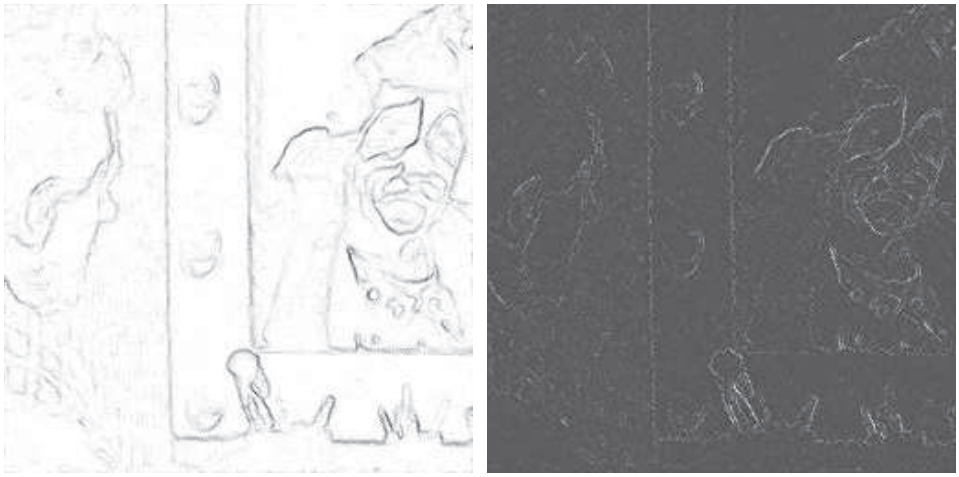

Figure 4.2: (*left*) Values of the time-step δt across the image after applying the proposed model for 25 iterations. Larger time-steps are taken in the isotropic areas of the image (faster update), and smaller time-steps are taken on and near the edges (slower update). (*right*) Values of the parameter Λ across the image after applying the proposed model for 25 iterations. This parameter is larger on and near edges (less diffusion), and it is smaller in the isotropic areas of the image (more diffusion).

Figure 4.3: (*left to right*) Filtered images of the Clown by the Marquina-Osher model and the proposed model. The maximum correlation coefficients between the noise-free image and the filtered images, $\mathrm{corr}\,(f, u)$, are 0.9700 and 0.9736, respectively.

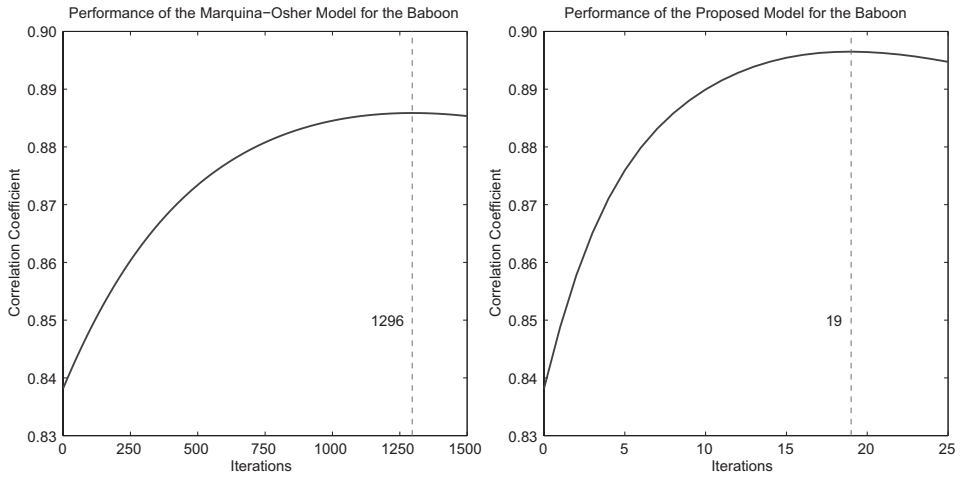

Figure 4.4: (*left*) Correlation coefficient between the noise-free image of the Baboon and the filtered image of the Baboon at each iteration, $\mathrm{corr}\,(f, u)$, after applying the Marquina-Osher model. (*right*) Correlation coefficient between the noise-free image of the Baboon and the filtered image of the Baboon at each iteration, $\mathrm{corr}\,(f, u)$, after applying the proposed model. The maximum value of the correlation coefficient for each model is as follows: Marquina-Osher, 0.8859, after 1296 iterations; proposed model, 0.8965, after 19 iterations.

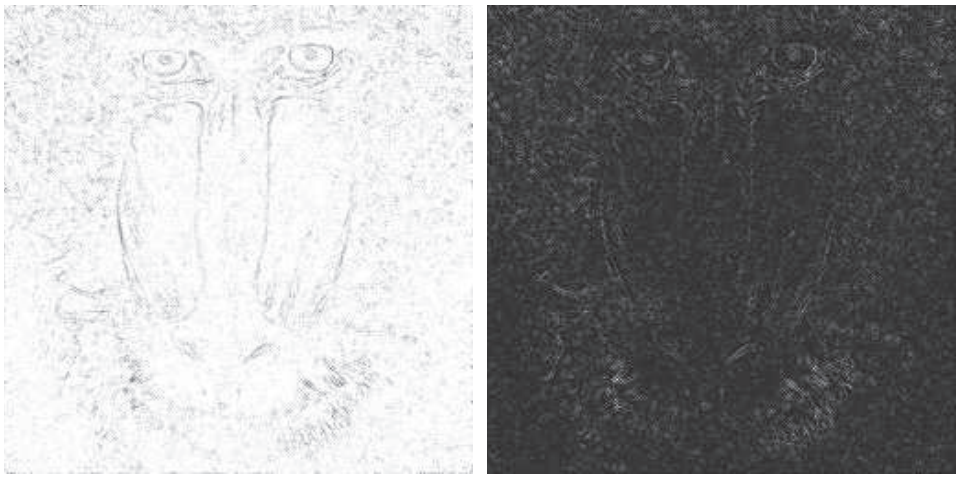

Figure 4.5: (*left*) Values of the time-step δt across the image after applying the proposed model for 19 iterations. Larger time-steps are taken in the isotropic areas of the image (faster update), and smaller time-steps are taken on and near the edges (slower update). (*right*) Values of the parameter Λ across the image after applying the proposed model for 19 iterations. This parameter is larger on and near edges (less diffusion), and it is smaller in the homogeneous areas of the image (more diffusion).

Figure 4.6: (*left to right*) Filtered images of the Baboon by the Marquina-Osher model and the proposed model. The maximum correlation coefficients between the noise-free image and the filtered images, $\mathrm{corr}\,(f, u)$, are 0.8859 and 0.8965, respectively.

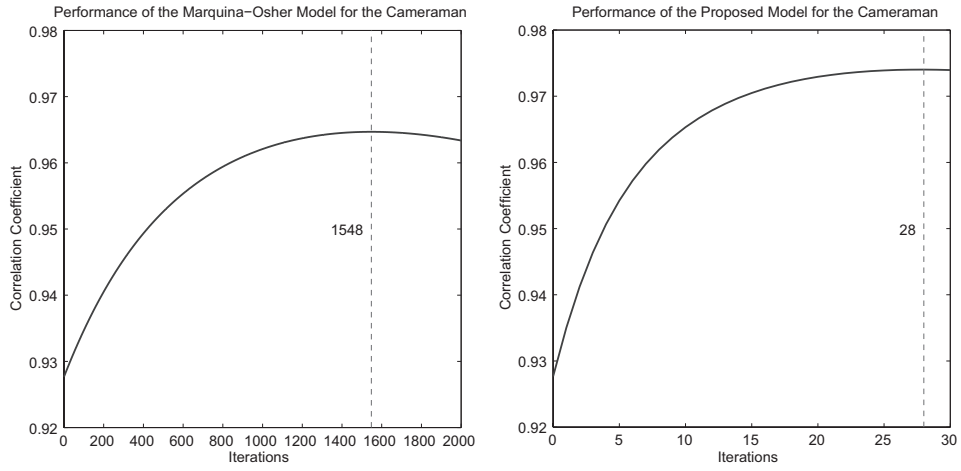

Figure 4.7: (*left*) Correlation coefficient between the noise-free image of the Cameraman and the filtered image of the Cameraman at each iteration, $\mathrm{corr}\,(f, u)$, after applying the Marquina-Osher model. (*right*) Correlation coefficient between the noise-free image of the Cameraman and the filtered image of the Cameraman at each iteration, $\mathrm{corr}\,(f, u)$, after applying the proposed model. The maximum value of the correlation coefficient for each model is as follows: Marquina-Osher, 0.9647, after 1548 iterations; proposed model, 0.9740, after 28 iterations.

Figure 4.8: (*left*) Values of the time-step δt across the image after applying the proposed model for 28 iterations. Larger time-steps are taken in the isotropic areas of the image (faster update), and smaller time-steps are taken on and near the edges (slower update). (*right*) Values of the parameter Λ across the image after applying the proposed model for 28 iterations. This parameter is larger on and near edges (less diffusion), and it is smaller in the homogeneous areas of the image (more diffusion).

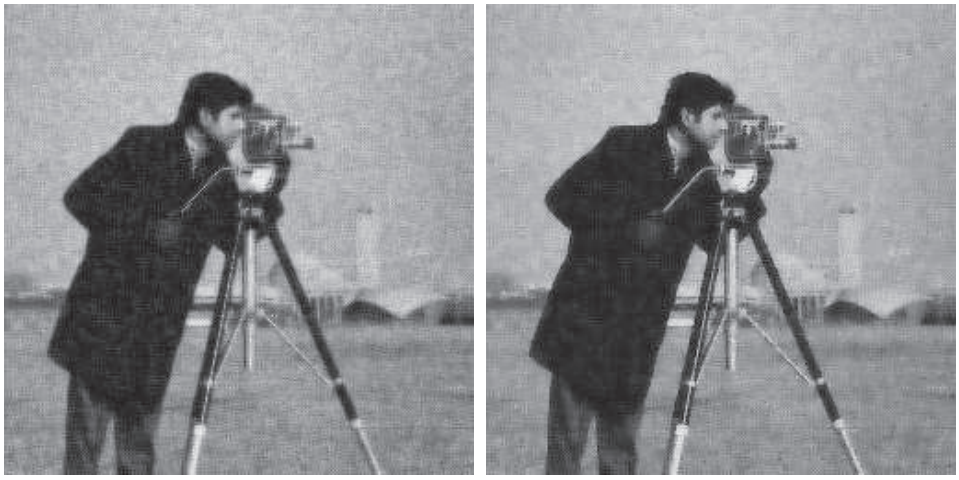

Figure 4.9: (*left to right*) Filtered images of the Cameraman by the Marquina-Osher model and the proposed model. The maximum correlation coefficients between the noise-free image and the filtered images, $\mathrm{corr}\,(f, u)$, are 0.9647 and 0.9740, respectively.

4.3 Total Variation-Based Models in Electron Tomography

To the best of our knowledge, the TV-based models introduced to the field of tomographic imaging were applied only during the 3D reconstruction processes. They were primarily employed for regularizing the severe ill-posedness present in the inverse problem. None of the applications we have found in the literature were used for the purpose of removing the noise while preserving edges from the 3D tomogram. Some of the TV-based models used in tomographic imaging are:

(i) Jonsson, Huang and Chan [179] introduced TV regularization in positron emission tomography (PET). They modified the standard expectation maximization (EM) for PET to incorporate the TV regularization which resulted in a robust algorithm independent of the amount of regularization. The authors in [179] argued that their TV-regularized EM-algorithm is far better that the standard EM-method when it comes to convergence and enhancement of object edges, better than the standard EM-method at reconstructing large flat regions, and comparable to the standard EM-method for smaller constant intensity regions.

(ii) Panin, Zeng and Gullberg [281] proposed a similar approach as above, in the form of an iterative Bayesian reconstruction where the regularization norm is included in the one step late-expectation maximization (OSL-EM) algorithm. They extended the TV-norm minimization constraint to the field of single positron emission computed tomography (SPECT) image reconstruction with a Poisson noise model. This TV regularization scheme, when apply to SPECT, provides reconstructed images that have attractive features, such as the identification of distinguishable sharp edges.

(iii) Persson, Bone and Elmqvist [296] extended the TV-norm formulation from 2D to 3D and incorporated it into an ordered subsets EM algorithm for limited view

angle acquisition geometry in gamma camera imaging (ectomography). They called their algorithm TV3D-EM, and evaluated it using a modeled point spread function and digital phantoms. The reconstructed images, when compared with those reconstructed with the 2D filtered back-projection algorithm, show perceived improvement in quality. The TV3D-EM yielded a reduction in artifacts, caused by the incomplete angular sampling of a limited view angle system, while the noise level was controlled.

(iv) Kisilev, Zibulevsky and Zeevi [188] incorporated the wavelet transform (WT) and TV based regularization procedures into the maximum likelihood (ML) framework, embedded into the iterative processes (reconstruction processes) of the EM algorithm and the conjugate barrier (CB) algorithm for PET. They concluded that the combination of the CB algorithm with the TV penalty achieves the best contrast to noise trade-off, and that it improves the contrast and suppresses noise simultaneously.

(v) Zhang and Froment [402] developed a Fourier-based tomographic reconstruction and TV-regularization method from given parallel x-ray projections. Their experiments on the well-known Shepp-Logan head phantom [325], show that this approach outperforms the following classic reconstruction methods both in terms of PSNR (an objective mean-square error) and visual quality: direct Fourier method (DFM), filtered back-projection, and Tikhonov iterative method (TIM).

(vi) Sidky, Kao and Pan [326] developed and investigated an iterative image reconstruction algorithm based on the minimization of the image TV-norm that applies to both fan-beam and cone-beam computed tomography (CT). This model aims to reconstruct images from sparse or insufficient data problems that may occur due to practical issues of CT scanning (including the few-view, limited-angle, and bad-bin problems). The minimization of the image TV is carried out by the gradient descent method, and the constraints imposed by the known projection data are incorporated

by projection on convex sets (POCS) [28]. They demonstrated and validated the proposed TV algorithm for image reconstruction in various sparse or insufficient data under 'ideal' conditions. Also, they presented preliminary results indicating that the TV algorithm seems to be effective on sparse data problems in the presence of signal noise.

(vii) Asaki, Campbell, Chartrand, Powell, Vixie and Wohlberg [14] applied TV regularization methods to Abel inversion tomography. Their experimental results showed favorable characteristics of noise suppression and density discontinuity preservation. They also introduced an adaptive TV method that employs a modified discrete gradient operator acting only apart from data-determined density discontinuities. The authors is [14] claim that this method provides improved density level preservation relative to the basic TV method.

We introduced a TV-based model for the reduction of noise and the strengthening of edges (structures) in cryo-electron tomograms [31, 34]. Our implementation uses the approach presented in subsection 4.2.1 where we devised a variation of Blomgren, Chan and Mulet's [44] version of the Rudin, Osher and Fatemi's [314] Euler-Lagrange equation as modified by Marquina and Osher [228]. It provides a user-independent method for choosing all the parameters in the model, along with an adaptive time-step that allows faster and more stable image restoration. Some experimental results are shown in subsection 4.3.1 where we applied the proposed model to the electron tomogram of a mitochondrion from a HeLa cell.

4.3.1 Numerical Experiments for the Parameter-Free Adaptive Total Variation-Based Noise Removal and Edge Strengthening Model, Electron Tomography

We applied the parameter-free adaptive TV-based noise removal and edge strengthening model, Eq. (4.13), to 2D slices of a 3D electron tomogram of a mitochondrion from a HeLa cell. The evolution model is as follows[8]:

$$
\begin{aligned}
& u_t - |\nabla u| \, \nabla \cdot \left(\mathbf{D}_{bf} \left(|\nabla u|^{p-1} \right) \cdot \nabla u \right) + \Lambda G_\sigma * (G_\sigma * u - u_0) = 0, \\
& \text{on } \ \Omega \times [\, 0, \infty) \,, \\
& u \, (\mathbf{x}, 0) = u_0 \, (\mathbf{x}) \,, \qquad \text{on } \ \Omega, \\
& \langle \mathbf{D}_{bf} \cdot \nabla u, \mathbf{n} \rangle = 0, \qquad \text{on } \ \partial\Omega \times (0, \infty) \,.
\end{aligned}
$$

The diffusion tensor $\mathbf{D}_{bf}$ is given by Eq. (4.15), the adaptive parameters p_1 and p_2 are defined by Eq. (4.16), and the adaptive time-step δt is described by Eq. (4.18). Fig. 4.10 shows the noisy 2D slice of a 3D electron tomogram of a mitochondrion from a HeLa cell, and the corresponding filtered image, after applying the parameter-free adaptive TV-based noise removal and edge strengthening model. We observe the good performance of the model at removing the high frequency signal with careful preservation of the edges.

4.3.2 Homomorphic Total Variation-Based Model

In this subsection we use TV-based methods for the reduction of multiplicative noise and the enhancement of structures in images from ET. These methods are used prior to applying image segmentation techniques that facilitate the 3D rendering and subsequence analysis of the mitochondrial structure. We design an algorithm based on the classic TV-based method by Rudin, Osher and Fatemi [314] as modified by Marquina and Osher [228] within a homomorphic system, and compare it to the TV-based image

[8] We refer the reader to chapter 5 for a description of the algorithm to implement this model.

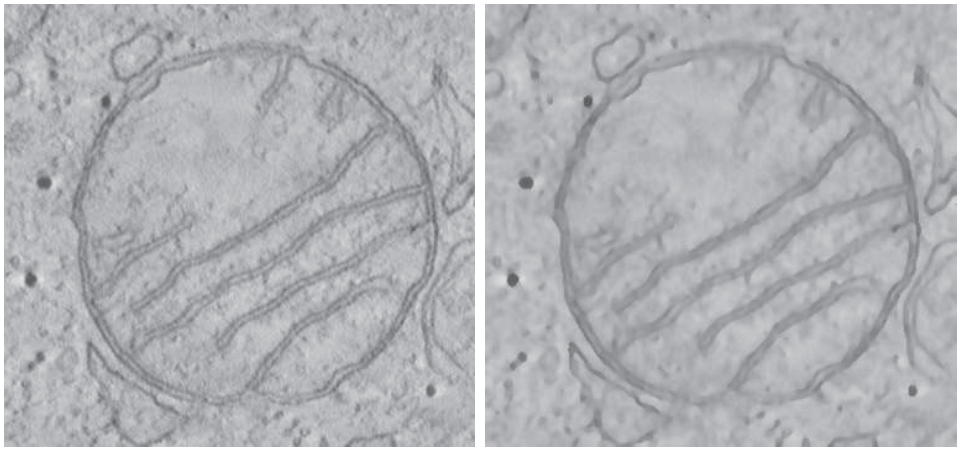

Figure 4.10: (*left to right*) Noisy 2D slice of a 3D electron tomogram of a mitochondrion from a HeLa cell, and the filtered 2D slice of a 3D electron tomogram of a mitochondrion from a HeLa cell, after applying the parameter-free adaptive TV-based noise removal and edge strengthening model.

restoration technique by Rudin, Lions and Osher [312] at reducing the multiplicative noise present in EM imagery. In a homomorphic system, the natural logarithm is used to transform the multiplicative nature of the degradation into an additive one and then, the resulting degraded image is processed by using a filter to reduce the additive noise. An exponential function is then applied to the output of the filter.

We will use an approach similar to the one presented in subsection 2.6.2 for our 'homomorphic TV-based image denoising technique.' The equation we are trying to solve is the low-dose imaging problem, $u_0(\mathbf{x}) = m(\mathbf{x})\, f(\mathbf{x})$, where u_0 is the observed degraded image, f is the true image, and m is the multiplicative noise with unit-mean following a Gamma (or Log-normal) probability distribution. Applying the natural logarithmic transform we obtain $\bar{u}_0(\mathbf{x}) = \bar{f}(\mathbf{x}) + \bar{\eta}(\mathbf{x})$, were $\bar{\eta}$ is a random zero-mean noise process [350] (very close to Gaussian distribution [1, 98, 155]) and $\bar{f} = \ln f + \mu_{\bar{m}}$. The variance and mean of $\bar{m}$ have been derived in [397] and for our particular case, $L = 61$, that results in $\mu_{\bar{m}} = -0.008219116123108$ and $\sigma^2_{\bar{m}} = 0.016528549339858$.

For our second TV-based implementation [312], we solve the equation $u_0(\mathbf{x}) =$

$m(\mathbf{x})\, f(\mathbf{x})$ in its original form. In doing so, we try to find $u \approx f$ by minimizing the TV of the image, $\min_{u \in BV(\Omega)} \int_\Omega |\nabla u|\, d\mathbf{x}$, subject to the following constraints involving the statistics of the noise

$$\int m = 1, \quad \forall u \qquad \text{or} \qquad \int_\Omega m = |\Omega|\,, \tag{4.21}$$

$$\int (m-1)^2 = \sigma_m^2, \quad \forall u \qquad \text{or} \qquad \int_\Omega (m-1)^2 = |\Omega|\, \sigma_m^2. \tag{4.22}$$

Constraint (4.21) is necessary to account for the case of a noise–free image, while constraint (4.22) is a direct consequence of (4.21) and implies that the standard deviation of the noise, σ_m, is known *a priori*. Thus, the constrained optimization is subject to the following constraints

$$\int \frac{u_0}{u} = 1, \tag{4.23}$$

$$\frac{1}{2}\int \left(\frac{u_0}{f} - 1\right)^2 = \frac{1}{2}\int \left(\left(\frac{u_0}{u}\right)^2 - 1\right) = \frac{\sigma_m^2}{2}. \tag{4.24}$$

The gradient projection method leads to Eq. (4.10) which we rewrite here for convenience

$$u_t - \nabla \cdot \left(\frac{\nabla u}{|\nabla u|}\right) + \lambda_1 \frac{u_0^2}{u^3} + \lambda_2 \frac{u_0}{u^2} = 0, \tag{4.25}$$

for $t > 0$, on a closed domain Ω, with the observed image as initial condition, $u(\mathbf{x}, 0) = u_0(\mathbf{x})$, and homogeneous Neumann boundary conditions, $\langle g \cdot \nabla u, \mathbf{n} \rangle = 0$, on the boundary $\partial\Omega$. We now have two Lagrange multipliers, λ_1 and λ_2, which can be computed by requiring

$$\begin{aligned} &\frac{\partial}{\partial t}\int \frac{u_0}{u} = -\int \frac{u_0}{u^2}\, u_t = 0, \quad \forall u \\ \text{or} \qquad &\frac{\partial}{\partial t}\int_\Omega \left(\frac{u_0}{u}\right) d\mathbf{x} = \int_\Omega \left(\frac{u_0}{u^2}\, u_t\right) d\mathbf{x} = 0, \end{aligned} \tag{4.26}$$

$$\begin{aligned} &\frac{\partial}{\partial t}\int \left(\left(\frac{u_0}{u}\right)^2 - 1\right) = -\int \frac{u_0^2}{u^3}\, u_t = 0, \quad \forall u \\ \text{or} \qquad &\frac{\partial}{\partial t}\int_\Omega \left(\left(\frac{f}{u}\right)^2 - 1\right) d\mathbf{x} = \int_\Omega \left(\frac{u_0^2}{u^3}\, u_t\right) d\mathbf{x} = 0. \end{aligned} \tag{4.27}$$

Eqs. (4.26) and (4.27), together with (4.25), lead to two algebraic equations for the two unknowns, λ_1 and λ_2, and the resulting Gram determinant is nonzero [312]. (See Appendix E for the derivation of λ_1 and λ_2.)

4.3.3 Numerical Experiments for the Homomorphic Total Variation-Based Model

For the homomorphic TV-based model we implement the following system[9]:

$$
\begin{aligned}
&u_t - |\nabla u| \nabla \cdot \left(\frac{\nabla u}{|\nabla u|} \right) + \Lambda G_\sigma * (G_\sigma * u - u_0) = 0, \qquad \text{on } \Omega \times [0, \infty), \\
&u(\mathbf{x}, 0) = u_0(\mathbf{x}), \qquad \text{on } \Omega, \\
&\langle g \cdot \nabla u, \mathbf{n} \rangle = 0, \qquad \text{on } \partial\Omega \times (0, \infty).
\end{aligned}
$$

The parameter Λ is the one we suggested in Eq. (4.14) and for the standard deviation of the noise, $\sigma_{\bar{\eta}}$, we used $\sigma_{\bar{m}}$, since $\text{var}(\bar{\eta}) = \text{var}(\bar{m} - \mu_{\bar{m}}) = \text{var}(\bar{m})$. We need to correct the output u to account for the applied shift $\bar{f} = \ln f + \mu_{\bar{m}}$, and then apply the exponential transformation to obtain the final approximation to the true image.

For the TV-based multiplicative noise removal case we implement the Rudin-Lions-Osher model [312]

$$
\begin{aligned}
&u_t - \nabla \cdot \left(\frac{\nabla u}{|\nabla u|} \right) + \lambda_1 \frac{u_0^2}{u^3} + \lambda_2 \frac{u_0}{u^2} = 0, \qquad \text{on } \Omega \times [0, \infty), \\
&u(\mathbf{x}, 0) = u_0(\mathbf{x}), \qquad \text{on } \Omega, \\
&\langle g \cdot \nabla u, \mathbf{n} \rangle = 0, \qquad \text{on } \partial\Omega \times (0, \infty).
\end{aligned}
$$

For the parameters λ_1 and λ_2 we solved the two equations with two unknowns and obtained (see Appendix E)

$$
\lambda_1(t) = \frac{1}{D(\mathbf{x})} \left(\int_\Omega \frac{u_0^2}{u^4} d\mathbf{x} \int_\Omega \frac{u_0^2}{u^3} B(\mathbf{x}) \, d\mathbf{x} - \int_\Omega \frac{u_0^3}{u^5} d\mathbf{x} \int_\Omega \frac{u_0}{u^2} B(\mathbf{x}) \, d\mathbf{x} \right),
$$

$$
\lambda_2(t) = \frac{1}{D(\mathbf{x})} \left(\int_\Omega \frac{u_0^4}{u^6} d\mathbf{x} \int_\Omega \frac{u_0}{u^2} B(\mathbf{x} d\mathbf{x}) \, d\mathbf{x} - \int_\Omega \frac{u_0^3}{u^5} d\mathbf{x} \int_\Omega \frac{u_0^2}{u^3} B(\mathbf{x}) \, d\mathbf{x} \right),
$$

[9] We refer the reader to chapter 5 for a description of the algorithm to implement this model.

where

$$D(\mathbf{x}) = \int_\Omega \frac{u_0^4}{u^6} d\mathbf{x} \int_\Omega \frac{u_0^2}{u^4} d\mathbf{x} - \int_\Omega \frac{u_0^3}{u^5} d\mathbf{x} \int_\Omega \frac{u_0^3}{u^5} d\mathbf{x}, \qquad B(\mathbf{x}) = \nabla \cdot \left(\frac{\nabla u}{|\nabla u|} \right).$$

Fig. 4.11 shows a 2D slice of a 3D electron tomogram of a mitochondrion obtained by low-dose imaging. In this case, the dynamic range of the image is very narrow and the image is predominantly perturbed by multiplicative noise. The resulting images after applying the two techniques we described above are shown in Figs. 4.12 and 4.13. We can observe that both images are better suited for automatic segmentation.

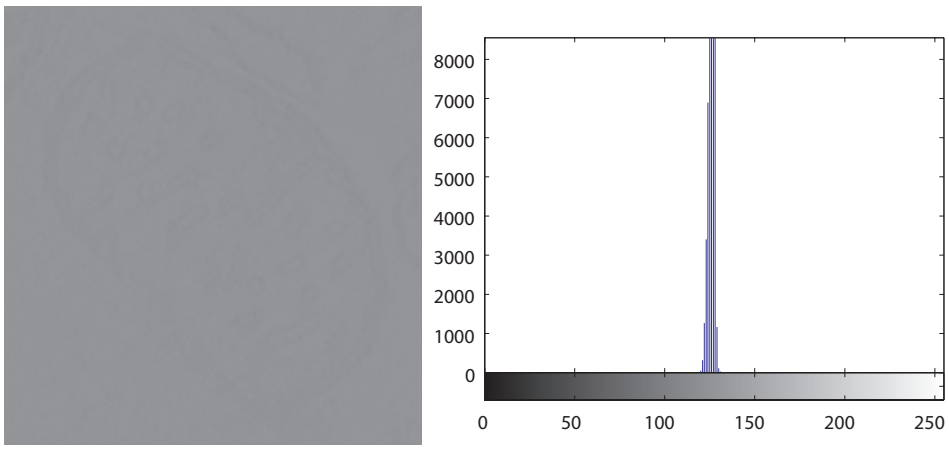

Figure 4.11: (*left to right*) Low-dose noisy 2D slice of a 3D electron tomogram of a mitochondrion and the histogram plot of its dynamic range. The dynamic range is extremely narrow as a consequence on the low contrast between ice and specimen.

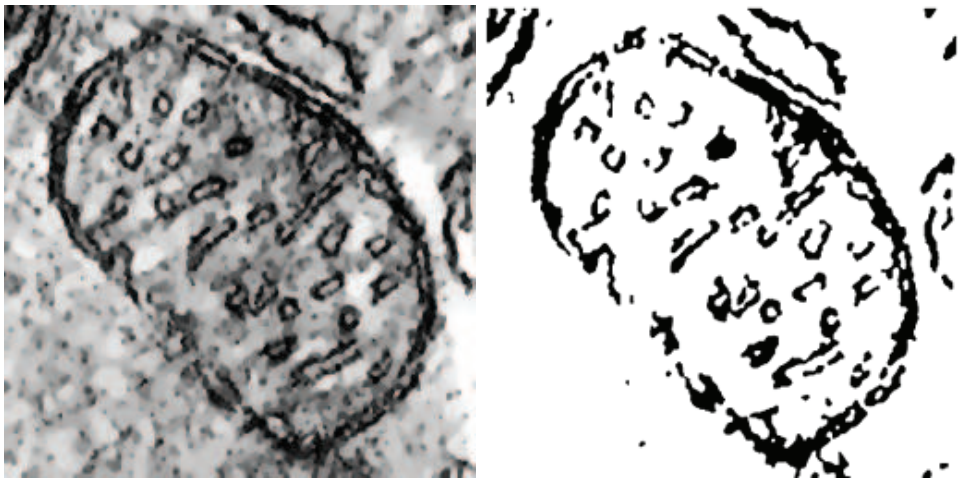

Figure 4.12: (*left*) Output image obtained by applying the homomorphic TV-based denoising after gamma correction. We can observe that the image is better suited for automatic segmentation. (*right*) Segmented image using a threshold algorithm that allows the extraction of the mitochondrion structure.

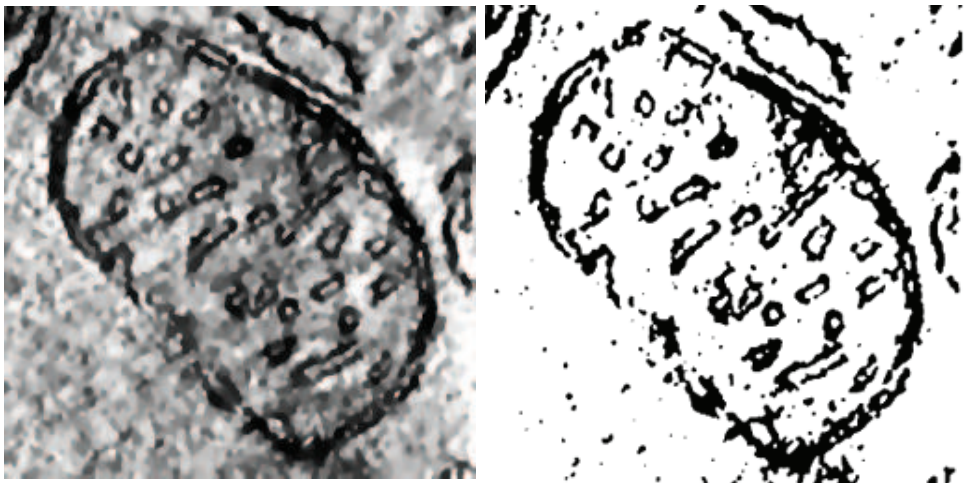

Figure 4.13: (*left*) Output image obtained by applying the TV-based denoising method for multiplicative noise after gamma correction. We can observe that the image is better suited for automatic segmentation. (*right*) Segmented image that allows the extraction of the mitochondrion structure.

4.4 Concluding Remarks

We developed a fully adaptive TV-based model with morphologic convection and anisotropic diffusion, and devised a user-independent choosing of all the parameters in the model. We start by estimating the unknown noise level via a simple approximation that uses convolution with a Gaussian kernel. This parameter is updated at each iteration and as the noise is being removed, it reduces the diffusion and helps reach convergence. For this model, we implemented a pixel-wise parameter in the forcing-term that allows more diffusion in homogeneous areas and restricts the diffusion in areas with higher probability of belonging to edges. This parameter also allows more diffusion in the early stages of the scale-marching process and less diffusion as iterations evolve. These are desirable attributes in image noise removal applications. For the anisotropic diffusion process, the diffusion tensor that we implemented not only steers the diffusion in such a way that the eigenvectors prescribe the diffusion directions and the corresponding eigenvalues determine the amount of diffusion along these directions, but also adapts itself to the underlying structure of the image, by applying a range of diffusion processes in each direction. The proposed model applies diffusion processes consistent with either the TV-norm or the L^2-norm, or an interpolation between the two norms. Finally, we implemented an adaptive time-step that helps with the stability and the speed of TV-based restoration process. The size of the time-step varies across the image at each iteration. Also, the adaptive time-step is smaller in regions with high gradients and is larger in regions with low gradients. Both of these are desirable features for preserving the edges and for smoothing isotropic regions, respectively.

In addition to the aforementioned TV-based model, we designed a homomorphic TV-based algorithm for the reduction of the multiplicative noise present in low-dose

EM imagery. In a homomorphic system, the natural logarithm is used to transform the multiplicative nature of the degradation into an additive one and then, the resulting degraded image is processed by using a filter to reduce the additive noise. An exponential function is then applied to the output of the filter. In the implementation of this model we employed some of the adaptive parameters we devised in the first part of the chapter. For the purpose of performance comparison, we implemented a TV-based algorithm that was originally designed for the removal of multiplicative noise. Ours is the first implementation of this method within the context of EM tomography.

Chapter 5

Implementation of the Numerical Solution

5.1 Introduction

Digital images are given on discrete (regular) grids. This lends itself for discretizing the PDEs to obtain numerical schemes that can be solved on a computer (see Fig. 5.1). Because of their favorable stability and efficiency properties, semi-implicit schemes have been the methods of choice for the scale discretization [23, 24, 62, 88, 156, 157, 158, 182, 193, 247, 248, 302, 376, 381]. As for the space discretization, the most popular choices are finite difference [62, 376, 381] and finite element methods [23, 24, 88, 182, 302, 376, 381] (in that order of preference). In previous work [32] we chose to discretize the space using finite elements, because of the ability to use adaptive mesh in the numerical solutions (see Figs. 5.2, 5.3, 5.4, and 5.5). In our implementation the remeshing approach based on the L^2-norm was employed, so that the nodes are placed following the edges of the image which allows very good edge preservation. Even though the employment of adaptive grid proved to be a very efficient approach (considerably fewer DOF are necessary to produce similar results to the regular grid case), our decision to work with 3D electron tomograms made us revise our approach in favor of more simple finite difference schemes.

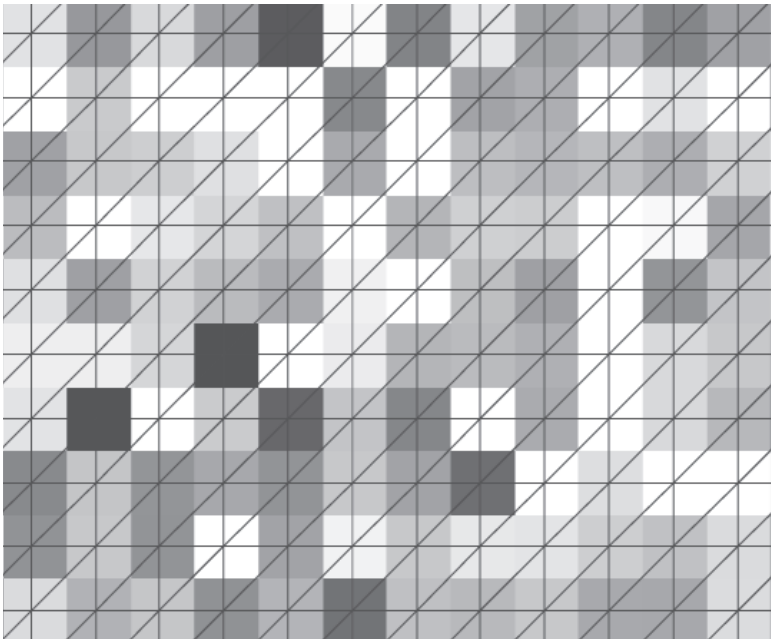

Figure 5.1: Digital images are given on discrete (regular) grids. This lends itself for discretizing the PDEs to obtain numerical schemes that can be solved on a computer. The figure shows a zoomed-in detail of an image at the pixel level that was superimposed with a finite element mesh of triangular elements. Each node of an element has one DOF, the intensity value of that pixel.

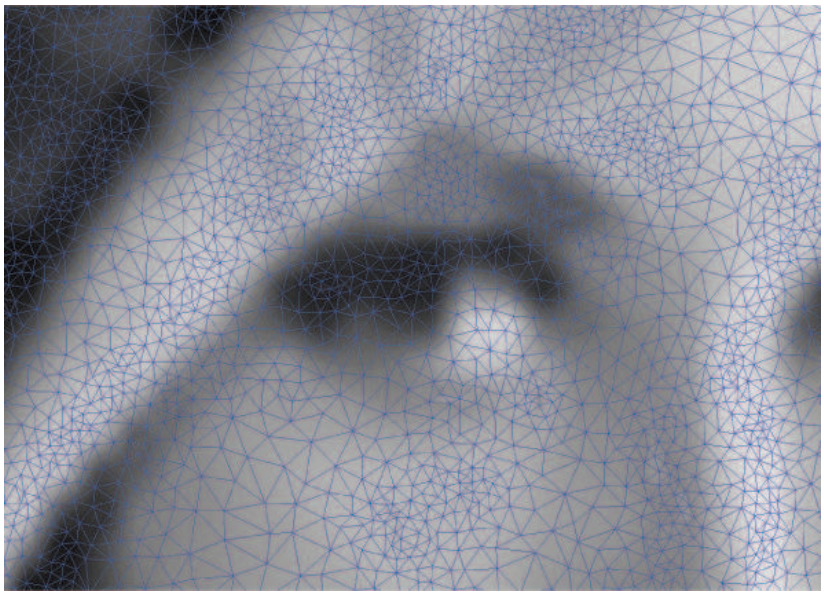

Figure 5.2: Zoomed-in detail of the filtered image of Lena with the final adaptive mesh superimposed.

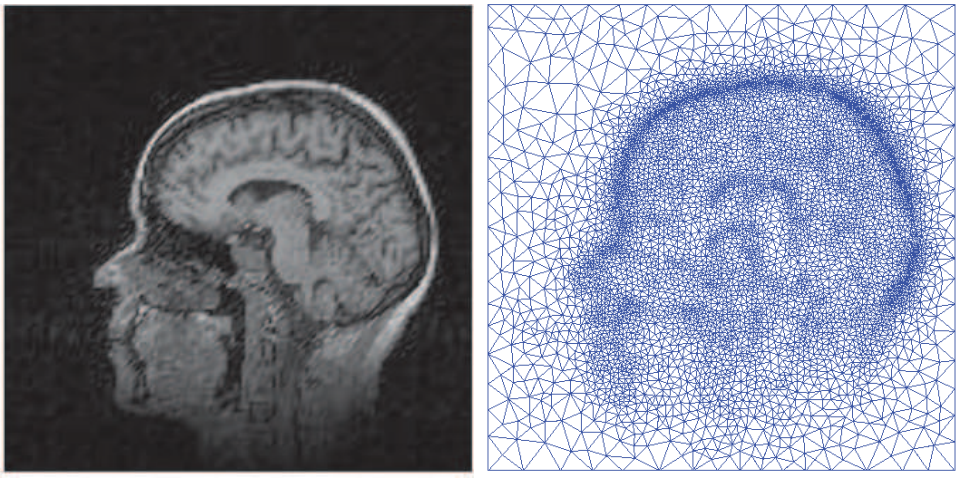

Figure 5.3: (*left to right*) 2D slice of a brain MRI and the final adaptive mesh.

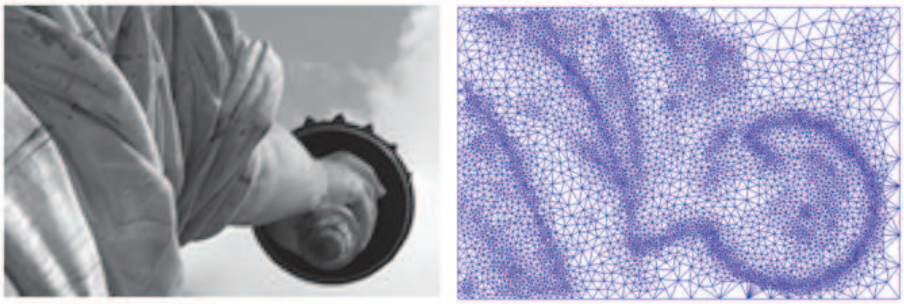

Figure 5.4: (*left to right*) Filtered image of the Statute of Liberty and the final adaptive mesh.

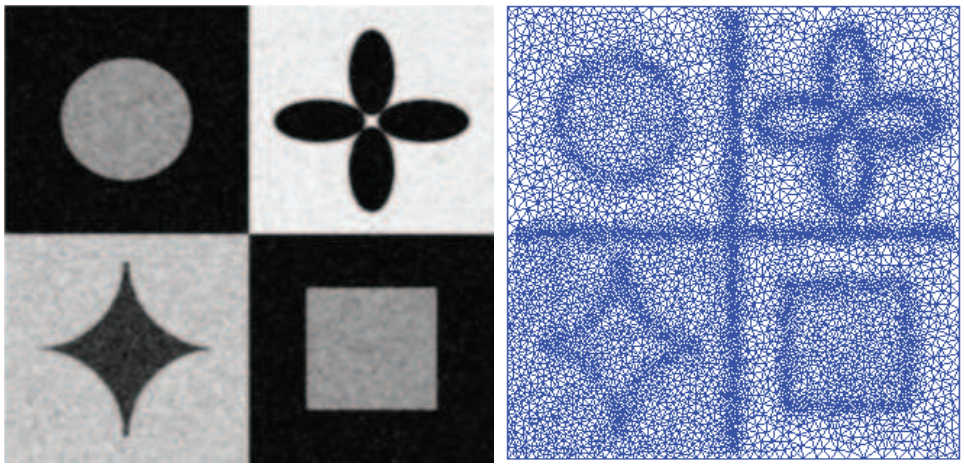

Figure 5.5: (*left to right*) Filtered version of the synthetic geometric image and the final adaptive mesh.

5.2 Algorithms for the Anisotropic Nonlinear Diffusion Models

5.2.1 Perona-Malik Inhomogeneous Nonlinear Diffusion Model

The classic Perona-Malik model, Eq. (3.12), is given by

$$
\begin{aligned}
& u_t - \nabla \cdot \left(g\left(|\nabla u|^2 \right) \cdot \nabla u \right) = 0, \qquad \text{on } \ \Omega \times [\,0, \infty), \\
& u\left(\mathbf{x}, 0\right) = u_0\left(\mathbf{x}\right), \qquad \text{on } \ \Omega, \\
& \langle g \nabla u, \mathbf{n} \rangle = 0, \qquad \text{on } \ \partial\Omega \times (0, \infty), \\
& g\left(|\nabla u|^2 \right) = \frac{1}{1 + |\nabla u|^2 / \lambda^2}, \qquad \lambda = 10^{-2}.
\end{aligned}
$$

The algorithm to implement the Perona-Malik model is as follows:

$N \Leftarrow 50$ % number of iterations

$\lambda \Leftarrow 10^{-2}$ % contrast parameter

$\delta t \Leftarrow 10^{-2}$ % time-step

$u\left(\mathbf{x}, 0\right) \Leftarrow u_0\left(\mathbf{x}\right)$, on Ω % set initial condition

$c_1 \Leftarrow \mathrm{corr}\left(u, f\right)$ % performance measure

$\bar{c}_1 \Leftarrow \mathrm{corr}\left(u, u_0\right)$ % correlation measure

for $i = 1$ to N **do**

$\nabla u \Leftarrow \left[u_x \ \ u_y\right]^{\mathrm{T}}$ % estimate gradients

$|\nabla u| \Leftarrow \sqrt{u_x^2 + u_y^2}$ % magnitude of the gradients

$g \Leftarrow \frac{1}{1 + |\nabla u|^2 / \lambda^2}$ % diffusivity function

$\langle g \cdot \nabla u, \mathbf{n} \rangle \Leftarrow 0$, on $\partial\Omega$ % set boundary conditions

$\phi \Leftarrow \nabla \cdot \left(g \cdot \nabla u\right)$ % diffusion term

$u \Leftarrow u + \delta t \phi$ % evolve the image

$c_{i+1} \Leftarrow \mathrm{corr}\left(u, f\right)$ % update performance measure

$\bar{c}_{i+1} \Leftarrow \mathrm{corr}\left(u, u_0\right)$ % update correlation measure

$\hat{c}_{i+1} \Leftarrow \partial^2 \bar{c}_{i+1}$ % stopping criterion

if $\partial \hat{c}_{i+1} \leq 0$ **then**

$v = u$ % save best image if condition is met

end if

end for

5.2.2 Catté, Lions, Morel and Coll Inhomogeneous Nonlinear Diffusion Model

The Perona-Malik model as modified by Catté, Lions, Morel and Coll, Eq. (3.13), is given by

$$
\begin{aligned}
& u_t - \nabla \cdot \left(g\left(|\nabla u_\sigma|^2 \right) \cdot \nabla u \right) = 0, \qquad \text{on } \Omega \times [\,0, \infty), \\
& u\,(\mathbf{x}, 0) = u_0\,(\mathbf{x}), \qquad \text{on } \Omega, \\
& \langle g \cdot \nabla u, \mathbf{n} \rangle = 0, \qquad \text{on } \partial\Omega \times (0, \infty), \\
& g\left(|\nabla u_\sigma|^2 \right) = \frac{1}{1 + |\nabla u_\sigma|^2 / \lambda^2}, \qquad \lambda = 10^{-2}, \\
& u_\sigma = G_\sigma * u, \qquad \sigma = 1.
\end{aligned}
$$

The algorithm to implement the Perona-Malik model as modified by Catté, Lions, Morel and Coll is as follows:

$N \Leftarrow 50$ % number of iterations

$\lambda \Leftarrow 10^{-2}$ % contrast parameter

$\delta t \Leftarrow 10^{-2}$ % time-step

$\sigma \Leftarrow 1$ % Gaussian kernel's width

$u\,(\mathbf{x}, 0) \Leftarrow u_0\,(\mathbf{x})$, on Ω % set initial condition

$c_1 \Leftarrow \mathrm{corr}\,(u, f)$ % performance measure

$\bar{c}_1 \Leftarrow \mathrm{corr}\,(u, u_0)$ % correlation measure

for $i = 1$ to N **do**

$u_\sigma \Leftarrow G_\sigma * u$ % convolve image with Gaussian kernel

$\nabla u \Leftarrow [u_x \;\; u_y]^{\mathrm{T}}$ % estimate gradients

$\nabla u_\sigma \Leftarrow \left[(u_\sigma)_x \;\; (u_\sigma)_y\right]^{\mathrm{T}}$ % estimate gradients

$|\nabla u_\sigma| \Leftarrow \sqrt{(u_\sigma)_x^2 + (u_\sigma)_y^2}$ % magnitude of the gradients

$g \Leftarrow \frac{1}{1+|\nabla u_\sigma|^2/\lambda^2}$ % diffusivity function

$\langle g \cdot \nabla u, \mathbf{n}\rangle \Leftarrow 0$, on $\partial\Omega$ % set boundary conditions

$\phi \Leftarrow \nabla \cdot (g \cdot \nabla u)$ % diffusion term

$u \Leftarrow u + \delta t \phi$ % evolve the image

$c_{i+1} \Leftarrow \mathrm{corr}\,(u, f)$ % update performance measure

$\bar{c}_{i+1} \Leftarrow \mathrm{corr}\,(u, u_0)$ % update correlation measure

$\hat{c}_{i+1} \Leftarrow \partial^2 \bar{c}_{i+1}$ % stopping criterion

if $\partial \hat{c}_{i+1} \leq 0$ **then**

$v = u$ % save best image if condition is met

end if

end for

5.2.3 Anisotropic Nonlinear Diffusion and Bilateral Filter Model

The proposed model (Perona-Malik model as modified by Bazán and Blomgren), Eq. (3.14), is given by

$$
\begin{aligned}
& u_t - \nabla \cdot \left(g\left(|\nabla u_{bf}|^2\right) \cdot \nabla u\right) = 0, \qquad \text{on } \Omega \times [0, \infty), \\
& u(\mathbf{x}, 0) = u_0(\mathbf{x}), \qquad \text{on } \Omega, \\
& \langle g \cdot \nabla u, \mathbf{n}\rangle = 0, \qquad \text{on } \partial\Omega \times (0, \infty), \\
& g\left(|\nabla u|^2\right) = \frac{1}{1 + |\nabla u_{bf}|^2/\lambda^2}, \qquad \lambda = 10^{-2}, \\
& u_{bf} = G_{bf} * u, \qquad \sigma_d = 3, \qquad \sigma_r = 10^{-2}.
\end{aligned}
$$

The algorithm to implement the proposed model (Perona-Malik model as modified

by Bazán and Blomgren) is as follows:

$N \Leftarrow 50$ % number of iterations

$\lambda \Leftarrow 10^{-2}$ % contrast parameter

$\delta t \Leftarrow 10^{-2}$ % time-step

$\sigma_d \Leftarrow 3$ % domain Gaussian kernel's width

$\sigma_r \Leftarrow 10^{-2}$ % range Gaussian kernel's width

$u(\mathbf{x}, 0) \Leftarrow u_0(\mathbf{x})$, on Ω % set initial condition

$c_1 \Leftarrow \operatorname{corr}(u, f)$ % performance measure

$\bar{c}_1 \Leftarrow \operatorname{corr}(u, u_0)$ % correlation measure

for $i = 1$ to N **do**

$u_{bf} \Leftarrow G_{bf} * u$ % convolve image with bilateral filter kernel

$\nabla u \Leftarrow [u_x \;\; u_y]^{\mathrm{T}}$ % estimate gradients

$\nabla u_{bf} \Leftarrow \left[(u_{bf})_x \;\; (u_{bf})_y \right]^{\mathrm{T}}$ % estimate gradients

$|\nabla u_{bf}| \Leftarrow \sqrt{(u_{bf})_x^2 + (u_{bf})_y^2}$ % magnitude of the gradients

$g \Leftarrow \frac{1}{1+\left|\nabla u_{bf}\right|^2/\lambda^2}$ % diffusivity function

$\langle g \cdot \nabla u, \mathbf{n} \rangle \Leftarrow 0$, on $\partial\Omega$ % set boundary conditions

$\phi \Leftarrow \nabla \cdot (g \cdot \nabla u)$ % diffusion term

$u \Leftarrow u + \delta t \phi$ % evolve the image

$c_{i+1} \Leftarrow \operatorname{corr}(u, f)$ % update performance measure

$\bar{c}_{i+1} \Leftarrow \operatorname{corr}(u, u_0)$ % update correlation measure

$\hat{c}_{i+1} \Leftarrow \partial^2 \bar{c}_{i+1}$ % stopping criterion

if $\partial \hat{c}_{i+1} \leq 0$ **then**

$v = u$ % save best image if condition is met

end if

end for

5.2.4 Structure Enhancing Anisotropic Nonlinear Diffusion Model

The proposed SED model, Eq. (3.37), is given by

$$u_t - \nabla \cdot (\mathbf{D}_{bf} \cdot \nabla u) = 0, \qquad \text{on } \Omega \times [\,0, \infty)\,,$$

$$u\,(\mathbf{x}, 0) = u_0\,(\mathbf{x})\,, \qquad \text{on } \Omega,$$

$$\langle \mathbf{D}_{bf} \cdot \nabla u, \mathbf{n} \rangle = 0 \qquad \text{on } \partial\Omega \times (0, \infty)\,.$$

The algorithm to implement the proposed SED model is as follows:

$\delta t \Leftarrow 1/6$ % time-step

$\sigma_d \Leftarrow 1$ % domain Gaussian kernel's width

$\sigma_r \Leftarrow 10^{-2}$ % range Gaussian kernel's width

$\bar{\sigma}_d \Leftarrow 2$ % orientation Gaussian kernel's width

$\bar{\sigma}_r \Leftarrow 10^{-2}$ % magnitude Gaussian kernel's width

$u\,(\mathbf{x}, 0) \Leftarrow u_0\,(\mathbf{x})$, on Ω % set initial condition

$\bar{c}_1 \Leftarrow \mathrm{corr}\,(u, u_0)$ % correlation measure

repeat

$u_{bf} \Leftarrow G_{bf} * u$ % convolve image with bilateral filter kernel

$\nabla u \Leftarrow \left[u_x \;\; u_y \;\; u_z\right]^{\mathrm{T}}$ % estimate gradients

$\nabla u_{bf} \Leftarrow \left[(u_{bf})_x \;\; (u_{bf})_y \;\; (u_{bf})_z\right]^{\mathrm{T}}$ % estimate gradients

$|\nabla u_{bf}| \Leftarrow \sqrt{(u_{bf})_x^2 + (u_{bf})_y^2 + (u_{bf})_z^2}$ % magnitude of the gradients

$\mathbf{J}_{bf} \Leftarrow \nabla u_{bf} \cdot \nabla u_{bf}^{\mathrm{T}}$ % structure tensor

$\bar{\mathbf{J}}_{bf} \Leftarrow \bar{G}_{bf} * \mathbf{J}_{bf}$ % convolve structure tensor with bilateral filter

$\mathbf{v}_j, \mu_j \Leftarrow \mathbf{eigen}\big(\bar{\mathbf{J}}_{bf}\big),\ j = 1, 2, 3$ % eigenvectors and eigenvalues

$\lambda \Leftarrow \mathbf{prctile}(|\nabla u_{bf}|)$ % contrast parameter

$g \Leftarrow \frac{1}{1+\left|\nabla u_{bf}\right|^2/\lambda^2}$ % diffusivity function

$C_2 \Leftarrow \mathbf{sqtm}(\mu_1, \mu_2)$ % coherence parameter

$C_3 \Leftarrow \mathbf{sqtm}(\mu_1, \mu_3)$ % coherence parameter

$\lambda_1 \Leftarrow g$ % prescribe eigenvalue

$\lambda_2 \Leftarrow g + (1-g)\exp\left(-\frac{C_2}{(\mu_1-\mu_2)^2}\right)$ % prescribe eigenvalue

$\lambda_3 \Leftarrow g + (1-g)\exp\left(-\frac{C_3}{(\mu_1-\mu_3)^2}\right)$ % prescribe eigenvalue

$\mathbf{D}_{bf} \Leftarrow [\mathbf{v}_1 \;\; \mathbf{v}_2 \;\; \mathbf{v}_3]\,\mathrm{diag}\,(\lambda_1, \lambda_2, \lambda_3)\,[\mathbf{v}_1 \;\; \mathbf{v}_2 \;\; \mathbf{v}_3]^{\mathrm{T}}$ % form diffusion tensor

$\langle \mathbf{D}_{bf} \cdot \nabla u, \mathbf{n} \rangle \Leftarrow 0$, on $\partial\Omega$ % set boundary conditions

$\phi = \nabla \cdot (\mathbf{D}_{bf} \cdot \nabla u)$ % diffusion term

$u \Leftarrow u + \delta t \phi$ % evolve the image

$\bar{c}_{i+1} \Leftarrow \mathrm{corr}\,(u, u_0)$ % update correlation measure

$\hat{c}_{i+1} \Leftarrow \partial^2 \bar{c}_{i+1}$ % stopping criterion

until $\partial \hat{c}_{i+1} \leq 0$

5.3 Algorithms for the Total Variation-Based Models

5.3.1 Marquina-Osher Total Variation-Based Model

The classic Marquina-Osher TV-based model used in our experiment, Eq. (4.19), is given by

$$
\begin{aligned}
& u_t - |\nabla u|\,\nabla \cdot \left(\frac{\nabla u}{|\nabla u|}\right) + |\nabla u|\,\lambda\,(u - u_0) = 0, \qquad \text{on } \Omega \times [\,0, \infty)\,, \\
& u\,(\mathbf{x}, 0) = u_0\,(\mathbf{x})\,, \qquad \text{on } \Omega, \\
& \langle g \cdot \nabla u, \mathbf{n} \rangle = 0, \qquad \text{on } \partial\Omega \times (0, \infty)\,.
\end{aligned}
$$

The algorithm to implement the classic Marquina-Osher is as follows:

$N \Leftarrow 2000$ % number of iterations

$\varepsilon \Leftarrow 1/255$ % regularization constant

$\delta t \Leftarrow \varepsilon/5$ % time-step

$\sigma \Leftarrow 1$ % Gaussian kernel's width

$u(\mathbf{x}, 0) \Leftarrow u_0(\mathbf{x})$, on Ω % set initial condition

$\nabla u_0 \Leftarrow \left[(u_0)_x \quad (u_0)_y\right]^{\mathrm{T}}$ % estimate gradients

$u_\sigma = G_\sigma * u$ % convolve image with Gaussian kernel

$\sigma^2 = \mathrm{var}(u) - \mathrm{var}(u_\sigma)$ % estimate variance of the noise

$c_1 \Leftarrow \mathrm{corr}(u, f)$ % performance measure

$\bar{c}_1 \Leftarrow \mathrm{corr}(u, u_0)$ % correlation measure

for $i = 1$ to N **do**

$\nabla u \Leftarrow [u_x \quad u_y]^{\mathrm{T}}$ % estimate gradients

$|\nabla u| \Leftarrow \sqrt{u_x^2 + u_y^2}$ % magnitude of the gradients

$g \Leftarrow \frac{1}{\sqrt{u_x^2 + u_y^2 + \varepsilon}}$ % diffusivity function

$\langle g \cdot \nabla u, \mathbf{n} \rangle \Leftarrow 0$, on $\partial\Omega$ % set boundary conditions

$\lambda = -\frac{1}{2|\Omega|\sigma^2} \int_\Omega \left[|\nabla u| - \frac{\nabla u_0^{\mathrm{T}} \nabla u}{|\nabla u|}\right] d\mathbf{x}$ % forcing term parameter

$\phi = |\nabla u| (\nabla \cdot (g \cdot \nabla u) - \lambda (u - u_0))$ % diffusion term

$u \Leftarrow u + \delta t \phi$ % evolve the image

$c_{i+1} \Leftarrow \mathrm{corr}(u, f)$ % update performance measure

$\bar{c}_{i+1} \Leftarrow \mathrm{corr}(u, u_0)$ % update correlation measure

$\hat{c}_{i+1} \Leftarrow \partial^2 \bar{c}_{i+1}$ % stopping criterion

if $\partial \hat{c}_{i+1} \leq 0$ **then**

$v = u$ % save best image if condition is met

end if

end for

5.3.2 Parameter-Free Adaptive Total Variation-Based Noise Removal and Edge Strengthening Model, Image Processing

The parameter-free adaptive TV-based noise removal and edge strengthening model used in our experiment, Eq. (4.20), is given by

$$
\begin{aligned}
& u_t - |\nabla u| \, \nabla \cdot \left(\frac{\nabla u}{|\nabla u|} \right) + \Lambda \left(u - u_0 \right) = 0, \qquad \text{on } \ \Omega \times [\, 0, \infty) \,, \\
& u \left(\mathbf{x}, 0 \right) = u_0 \left(\mathbf{x} \right), \qquad \text{on } \ \Omega, \\
& \langle g \cdot \nabla u, \mathbf{n} \rangle = 0, \qquad \text{on } \ \partial\Omega \times (0, \infty) \,.
\end{aligned}
$$

The algorithm to implement the parameter-free adaptive TV-based noise removal and edge strengthening model is as follows:

$N \Leftarrow 100$ % number of iterations

$\varepsilon \Leftarrow 1/255$ % regularization parameter

$\sigma \Leftarrow 1$ % Gaussian kernel's width

$d \Leftarrow 2$ % dimensionality of problem

$u \left(\mathbf{x}, 0 \right) \Leftarrow u_0 \left(\mathbf{x} \right)$, on Ω % set initial condition

$\nabla u_0 \Leftarrow \left[\left(u_0 \right)_x \ \ \left(u_0 \right)_y \right]^{\mathrm{T}}$ % estimate gradients

$c_1 \Leftarrow \mathrm{corr} \left(u, f \right)$ % performance measure

$\bar{c}_1 \Leftarrow \mathrm{corr} \left(u, u_0 \right)$ % correlation measure

for $i = 1$ to N **do**

$u_\sigma = G_\sigma * u$ % convolve image with Gaussian kernel

$\sigma^2 = \mathrm{var} \left(u \right) - \mathrm{var} \left(u_\sigma \right)$ % estimate variance of the noise

$\nabla u \Leftarrow \left[u_x \ \ u_y \right]^{\mathrm{T}}$ % estimate gradients

$|\nabla u| \Leftarrow \sqrt{u_x^2 + u_y^2}$ % magnitude of the gradients

$g \Leftarrow \frac{1}{\sqrt{u_x^2 + u_y^2 + \varepsilon}}$ % diffusivity function

$\langle g \cdot \nabla u, \mathbf{n} \rangle \Leftarrow 0$, on $\partial\Omega$ % set boundary conditions

$\Lambda = -\frac{1}{2\sigma^2}\left[u_x\left(u_x - (u_0)_x\right) + u_y\left(u_y - (u_0)_y\right)\right]$ % forcing term parameter

$\phi = |\nabla u|\,\nabla\cdot\left(g\cdot\nabla u\right) - \Lambda\left(u - u_0\right)$ % diffusion term

$\delta t\left(\mathbf{x}\right) = \frac{\varepsilon}{5} + \left(\frac{1}{2d} - \frac{\varepsilon}{5}\right)\left(\frac{\max(|\nabla u|) - |\nabla u|}{\max(|\nabla u|)}\right)$ % time-step

$u \Leftarrow u + \delta t\phi$ % evolve the image

$c_{i+1} \Leftarrow \mathrm{corr}\left(u, f\right)$ % update performance measure

$\bar{c}_{i+1} \Leftarrow \mathrm{corr}\left(u, u_0\right)$ % update correlation measure

$\hat{c}_{i+1} \Leftarrow \partial^2 \bar{c}_{i+1}$ % stopping criterion

if $\partial\hat{c}_{i+1} \leq 0$ **then**

$v = u$ % save best image if condition is met

end if

end for

5.3.3 Parameter-Free Adaptive Total Variation-Based Noise Removal and Edge Strengthening Model, Electron Tomography

The parameter-free adaptive TV-based noise removal and edge strengthening model used in our experiment, Eq. (4.13), is given by

$$u_t - |\nabla u|\,\nabla\cdot\left(\mathbf{D}_{bf}\left(|\nabla u|^{p-1}\right)\cdot\nabla u\right) + \Lambda G_\sigma * \left(G_\sigma * u - u_0\right) = 0,$$

$$\text{on } \Omega\times[0,\infty),$$

$$u\left(\mathbf{x},0\right) = u_0\left(\mathbf{x}\right), \qquad \text{on } \Omega,$$

$$\left\langle \mathbf{D}_{bf}\cdot\nabla u, \mathbf{n}\right\rangle = 0, \qquad \text{on } \partial\Omega\times(0,\infty).$$

The algorithm to implement the parameter-free adaptive TV-based noise removal and edge strengthening model is as follows:

$\varepsilon \Leftarrow 1/255$ % regularization parameter

$\sigma \Leftarrow 1$ % Gaussian kernel's width

$\sigma_d \Leftarrow 1$ % domain Gaussian kernel's width

$\sigma_r \Leftarrow 10^{-2}$ % range Gaussian kernel's width

$\bar{\sigma}_d \Leftarrow 2$ % orientation Gaussian kernel's width

$\bar{\sigma}_r \Leftarrow 10^{-2}$ % magnitude Gaussian kernel's width

$d \Leftarrow 2$ % dimensionality of problem

$u(\mathbf{x}, 0) \Leftarrow u_0(\mathbf{x})$, on Ω % set initial condition

$\nabla u_0 \Leftarrow \left[(u_0)_x \quad (u_0)_y\right]^{\mathrm{T}}$ % estimate gradients

$\bar{c}_1 \Leftarrow \mathrm{corr}(u, u_0)$ % correlation measure

repeat

$u_\sigma = G_\sigma * u$ % convolve image with Gaussian kernel

$\sigma^2 = \mathrm{var}(u) - \mathrm{var}(u_\sigma)$ % estimate variance of the noise

$u_{bf} = G_{bf} * u$ % convolve image with bilateral filter kernel

$\nabla u_{bf} \Leftarrow \left[(u_{bf})_x \quad (u_{bf})_y\right]^{\mathrm{T}}$ % estimate gradients

$\nabla u \Leftarrow [u_x \quad u_y]^{\mathrm{T}}$ % estimate gradients

$|\nabla u| \Leftarrow \sqrt{u_x^2 + u_y^2}$ % magnitude of the gradients

$\mathbf{J}_{bf} = \nabla u_{bf} \cdot \nabla u_{bf}^{\mathrm{T}}$ % structure tensor

$\bar{\mathbf{J}}_{bf} = \bar{G}_{bf} * \mathbf{J}_{bf}$ % convolve structure tensor with bilateral filter

$\mathbf{v}_j, \mu_j \Leftarrow \mathbf{eigen}\left(\bar{\mathbf{J}}_{bf}\right)$, $j = 1, 2, 3$ % eigenvectors and eigenvalues

$\lambda \Leftarrow \mathbf{prctile}(|\nabla u_{bf}|)$ % contrast parameter

$g \Leftarrow \frac{1}{1+\left|\nabla u_{bf}\right|^2 / \lambda^2}$ % diffusivity function

$C \Leftarrow \mathbf{sqtm}(\mu_1, \mu_2)$ % coherence parameter

$p_1 \Leftarrow g$ % mode switch parameter

$p_2 \Leftarrow g + (1-g)\exp\left(-\frac{C}{(\mu_1 - \mu_2)^2}\right)$ % mode switch parameter

$\lambda_1 = |\nabla u|^{p_1 - 1}$ and $\lambda_2 = |\nabla u|^{p_2 - 1}$ % prescribe eigenvectors

$\mathbf{D}_{bf} \Leftarrow [\mathbf{v}_1 \quad \mathbf{v}_2 \quad \mathbf{v}_3]\,\mathrm{diag}(\lambda_1, \lambda_2, \lambda_3)\,[\mathbf{v}_1 \quad \mathbf{v}_2 \quad \mathbf{v}_3]^{\mathrm{T}}$ % form diffusion tensor

$\langle \mathbf{D}_{bf} \cdot \nabla u, \mathbf{n} \rangle \Leftarrow 0$, on $\partial\Omega$ % set boundary conditions

$\Lambda \Leftarrow -\frac{1}{2\sigma^2}\left[u_x\left(u_x - (u_0)_x\right) + u_y\left(u_y - (u_0)_y\right)\right]$ % forcing term parameter

$\phi \Leftarrow |\nabla u|\,\nabla \cdot (\mathbf{D}_{bf} \cdot \nabla u) - \Lambda G_\sigma * (G_\sigma * u - u_0)$ % diffusion term

$\delta t\,(\mathbf{x}) = \frac{\varepsilon}{5} + \left(\frac{1}{2d} - \frac{\varepsilon}{5}\right)\left(\frac{\max(|\nabla u|) - |\nabla u|}{\max(|\nabla u|)}\right)$ % time-step

$u \Leftarrow u + \delta t \phi$ % evolve the image

$\bar{c}_{i+1} \Leftarrow \mathrm{corr}\,(u, u_0)$ % update correlation measure

$\hat{c}_{i+1} \Leftarrow \partial^2 \bar{c}_{i+1}$ % stopping criterion

until $\partial \hat{c}_{i+1} \leq 0$

5.3.4 Homomorphic Total Variation-Based Model

The homomorphic TV-based model used in our experiment is given by

$$u_t - |\nabla u|\,\nabla \cdot \left(\frac{\nabla u}{|\nabla u|}\right) + \Lambda G_\sigma * (G_\sigma * u - u_0) = 0, \qquad \text{on } \Omega \times [\,0, \infty)\,,$$
$$u\,(\mathbf{x}, 0) = u_0\,(\mathbf{x})\,, \qquad \text{on } \Omega,$$
$$\langle g \cdot \nabla u, \mathbf{n} \rangle = 0, \qquad \text{on } \partial\Omega \times (0, \infty)\,.$$

The algorithm to implement the homomorphic TV-based model is as follows:

$\varepsilon \Leftarrow 1/255$ % regularization parameter

$\sigma \Leftarrow 1$ % Gaussian kernel's width

$d \Leftarrow 2$ % dimensionality of problem

$L = 61$ % number of looks

$\gamma_{EM} = 0.577215664901$ % Euler-Mascheroni constant

$\mu_{\bar{m}} = -\gamma_{EM} - \ln(L) + \sum_{k=1}^{L-1} \frac{1}{k}$ % noise mean

$\sigma^2_{\bar{m}} = \frac{\pi^2}{6} - \sum_{k=1}^{L-1} \frac{1}{k^2}$ % noise variance

$u_0 = \ln(u_0 + 1) + \mu_{\bar{m}}$ % logarithmic transform

$u\,(\mathbf{x}, 0) \Leftarrow u_0\,(\mathbf{x})$, on Ω % set initial condition

$\nabla u_0 \Leftarrow \left[(u_0)_x \quad (u_0)_y\right]^{\mathrm{T}}$ % estimate gradients

$\bar{c}_1 \Leftarrow \text{corr}\,(u, u_0)$ % correlation measure

repeat

$\nabla u \Leftarrow [u_x \;\; u_y]^{\mathrm{T}}$ % estimate gradients

$|\nabla u| \Leftarrow \sqrt{u_x^2 + u_y^2}$ % magnitude of the gradients

$g \Leftarrow \frac{1}{\sqrt{u_x^2+u_y^2+\varepsilon}}$ % diffusivity function

$\langle g \cdot \nabla u, \mathbf{n} \rangle \Leftarrow 0$, on $\partial\Omega$ % set boundary conditions

$\Lambda = -\frac{1}{2\sigma_{\bar{m}}^2}\left[u_x\left(u_x - (u_0)_x\right) + u_y\left(u_y - (u_0)_y\right)\right]$ % forcing term parameter

$\phi = |\nabla u|\,\nabla \cdot (g \cdot \nabla u) - \Lambda G_\sigma * (G_\sigma * u - u_0)$ % diffusion term

$\delta t\,(\mathbf{x}) = \frac{\varepsilon}{5} + \left(\frac{1}{2d} - \frac{\varepsilon}{5}\right)\left(\frac{\max(|\nabla u|) - |\nabla u|}{\max(|\nabla u|)}\right)$ % time-step

$u \Leftarrow u + \delta t \phi$ % evolve the image

$\bar{c}_{i+1} \Leftarrow \text{corr}\,(u, u_0)$ % update correlation measure

$\hat{c}_{i+1} \Leftarrow \partial^2 \bar{c}_{i+1}$ % stopping criterion

until $\partial \hat{c}_{i+1} \leq 0$

$u = \exp(u - \mu_{\bar{m}}) - 1;$ % exponential transform

5.3.5 Rudin-Lions-Osher Total Variation-Based Model

The Rudin-Lions-Osher TV-based model used in our experiment is given by

$$
\begin{aligned}
& u_t - \nabla \cdot \left(\frac{\nabla u}{|\nabla u|}\right) + \lambda_1 \frac{u_0^2}{u^3} + \lambda_2 \frac{u_0}{u^2} = 0, \qquad \text{on } \Omega \times [\,0, \infty)\,, \\
& u\,(\mathbf{x}, 0) = u_0\,(\mathbf{x})\,, \qquad \text{on } \Omega, \\
& \langle g \cdot \nabla u, \mathbf{n} \rangle = 0, \qquad \text{on } \partial\Omega \times (0, \infty)\,.
\end{aligned}
$$

The algorithm to implement the Rudin-Lions-Osher TV-based model is as follows:

$\varepsilon \Leftarrow 1/255$ % regularization parameter

$\sigma \Leftarrow 1$ % Gaussian kernel's width

$\delta t \Leftarrow \varepsilon/5$ % time-step

$u(\mathbf{x},0) \Leftarrow u_0(\mathbf{x})$, on Ω % set initial condition

$\nabla u_0 \Leftarrow \left[(u_0)_x \quad (u_0)_y\right]^{\mathrm{T}}$ % estimate gradients

$\bar{c}_1 \Leftarrow \mathrm{corr}(u, u_0)$ % correlation measure

repeat

$\nabla u \Leftarrow [u_x \;\; u_y]^{\mathrm{T}}$ % estimate gradients

$|\nabla u| \Leftarrow \sqrt{u_x^2 + u_y^2}$ % magnitude of the gradients

$g \Leftarrow \frac{1}{\sqrt{u_x^2+u_y^2+\varepsilon}}$ % diffusivity function

$\langle g \cdot \nabla u, \mathbf{n}\rangle \Leftarrow 0$, on $\partial\Omega$ % set boundary conditions

$D = \int_\Omega \frac{u_0^4}{u^6} d\mathbf{x} \int_\Omega \frac{u_0^2}{u^4} d\mathbf{x} - \int_\Omega \frac{u_0^3}{u^5} d\mathbf{x} \int_\Omega \frac{u_0^3}{u^5} d\mathbf{x}$ % parameter in Lagrange multiplier

$B = \nabla \cdot (g \cdot \nabla u)$ % parameter in Lagrange multiplier

$\lambda_1(t) = \frac{1}{D}\left(\int_\Omega \frac{u_0^2}{u^4} d\mathbf{x} \int_\Omega \frac{u_0^2}{u^3} B d\mathbf{x} - \int_\Omega \frac{u_0^3}{u^5} d\mathbf{x} \int_\Omega \frac{u_0}{u^2} B d\mathbf{x}\right)$ % Lagrange multiplier

$\lambda_2(t) = \frac{1}{D)}\left(\int_\Omega \frac{u_0^4}{u^6} d\mathbf{x} \int_\Omega \frac{u_0}{u^2} B d\mathbf{x} - \int_\Omega \frac{u_0^3}{u^5} d\mathbf{x} \int_\Omega \frac{u_0^2}{u^3} B d\mathbf{x}\right)$ % Lagrange multiplier

$\phi = B + \lambda_1 \frac{u_0^2}{u^3} + \lambda_2 \frac{u_0}{u^2}$ % diffusion term

$u \Leftarrow u + \delta t \phi$ % evolve the image

$\bar{c}_{i+1} \Leftarrow \mathrm{corr}(u, u_0)$ % update correlation measure

$\hat{c}_{i+1} \Leftarrow \partial^2 \bar{c}_{i+1}$ % stopping criterion

until $\partial \hat{c}_{i+1} \leq 0$

5.4 Concluding Remarks

The processing of 3D images from electron tomogram is computationally very expensive. To cope with the high cost we implemented simple algorithms that can be easily run in parallel. Most of the parallel implementations of these simple numerical schemes were done using the new Parallel Computing Toolbox™ from MATLAB®. The tool proved to be adequate for performing this type of computation.

Appendix A

Mitochondria Disorders

Mitochondria disorders may manifest at any age [206, 207]. Nevertheless, nuclear DNA abnormalities are more common in childhood, while mtDNA abnormalities usually appear in late childhood or adult life. Some mitochondria disorders only affect a single organ, but most of them involve multiple organ systems and patients exhibit a cluster of clinical features that fall into a discrete clinical syndrome [90, 258]. Table A.1 shows some of the clinical syndromes of mitochondria disorders[1].

Table A.1: Clinical Syndromes of Mitochondria Disorders

Disorder	Primary Features	Additional Features
Chronic progressive external ophthalmoplegia (CPEO)	– External ophthalmoplegia – Bilateral ptosis	– Mild proximal myopathy
Kearns-Sayre syndrome (KSS)	– PEO onset before age 20 years – Pigmentary retinopathy – One of the following: CSF protein greater than 1g/L, cerebellar ataxia, heart block	– Bilateral deafness – Myopathy – Dysphagia – Diabetes mellitus – Hypoparathyroidism – Dementia
Pearson syndrome	– Sideroblastic anemia of childhood – Pancytopenia – Exocrine pancreatic failure	– Renal tubular defects

(table continues)

[1]GeneTests: Medical Genetics Information Resource (database online). Copyright, University of Washington, Seattle. 1993-2008. Available at http://www.genetests.org. Accessed 20080429.

Table A.1 (continued)

Disorder	Primary Features	Additional Features
Infantile myopathy and lactic acidosis (fatal and non-fatal forms)	– Hypotonia in the first year of life – Feeding and respiratory difficulties	– Fatal form may be associated with a cardiomyopathy and/or the Toni-Fanconi-Debre syndrome
Leigh syndrome (LS)	– Subacute relapsing encephalopathy – Cerebellar and brain-stem signs – Infantile onset	– Basal ganglia lucencies – Maternal history of neurologic disease or Leigh syndrome
Neurogenic weakness with ataxia and retinitis pigmentosa (NARP)	– Late-childhood or adult-onset peripheral neuropathy – Ataxia – Pigmentary retinopathy	– Basal ganglia lucencies – Abnormal electroretinogram – Sensorimotor neuropathy
mitochondria encephalomyopathy with lactic acidosis and stroke-like episodes (MELAS)	– Stroke-like episodes before age 40 years – Seizures and/or dementia – Ragged-red fibers and/or lactic acidosis	– Diabetes mellitus – Cardiomyopathy (initially hypertrophic; later dilated) – Bilateral deafness – Pigmentary retinopathy – Cerebellar ataxia
Myoclonic epilepsy with ragged-red fibers (MERRF)	– Myoclonus – Seizures – Cerebellar ataxia – Myopathy	– Dementia – Optic atrophy – Bilateral deafness – Peripheral neuropathy – Spasticity – Multiple lipomata
Leber hereditary optic neuropathy (LHON)	– Subacute painless bilateral visual failure – Males:females $\sim 4:1$ – Median age of onset 24 years	– Dystonia – Cardiac pre-excitation syndromes

Appendix B

Gaussian Convolution as a Solution to the Heat Equation

This derivation first appeared in [57]. Given the original noise-free image f, and a blurred version of this image that has been convolved with a kernel, $u_0 = G * f$. It is a well known fact that the difference between the blurred image and the noise-free image is roughly proportional to the Laplacian of image f. To be more concrete, we assume that the kernel G is spatially varying and that we can scale G such that

$$G_\sigma(\mathbf{x}) = \frac{1}{\sigma} G\left(\frac{\mathbf{x}}{\sigma^{\frac{1}{d}}}\right), \tag{B.1}$$

where $\sigma \to 0$ is a scale parameter and d is the number of dimensionality of the data ($d = 2$ for a 2D image). Furthermore, we make the following assumptions: (i) $\mathbf{x}(x, y)$ is a point in the image domain, (ii) image f is at least C^3 around the point $\mathbf{x}$, (iii) G_σ is a positive radial kernel that satisfies $\int \left(1 + |\mathbf{x}|^2 + |\mathbf{x}|^3\right) G_\sigma(\mathbf{x}) d\mathbf{x} < \infty$ and $\int x^2 G_\sigma(\mathbf{x}) d\mathbf{x} = 2$. Expanding f in Taylor series around $\mathbf{x}$ it has been shown in [153] that as $\sigma \to 0$

$$\frac{G_\sigma * f(\mathbf{x}) - f(\mathbf{x})}{\sigma} \to \nabla^2 f(\mathbf{x}). \tag{B.2}$$

We can rewrite Eq. (B.2) and have

$$G_\sigma * f(\mathbf{x}) - f(\mathbf{x}) = \sigma \nabla^2 f(\mathbf{x}) + O(\sigma). \tag{B.3}$$

If $u(\mathbf{x}, t)$ is a solution to the heat equation, then we can write

$$u_t = \nabla^2 u, \qquad u(\mathbf{x}, 0) = f(\mathbf{x}). \tag{B.4}$$

Now, provided that f is at least C^2 and bounded, we can deduce that

$$u(\mathbf{x}, t) - u(\mathbf{x}, 0) = t \nabla^2 f(\mathbf{x}) + O(\sigma). \tag{B.5}$$

Comparing Eq. (B.3) and Eq. (B.4) shows that convolving the image f with a (Gaussian) kernel G_σ is, for small σ, equivalent to applying the heat equation to f at scale σ.

Appendix C

Rudin-Osher-Fatemi Total Variation-Based Model

The TV-based constrained optimization approach involves the variation (oscillations) of the image within its domain, subject to constraints related to the statistics of the noise. The procedure leads to a nonlinear partial differential equation on a manifold determined by the constraints which is solved by a time-evolution scheme. In the Rudin-Osher-Fatemi model [314], given a noisy image $u_0 = f + \eta$, where the true image f has been perturbed by additive white noise η, the restored image $u \approx f$ is the solution of

$$\min_{u \in BV(\Omega)} \mathrm{TV}\,(u) = \min_{u \in BV(\Omega)} \int_\Omega |\nabla u|\, d\mathbf{x},$$

subject to the following constraints involving the noise:

$$\frac{1}{2}\int_\Omega (u - u_0)^2\, d\mathbf{x} = \frac{1}{2}\,|\Omega|\,\sigma^2,$$

$$\frac{1}{|\Omega|}\int_\Omega u_0 d\mathbf{x} = \frac{1}{|\Omega|}\int_\Omega u d\mathbf{x}.$$

We apply Lagrange multipliers to minimize the constrained problem

$$\min_u \int_\Omega |\nabla u|\, d\mathbf{x} - \lambda_1 \int_\Omega (u - u_0)\, d\mathbf{x} - \lambda_2 \left[\frac{1}{2}\int_\Omega (u - u_0)^2\, d\mathbf{x} - |\Omega|\,\sigma^2\right],$$

where λ_1 and λ_2 are the Lagrange multipliers. We take the derivative with respect to u, and set the result equal to zero:

$$\frac{\partial}{\partial u}\left\{\int_\Omega |\nabla u|\, d\mathbf{x} - \lambda_1 \int_\Omega (u-u_0)\, d\mathbf{x} - \lambda_2 \left[\frac{1}{2}\int_\Omega (u-u_0)^2\, d\mathbf{x} - |\Omega|\,\sigma^2\right]\right\} = 0. \quad \text{(C.1)}$$

From the first term in the curly brackets, Eq. (C.1), we have

$$\begin{aligned}
&\frac{\partial |\nabla u|}{\partial u} = \frac{\partial |\nabla u|}{2\partial u} + \frac{\partial |\nabla u|}{2\partial u} = \frac{\partial/\partial x}{\partial/\partial x}\frac{\partial |\nabla u|}{2\partial u} + \frac{\partial/\partial y}{\partial/\partial y}\frac{\partial |\nabla u|}{2\partial u} = \\
&\frac{\partial}{\partial x}\frac{\partial |\nabla u|}{2\partial (\partial u/\partial x)} + \frac{\partial}{\partial y}\frac{\partial |\nabla u|}{2\partial (\partial u/\partial y)} = \frac{\partial}{\partial x}\frac{\partial |\nabla u|}{2\partial u_x} + \frac{\partial}{\partial y}\frac{\partial |\nabla u|}{2\partial u_y} = \\
&\frac{\partial}{\partial x}\frac{\partial \sqrt{u_x^2+u_y^2}}{2\partial u_x} + \frac{\partial}{\partial y}\frac{\partial \sqrt{u_x^2+u_y^2}}{2\partial u_y} = \frac{\partial}{\partial x}\frac{2u_x}{2\sqrt{u_x^2+u_y^2}} + \frac{\partial}{\partial y}\frac{2u_y}{2\sqrt{u_x^2+u_y^2}} = \\
&\frac{\partial}{\partial x}\frac{u_x}{|\nabla u|} + \frac{\partial}{\partial y}\frac{u_y}{|\nabla u|} = \begin{bmatrix} \frac{\partial}{\partial x} & \frac{\partial}{\partial y} \end{bmatrix} \left(\frac{1}{|\nabla u|} \begin{bmatrix} u_x \\ u_y \end{bmatrix} \right) = \nabla \cdot \left(\frac{\nabla u}{|\nabla u|} \right).
\end{aligned} \quad \text{(C.2)}$$

From the second term in the curly brackets, Eq. (C.1), we have

$$\frac{\partial}{\partial u}(u-u_0) = 1. \quad \text{(C.3)}$$

From the third term in the curly brackets, Eq. (C.1), we have

$$\frac{\partial}{\partial u}(u-u_0)^2 = 2(u-u_0). \quad \text{(C.4)}$$

Replacing Eqs. (C.2), (C.3), and (C.4) into Eq. (C.1),

$$\begin{aligned}\frac{\partial}{\partial u}\left\{\int_{\Omega}|\nabla u|\,d\mathbf{x}-\lambda_1\int_{\Omega}(u-u_0)\,d\mathbf{x}-\lambda_2\left[\frac{1}{2}\int_{\Omega}(u-u_0)^2\,d\mathbf{x}-|\Omega|\,\sigma^2\right]\right\}=0\\ \int_{\Omega}\nabla\cdot\left(\frac{\nabla u}{|\nabla u|}\right)d\mathbf{x}-\lambda_1\int_{\Omega}(1)\,d\mathbf{x}-\lambda_2\left[\frac{1}{2}\int_{\Omega}2\,(u-u_0)\,d\mathbf{x}-0\right]=0.\end{aligned} \tag{C.5}$$

Since Eq. (C.5) has to hold $\forall\,\Omega$ then

$$\nabla\cdot\left(\frac{\nabla u}{|\nabla u|}\right)-\lambda_1-\lambda_2\,(u-u_0)=0,\qquad \text{in }\Omega \tag{C.6}$$

If we set homogeneous Neumann boundary condition, *i.e.*, we do not allow flux in or out of the system, the constraint regarding the mean intensity being constant is automatically satisfied. Thus, there is no need to carry the Lagrange multiplier λ_1, and Eq. (C.6) becomes

$$\begin{aligned}-\nabla\cdot\left(\frac{\nabla u}{|\nabla u|}\right)+\lambda\,(u-u_0)=0,\qquad &\text{in }\Omega\\ \langle g\cdot\nabla u,\mathbf{n}\rangle=0,\qquad &\text{on }\partial\Omega.\end{aligned}$$

Appendix D

Approximation of the Variance of the Noise

In subsection 4.2.1 we proposed to approximate the unknown variance of the additive noise by the following expression:

$$\mathrm{var}\,(\eta) = \mathrm{var}\,(u_0) - \mathrm{var}\,(G_\sigma * u_0)\,, \tag{D.1}$$

where the variance of the (unknown) true image is approximated by the variance of the convolved noisy image with a Gaussian kernel, G_σ, of width $\sigma = 1$. This rationale is based on the assumption that the true image has been perturbed by additive white noise, $u_0 = f + \eta$, and that the noise is independent from the signal. In this case, the variance of the noisy image has to be equal to the sum of the variance of the true image and the variance of the noise, *i.e.*, $\mathrm{var}\,(u_0) = \mathrm{var}\,(f) + \mathrm{var}\,(\eta)$.

The experiment consisted in perturbing the true image with Gaussian white noise of increasing variance, $0 \leqslant \sigma \leqslant 64$, and approximating the variance of the noise by Eq. (D.1). We observe in the figures below that the approximation is very reasonable, specially if we consider that noise of high variance, *e.g.*, $\sigma \geq 64$, is somewhat rare since in those cases the SNR is extremely low, to the point where there is not much signal left after the quantization.

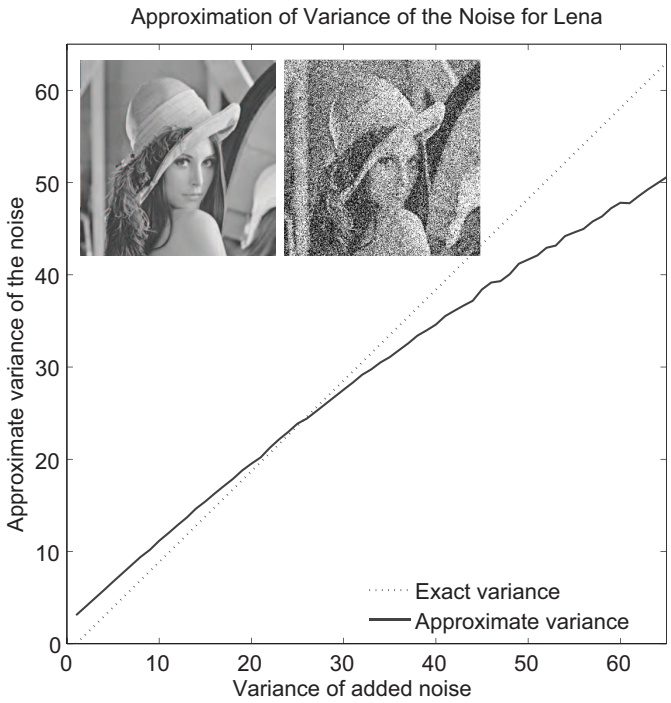

Figure D.1: Approximation of the variance of the noise for Lena.

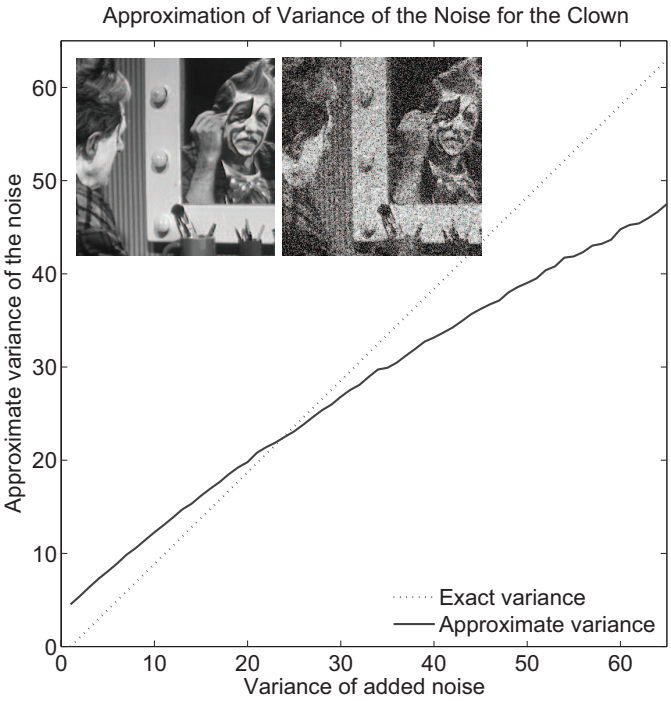

Figure D.2: Approximation of the variance of the noise for the Clown.

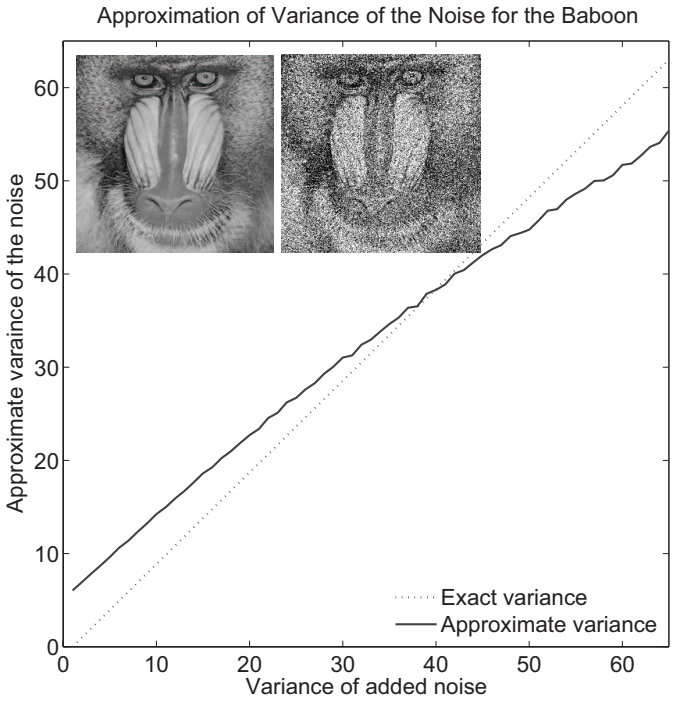

Figure D.3: Approximation of the variance of the noise for the Baboon.

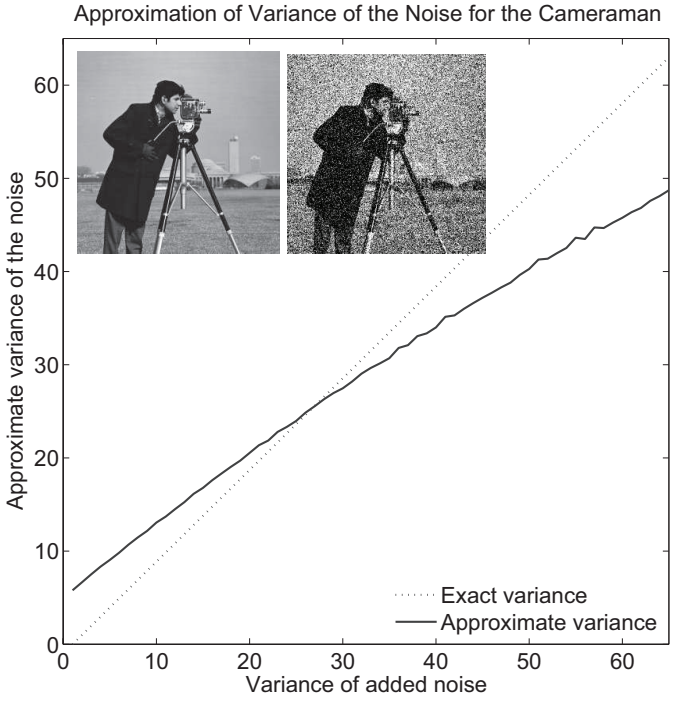

Figure D.4: Approximation of the variance of the noise for the Cameraman.

Appendix E

Lagrange Multipliers

We can obtain the two unknown Lagrange multipliers, λ_1 and λ_2, needed in subsection 4.3.2, from the following equations:

$$u_t = \nabla \cdot \left(\frac{\nabla u}{|\nabla u|} \right) - \lambda_1 \frac{u_0^2}{u^3} - \lambda_2 \frac{u_0}{u^2}, \tag{E.1}$$

$$\frac{\partial}{\partial t} \int_\Omega \left(\frac{u_0}{u} \right) d\mathbf{x} = - \int_\Omega \left(\frac{u_0}{u^2} \, u_t \right) d\mathbf{x} = 0, \tag{E.2}$$

$$\frac{\partial}{\partial t} \int_\Omega \left(\left(\frac{u_0}{u} \right)^2 - 1 \right) d\mathbf{x} = - \int_\Omega \left(\frac{u_0^2}{u^3} \, u_t \right) d\mathbf{x} = 0. \tag{E.3}$$

Multiply Eq. (E.1) by $-\frac{u_0^2}{u^3}$

$$-\frac{u_0^2}{u^3} \, u_t = -\frac{u_0^2}{u^3} \nabla \cdot \left(\frac{\nabla u}{|\nabla u|} \right) + \frac{u_0^2}{u^3} \lambda_1 \frac{u_0^2}{u^3} + \frac{u_0^2}{u^3} \lambda_2 \frac{u_0}{u^2},$$

$$-\frac{u_0^2}{u^3} u_t = -\frac{u_0^2}{u^3} \nabla \cdot \left(\frac{\nabla u}{|\nabla u|} \right) + \lambda_1 \frac{u_0^4}{u^6} + \lambda_2 \frac{u_0^3}{u^5}.$$

Integrate over Ω (for notation simplicity we drop the $d\mathbf{x}$ from the integral over the

image domain Ω)

$$-\int_\Omega \frac{u_0^2}{u^3}u_t = -\int_\Omega \frac{u_0^2}{u^3}\nabla\cdot\left(\frac{\nabla u}{|\nabla u|}\right) + \int_\Omega \lambda_1\frac{u_0^4}{u^6} + \int_\Omega \lambda_2\frac{u_0^3}{u^5}.$$

By Eq. (E.3)

$$-\int_\Omega \frac{u_0^2}{u^3}u_t = -\int_\Omega \frac{u_0^2}{u^3}\nabla\cdot\left(\frac{\nabla u}{|\nabla u|}\right) + \int_\Omega \lambda_1\frac{u_0^4}{u^6} + \int_\Omega \lambda_2\frac{u_0^3}{u^5} = 0,$$

$$-\int_\Omega \frac{u_0^2}{u^3}\nabla\cdot\left(\frac{\nabla u}{|\nabla u|}\right) + \int_\Omega \lambda_1\frac{u_0^4}{u^6} + \int_\Omega \lambda_2\frac{u_0^3}{u^5} = 0,$$

$$\int_\Omega \lambda_1\frac{u_0^4}{u^6} + \int_\Omega \lambda_2\frac{u_0^3}{u^5} = \int_\Omega \frac{u_0^2}{u^3}\nabla\cdot\left(\frac{\nabla u}{|\nabla u|}\right).$$

Consider λ_1 and λ_2 constant for each t

$$\lambda_1\int_\Omega \frac{u_0^4}{u^6} + \lambda_2\int_\Omega \frac{u_0^3}{u^5} = \int_\Omega \frac{u_0^2}{u^3}\nabla\cdot\left(\frac{\nabla u}{|\nabla u|}\right). \tag{E.4}$$

Multiply Eq. (E.1) by $-\frac{u_0}{u^2}$

$$-\frac{u_0}{u^2}u_t = -\frac{u_0}{u^2}\nabla\cdot\left(\frac{\nabla u}{|\nabla u|}\right) + \frac{u_0}{u^2}\lambda_1\frac{u_0^2}{u^3} + \frac{u_0}{u^2}\lambda_2\frac{u_0}{u^2},$$

$$-\frac{u_0}{u^2}u_t = -\frac{u_0}{u^2}\nabla\cdot\left(\frac{\nabla u}{|\nabla u|}\right) + \lambda_1\frac{u_0^3}{u^5} + \lambda_2\frac{u_0^2}{u^4}.$$

Integrate over Ω (for notation simplicity we drop the $d\mathbf{x}$ from the integral over the image domain Ω)

$$-\int_\Omega \frac{u_0}{u^2}u_t = -\int_\Omega \frac{u_0}{u^2}\nabla\cdot\left(\frac{\nabla u}{|\nabla u|}\right) + \int_\Omega \lambda_1\frac{u_0^3}{u^5} + \int_\Omega \lambda_2\frac{u_0^2}{u^4}. \tag{E.5}$$

By Eq. (E.2)

$$-\int_\Omega \frac{u_0}{u^2}u_t = -\int_\Omega \frac{u_0}{u^2}\nabla\cdot\left(\frac{\nabla u}{|\nabla u|}\right)+\int_\Omega \lambda_1\frac{u_0^3}{u^5}+\int_\Omega \lambda_2\frac{u_0^2}{u^4}=0,$$

$$-\int_\Omega \frac{u_0}{u^2}\nabla\cdot\left(\frac{\nabla u}{|\nabla u|}\right)+\int_\Omega \lambda_1\frac{u_0^3}{u^5}+\int_\Omega \lambda_2\frac{u_0^2}{u^4}=0,$$

$$\int_\Omega \lambda_1\frac{u_0^3}{u^5}+\int_\Omega \lambda_2\frac{u_0^2}{u^4}=\int_\Omega \frac{u_0}{u^2}\nabla\cdot\left(\frac{\nabla u}{|\nabla u|}\right).$$

Consider λ_1 and λ_2 constant for each t

$$\lambda_1\int_\Omega \frac{u_0^3}{u^5}+\lambda_2\int_\Omega \frac{u_0^2}{u^4}=\int_\Omega \frac{u_0}{u^2}\nabla\cdot\left(\frac{\nabla u}{|\nabla u|}\right). \tag{E.6}$$

Putting Eqs. (E.4) and (E.6) in matrix-vector form

$$\begin{bmatrix} \int_\Omega \frac{u_0^4}{u^6} & \int_\Omega \frac{u_0^3}{u^5} \\ \int_\Omega \frac{u_0^3}{u^5} & \int_\Omega \frac{u_0^2}{u^4} \end{bmatrix}\begin{bmatrix} \lambda_1 \\ \lambda_2 \end{bmatrix}=\begin{bmatrix} \int_\Omega \frac{u_0^2}{u^3}\nabla\cdot\left(\frac{\nabla u}{|\nabla u|}\right) \\ \int_\Omega \frac{u_0}{u^2}\nabla\cdot\left(\frac{\nabla u}{|\nabla u|}\right) \end{bmatrix}.$$

Define

$$D=\int_\Omega \frac{u_0^4}{u^6}\int_\Omega \frac{u_0^2}{u^4}-\int_\Omega \frac{u_0^3}{u^5}\int_\Omega \frac{u_0^3}{u^5},$$

$$\begin{bmatrix} \lambda_1 \\ \lambda_2 \end{bmatrix}=\frac{1}{D}\begin{bmatrix} \int_\Omega \frac{u_0^2}{u^4} & -\int_\Omega \frac{u_0^3}{u^5} \\ -\int_\Omega \frac{u_0^3}{u^5} & \int_\Omega \frac{u_0^6}{u^4} \end{bmatrix}\begin{bmatrix} \int_\Omega \frac{u_0^2}{u^3}\nabla\cdot\left(\frac{\nabla u}{|\nabla u|}\right) \\ \int_\Omega \frac{u_0}{u^2}\nabla\cdot\left(\frac{\nabla u}{|\nabla u|}\right) \end{bmatrix}.$$

Define

$$B=\nabla\cdot\left(\frac{\nabla u}{|\nabla u|}\right).$$

Then, recalling that $D = D(\mathbf{x})$ and $B = B(\mathbf{x})$

$$\begin{bmatrix} \lambda_1 \\ \lambda_2 \end{bmatrix} = \frac{1}{D} \begin{bmatrix} \int_\Omega \frac{u_0^2}{u^4} & -\int_\Omega \frac{u_0^3}{u^5} \\ -\int_\Omega \frac{u_0^3}{u^5} & \int_\Omega \frac{u_0^6}{u^4} \end{bmatrix} \begin{bmatrix} \int_\Omega \frac{u_0^2}{u^3} B \\ \int_\Omega \frac{u_0}{u^2} B \end{bmatrix},$$

$$\lambda_1 = \frac{1}{D} \left(\int_\Omega \frac{u_0^2}{u^4} \int_\Omega \frac{u_0^2}{u^3} B - \int_\Omega \frac{u_0^3}{u^5} \int_\Omega \frac{u_0}{u^2} B \right), \tag{E.7}$$

$$\lambda_2 = \frac{1}{D} \left(\int_\Omega \frac{u_0^6}{u^4} \int_\Omega \frac{u_0}{u^2} B - \int_\Omega \frac{u_0^3}{u^5} \int_\Omega \frac{u_0^2}{u^3} B \right). \tag{E.8}$$

Bibliography

[1] K.Z. Abd-Elmoniem, A.B.M. Youssef, and Y.M. Kadah. Real-time speckle reduction and coherence enhancement in ultrasound imaging via nonlinear anisotropic diffusion. *IEEE Transactions on Biomedical Engineering*, 49(9):997–1014, 2002.

[2] R. Acar and C.R. Vogel. Analysis of total variation penalty methods for ill-posed problems. *Inverse Problems*, 10(6):1217–1229, 1994.

[3] A. Achim, A. Bezerianos, and P. Tsakalides. An alpha-stable based Bayesian algorithm for speckle noise removal in the wavelet domain. In *IEEE - EURASIP Workshop on Nonlinear Signal and Image Processing*, 2001.

[4] A. Achim, P. Tsakalides, and A. Bezerianos. SAR image denoising via bayesian wavelet shrinkage based on heavy-tailed modeling. *IEEE Transactions on Geoscience and Remote Sensing*, 41:1773–1784, 2003.

[5] D. Adalsteinsson and J.A. Sethian. A fast level set method for propagating interfaces. *Journal of Computational Physics*, 118(2):269–277, 1995.

[6] B.A. Afzelius and A.B. Maunsbach. Biological ultrastructure research: The first 50 years. *Tissue Cell*, 36(2):83–94, 2004.

[7] A. Al-Amoudi, J. Dubochet, H. Gnaegi, W. Lüthi, and D. Studer. An oscillating cryo-knife reduces cutting-induced deformation of vitreous ultrathin sections. *Journal of Microscopy*, 212(1):26–33, 2003.

[8] A. Al-Amoundi, J.J. Chang, A. Leforestier, A. McDowall, L.P. Salamin, L.M. Norlen, K. Richter, N.S. Blanc, D. Studer, and J. Dubochet. Cryo-electron microscopy of vitreous sections. *EMBO Journal*, 23(18):3583–3588, 2004.

[9] M. Aleksic, M. Smirnov, and S. Goma. Novel bilateral filter approach: Image noise reduction with sharpening. In *Proceeding of the Digital Photography II Conference*, pages 141–147. SPIE, 2006.

[10] L. Alparone, F. Boragine, and S. Fini. Parallel architectures for the postprocessing of SAR images. In *SPIE Proceedings*, volume 1360, pages 790–802, 1990.

[11] L. Alvarez, P.-L. Lions, and J.-M. Morel. Image selective smoothing and edge detection by nonlinear diffusion, II. *SIAM Journal on Numerical Analysis*, 29(3):845–866, 1992.

[12] E. Arbustini, M. Diegoli, R. Fasani, M. Grasso, P. Morbini, N. Banchieri, O. Bellini, B. Dal Bello, A. Pilotto, G. Magrini, C. Campana, P. Fortina, A. Gavazzi, J. Narula, and M. Viganò. Mitochondrial DNA mutations and mitochondrial abnormalities in dilated cardiomyopathy. *American Journal of Pathology*, 153:1501–1510, 1998.

[13] H.H. Arsenault and G. April. Properties of speckle integrated with a finite aperture and logarithmically transformed. *Journal of the Optical Society of America*, 66:1160–1163, 1976.

[14] T.J. Asaki, P.R. Campbell, R. Chartrand, C. Powell, K.R. Vixie, and B.E. Wohlberg. Abel inversion using total variation regularization: Applications. *Inverse Problems in Science and Engineering*, 14(8):873–885, 2006.

[15] V. Aurich and J. Weule. Non-linear Gaussian filters performing edge preserving diffusion. In *Proceedings of DAGM Symposium*, volume 17, pages 538–545. Deutsche Arbeitsgemeinschaft für Mustererkennung, 1995.

[16] S. Awate and R. Whitaker. Unsupervised, information-theoretic, adaptive image filtering for image restoration. *IEEE Transactions on Pattern Analysis and Machine Intelligence*, 28(3):364–376, 2006.

[17] M.R. Azimi-Sadjadi and S. Bannour. Two-dimensional adaptive block Kalman filtering of SAR imagery. *IEEE Transactions on Geoscience and Remote Sensing*, 29:742–753, 1991.

[18] S. Bae, S. Paris, and F. Durand. Two-scale tone management for photographic look. *ACM Transactions on Graphics*, 25(3):637–645, 2006.

[19] C. Bajaj, Q. Wu, and G. Xu. Level-set based volumetric anisotropic diffusion for 3d image denoising. ICES Technical Report 03-10, The University of Texas at Austin, austin, Texas, 2003.

[20] C. Bajaj and Z. Yu. *Geometric and Signal Processing of Reconstructed 3D Maps of Molecular Complexes*, chapter 23. Handbook of Computational Molecular Biology. Chapman & Hall/CRC Press, New York, New York, 2005.

[21] C. Bajaj, Z. Yu, and M. Auer. Volumetric feature extraction and visualization of tomographic molecular imaging. *Journal of Structural Biology*, 144(1-2):132–143, 2003.

[22] P. Bakker, L. van Vliet, and P. Verbeek. Edge preserving orientation adaptive filtering. In M. Boasson, J. Kaandorp, J. Tonino, and M. Vosselman, editors, *Proceedings of 5th Annual Conference of the Advanced School for Computing and Imaging*, pages 207–213, 1999.

[23] E. Bänsch and K. Mikula. A coarsening finite element strategy in image selective smoothing. *Computing and Visualization in Science*, 1(1):53–61, 1997.

[24] E. Bänsch and K. Mikula. Adaptivity in 3D image processing. *Computing and Visualization in Science*, 4(1):21–30, 2001.

[25] D. Barash. A fundamental relationship between bilateral filtering, adaptive smoothing and nonlinear diffusion equation. *IEEE Transactions on Pattern Analysis and Machine Intelligence*, 24(6):844–847, 2002.

[26] D. Barash and D. Comaniciu. A common framework for nonlinear diffusion, adaptive smoothing, bilateral filtering and mean shift. *Image and Video Computing*, 22(1):73–81, 2004.

[27] G.I. Barenblatt, M. Bertsch, R. Dal Passo, and M. Ughi. A degenerate pseudo-parabolic regularization of a nonlinear forward-backward heat equation arising in the theory of heat and mass exchange in stably stratified turbulent shear flow. *SIAM Journal on Mathematical Analysis*, 24(6):1414–1439, 1993.

[28] H.H. Barret and K.J. Myers. *Foundations of Image Science*, chapter 15. John Wiley & Sons, Inc., Hoboken, 2004.

[29] W. Baumeister. Electron tomorgraphy: Towards visualizing the molecular organization of the cytoplasm. *Current Opinion in Structural Biology*, 12:679–684, 2002.

[30] W.T. Baxter, A. Leith, and J. Frank. SPIRE: The SPIDER reconstruction engine. *Journal of Structural Biology*, 157(1):56–63, 2007.

[31] C. Bazán and B. Blomgren. Parameter-free adaptive total variation-based noise removal and edge strengthening for mitochondrial structure extraction. Research Report CSRCR 2007-16, San Diego State University, San Diego, California, 2007.

[32] C. Bazán and P. Blomgren. Adaptive finite element method for image processing. In *Proceedings of COMSOL Multiphysics Conference*, pages 377–381, Boston, Massachusetts, 2005.

[33] C. Bazán and P. Blomgren. Image smoothing and edge detection by nonlinear diffusion and bilateral filter. Research Report CSRCR 2007-21, San Diego State University, San Diego, California, 2007.

[34] C. Bazán and P. Blomgren. Total variation-based image and structure enhancement for electron tomography. Research Report CSRCR 2008-17, San Diego State University, San Diego, California, 2007.

[35] A. Belmonte. Temporal averaging of turbulence-induced uncertainties on coherent power measurements. *Optics Express*, 12(16):3770–3777, 2004.

[36] B. Benhamouda. Parameter adaptation for nonlinear diffusion in image processing. Master's thesis, University of Kaiserslautern, Kaiserslautern, Germany, 1994.

[37] E.P. Bennet and L. McMillan. Video enhancement using per-pixel virtual exposures. *ACM Transactions on Graphics*, 24(3):845–852, 2005.

[38] P. Bernardi. The permeability transition pore. Control points of a cyclosporin A-sensitive mitochondrial channel involved in cell death. *Biochimica et Biophysica Acta*, 1275:5–9, 1996.

[39] C. Best, S. Nickell, and W. Baumeister. Localization of protein complexes by pattern recognition. In J.R. McIntosh, editor, *Cellular Electron Microscopy*, volume 79 of *Methods in Cell Biology*, chapter 25, pages 615–637. Academic Press, San Diego, Califonia, 2007.

[40] J. Bigün and G.H. Granlund. Optimal orientation detection of linear symmetry. In *Proceedings of First International Conference on Computer Vision*, pages 433–438, London, England, 1987. IEEE Computer Society Press.

[41] M.J. Black and G. Sapiro. Edges as outliers: Anisotropic smoothing using local image statistics. In M. Nielsen, P. Johansen, O.F. Olsen, and J. Weickert, editors, *Lecture Notes in Computer Science*, number 1682, pages 259–270. Springer, Berlin, Germany, 1999.

[42] M.J. Black, G. Sapiro, D. Marimont, and D. Heeger. Robust anisotropic diffusion. *IEEE Transactions on Image Processing*, 7(3):421–432, 1998.

[43] Ya.M. Blanter. Recent advances in studies of current noise. Report cond-mat/0511478, Kavli Institute of Nanoscience, Delft University of Technology, Delft, The Netherlands, 2005.

[44] P. Blomgren, T. Chan, and P. Mulet. Extensions to total variation denoising. In *Proceedings of Society of Photo-Optical Instrumentation Engineers*, volume 3162, 1997.

[45] P. Blomgren and T.F. Chan. Color TV: Total variation methods for restoration of vector-valued images. *IEEE Transactions on Image Processing*, 7(3):304–309, 1998.

[46] J. Böhm, A.S. Frangakis, R. Hegerl, D. Nickell, S. Typke, and W. Baumeister. Toward detecting and identifying macromolecules in a cellular context: template matching applied to electron tomograms. *Proceedings of National Academy of Science*, 97(26):14245–14250, 2000.

[47] T. Boudier, J.P. Lechaire, G. Frebourg, C. Messaoudi, C. Mory, C. Colliex, F. Gaill, and S. Marco. A public software for energy filtering transmission electron tomography (EFTET-J): Application to the study of granular inclusions in

bacteria from Riftia pachyptila. *Journal of Structural Biology*, 151(2):151–159, 2005.

[48] J. Bouwer and M. Ellisman. Advances in electron microscope instrumentation and exploration of biological structures. In *SIAM Annual Meeting*, San Diego, California, 2008. Society for Industrial and Applied Mathematics.

[49] J.C. Bouwer, M.R. Mackey, A. Lawrence, T.J. Deerinck, Y.Z. Jones, M. Terada, M.E. Martone, S.T. Peltier, and M.H. Ellisman. The application of energy-filtered electron microscopy to tomography of thick, selectively stained biological samples. In J.R. McIntosh, editor, *Cellular Electron Microscopy*, volume 79 of *Methods in Cell Biology*, chapter 26, pages 643–660. Academic Press, San Diego, Califonia, 2007.

[50] S. Brandt, J. Heikkonen, and P. Engelhardt. Automatic alignment of transmission electron microscope tilt series without fiducial markers. *Journal of Structural Biology*, 136(3):201–213, 2001.

[51] S.S. Brandt. Markerless alignment in electron tomography electron tomography. In J. Frank, editor, *Electron Tomography: Methods for Three-Dimensional Visualization of Structures in the Cell*, chapter 6, pages 187–215. Springer, Berlin, Germany, 2nd edition, 2006.

[52] D.G. Breckenridge, M. Stojanovic, R.C. Marcellus, and G.C. Shore. Caspase cleavage product of BAP31 induces mitochondrial fission through endoplasmic reticulum calcium signals, enhancing cytochrome c release to the cytosol. *Journal of Cell Biology*, 160:1115–1127, 2003.

[53] T. Brox, R. van den Boomgaard, F. Lauze, J. van de Weijer, J. Weickert, P. Mrázek, and P. Kornprobst. Adaptive structure tensors and their applications. Technical Report 141, Universität des Saarlandes, Saarbrücken, Germany, 2005.

[54] T. Brox and J. Weickert. Nonlinear matrix diffusion for optic flow estimation. In L. van Gool, editor, *Lecture Notes in Computer Science*, pages 446–453. Springer-Verlag, Berlin, Germany, 2002.

[55] T. Brox, J. Weickert, B. Burgeth, and P. Mrázek. Nonlinear structure tensors. Technical Report 113, Universität des Saarlandes, Saarbrücken, Germany, 2004.

[56] T. Brox, J. Weickert, B. Burgeth, and P. Mrázek. Nonlinear structure tensors. *Image and Vision Computing*, 24(1):41–55, 2006.

[57] A. Buades, A. Chien, J.M. Morel, and S. Osher. Topology preserving linear filtering applied to medical imaging. *SIAM Journal on Imaging Science*, 1(1):26–50, 2008.

[58] A. Buades, B. Coll, and J.-M. Morel. Neighborhood filters and PDE's. *Numerische Mathematik*, 105(1):1–34, 2006.

[59] A. Buades, B. Coll, and J.-M. Morel. The staircasing effect in neighborhood filters and its solution. *IEEE Transactions on Image Processing*, 15(6):1499–1505, 2006.

[60] A. Canny. A computational approach to edge detection. *IEEE Transactions on Pattern Analysis and Machine Intelligence*, 8(6):679–698, 1986.

[61] J.-M. Carazo. The fidelity of 3D reconstructions from incomplete data and the use of restoration methods. In J. Frank, editor, *Electron Tomography: Three-Dimensional Imaging with the Transmission Electron Microscope*, chapter 6, pages 117–164. Plenum, New York, New York, 1992.

[62] F. Catté, P.-L. Lions, J.-M. Morel, and T. Coll. Image selective smoothing and edge detection by nonlinear diffusion. *SIAM Journal of Numerical Analysis*, 29(1):182–193, 1992.

[63] A. Chambolle. An algorithm for total variation minimization and applications. *Journal of Mathematical Imaging and Vision*, 20(1-2):89–97, 2004.

[64] A. Chambolle and P.L. Lions. Image recovery via total variation minimization and related problems. *Journal of Numerical Mathematics*, 76(2):167–188, 1997.

[65] T. Chan and S. Esedoglu. Aspects of total variation regularized L^1 function approximation. Technical Report CAM 05-01, University of California Los Angeles, Los Angeles, California, 2004.

[66] T.F. Chan and L.A. Vese. Active contours without edges. *IEEE Transactions on Image Processing*, 10(2):266–277, 2001.

[67] F. Charrière, B. Rappaz, J. Jühn, T. Colomb, P. Marquet, and C. Depeursinge. Influence of shot noise on phase measurement accuracy in digital holographic microscopy. *Optics Express*, 15(14):8818–8831, 2007.

[68] J. Chen, S. Paris, and F. Durand. Real-time edge-aware image processing with bilateral grid. *ACM Transactions on Graphics*, 26(3):Article No. 103, 2007.

[69] Y. Chen, S. Levine, and M. Rao. Variable exponent, linear growth functions in image restoration. *SIAM Journal on Applied Mathematics*, 66(4):1383–1406, 2006.

[70] E. Cole. The removal of unknown image blurs by homomorphic filtering. Technical Report 0038, Department of Electrical Engineering, University of Toronto, Toronto, Canada, 1973.

[71] T. Colomb, E. Dürr, E. Cuche, P. Marquet, H. Limberger, R.-P. Salathé, and C. Depeursinge. Polarization microscopy by use of holography: application to digital fiber birefringence measurements. *Applied Optics*, 44:4461–4469, 2005.

[72] P.L. Combettes. Image restoration subject to a total variation constraint. *IEEE Transactions on Image Processing*, 13(9):1213–1222, 2004.

[73] G.-H. Cottet. Neural networks: Continuous approach and applications to image processing. *Journal of Biological Systems*, 3:1131–1139, 1995.

[74] G.-H. Cottet and L. Germain. Image processing through reaction combined with nonlinear diffusion. *Mathematics of Computation*, 61(204):659–673, 1993.

[75] T.R. Crimmins. Geometric filter for speckle reduction. *Applied Optics*, 24:1438–1443, 1985.

[76] R.A. Crowther, D.J. De Rosier, and A. Klug. The reconstruction of a three-dimensional structure from projections and its application to electron microscopy. *Proceedings of Royal Society of London, Series A, Mathematical and Physical Sciences*, 317:319–340, 1970.

[77] R.N. Czerwinski, D.L. Jones, and W.D. O'Brien. Ultrasound speckle reduction by directional median filtering. In *Proceedings of EIII International Conference on Image Processing*, volume 1, pages 358–361, 1995.

[78] I. Daberkow, K.-H. Herrmann, L. Liu, and W.D. Rau. Performance of electron image converters with YAG single-crystal screen and CCD sensor. *Ultramicroscopy*, 38(3-4):215–223, 1991.

[79] J. Darbon and M. Sigelle. Image restoration with constrained total variation. part I: Fast and exact minimization. *Journal of Mathematical Imaging and Vision*, 26(3):261–276, 2006.

[80] J. Darbon and M. Sigelle. Image restoration with constrained total variation. part II: Levelable functions, convex priors and non-convex cases. *Journal of Mathematical Imaging and Vision*, 26(3):277–292, 2006.

[81] D.J. De Rosier and A. Klug. Reconstruction of three dimensional structures from electron micrographs. *Nature*, 217:130–134, 1968.

[82] K.J. De Vos, A.J. Allan, V.J. Grierson, and M.P. Sheetz. Mitochondrial function and actin regulate dynamin-related protein 1-dependent mitochondrial fission. *Current Biology*, 15:678–683, 2005.

[83] K.J. De Vos and M.P. Sheetz. Visualization and quantification of mitochondria dynamics in living animal cells. In L.A. Pon and E.A. Schon, editors, *Mitochondria*, volume 80 of *Methods in Cell Biology*, chapter 30, pages 627–682. Academic Press, San Diego, California, 2007.

[84] R. DeVore, B. Jawerth, and B. Lucier. Image compression through wavelet transform coding. *IEEE Transactions on Information Theory*, 38:719–746, 1992.

[85] K. Dierksen, D. Typke, R. Hegerl, and W. Baumeister. Towards automatic electron tomography II. Implementation of autofocus and low-dose procedures. *Ultramicroscopy*, 49(1-4):109–120, 1993.

[86] K. Dierksen, D. Typke, R. Hegerl, A.J. Koster, and W. Baumeister. Towards automatic electron tomography. *Ultramicroscopy*, 40(1):71–87, 1992.

[87] K. Dierksen, D. Typke, R. Hegerl, J. Walz, E. Sackmann, and W. Baumeister. Three-dimensional structure of lipid vesicles embedded in vitreous ice and investigated by automated electron tomography. *Biophysical Journal*, 68:1416–1422, 1995.

[88] U. Diewald, T. Preusser, M. Rumpf, and R. Strzodka. Diffusion models and their accelerated solution in image and surface processing. *Acta Mathematica Universitatis Comenianae*, 70(1):15–34, 2001.

[89] D.A. Díez, A. Seybert, and A.S. Frangakis. Tilt-series and electron microscope alignment for the correction of the non-perpendicularity of beam and tilt-axis. *Journal of Structural Biology*, 154(2):195–205, 2006.

[90] S. DiMauro and E.A. Schon. Mitochondrial DNA mutations in human disease. *American Journal of Medical Genetics*, 106:18–26, 2001.

[91] M. Djaldetti. Mitochondrial abnormalities in the cells of myeloma patients. *Acta Haematologica*, 68:241–248, 1982.

[92] C. Dolcetta and I. Ferretti. Optimal stopping time formulation of adaptive image filtering. *Applied Mathematics and Optimization*, 43(3):245–258, 2001.

[93] J. Dubochet, M. Adrian, J.J. Chang, J.C. Homo, J. Lepault, A.W. McDowall, and P. Schultz. Cryo-electron microscopy of vitrified specimens. *Quarterly Reviews of Biophysics*, 21:129–228, 1988.

[94] J. Dubochet, A.W. McDowall, B. Menge, E.N. Schmid, and K.G. Lickfeld. Electron microscopy of frozen-hydrated bacteria. *Journal of Bacteriology*, 155:381–390, 1983.

[95] J. Dubochet and N. Sartori Blanc. The cell in absence of aggregation artifacts. *Micron*, 32(1):91–99, 2001.

[96] J. Dubochet, B. Zuber, M. Eltsov, C. Bouchet-Marquis, and A. Al-Amoudi. How to "read" a vitreous section. In J.R. McIntosh, editor, *Cellular Electron Microscopy*, volume 79 of *Methods in Cell Biology*, chapter 15, pages 385–406. Academic Press, San Diego, Califonia, 2007.

[97] F. Durand and J. Dorsey. Fast bilateral filtering for the display of high-dynamic-range images. *ACM Transactions on Graphics*, 21(3):257–266, 2002.

[98] V. Dutt. *Statistical analysis of ultrasound echo envelope*. PhD thesis, Mayo Graduate School, Rochester, MN, 1995.

[99] R.F. Egerton, P. Li, and M. Malac. Radiation damage in the tem and sem. *Micron*, 35(6):399–409, 2004.

[100] E. Eisemann and F. Durand. Flash photography enhancement via intrinsic relighting. *ACM Transactions on Graphics*, 23(3):673–678, 2004.

[101] M. Elad. On the bilateral filter and ways to improve it. *IEEE Transactions on Image Processing*, 11(10):1141–1151, 2002.

[102] M. Elad. Retinex by two bilateral filters. *Lecture Notes in Computer Science*, 3459:217–229, 2005.

[103] G.Y. Fan, P. Datte, E. Beuville, J.-F. Beche, J. Millaud, K.H. Downing, F.T. Burkard, Ellisman M.H., and N.-H. Xuong. A SIC-based event-driven 2D digital electron counter for TEM imaging. *Ultramicroscopy*, 70(3):107–113, 1998.

[104] G.Y. Fan and M.H. Ellisman. High-sensitivity lens-coupled slow-scan CCD camera for transmission electron microscopy. *Ultramicroscopy*, 52(1):21–29, 1993.

[105] G.Y. Fan and M.H. Ellisman. Digital imaging in transmission electron microscopy. *Journal of Microscopy*, 200(1):1–13, 2000.

[106] D. Fanelli and O. Öktem. Electron tomography: a short overview with an emphasis on the absorption potential model for the forward problem. *Inverse Problems*, 24(1):1–51, 2008.

[107] A.R. Faruqi, H.N. Andrews, and R. Henderson. A high sensitivity imaging detector for electron microscopy. *Nuclear Instruments and Methods in Physics Research*, A367:408–412, 1995.

[108] A.R. Faruqi and S. Subramaniam. CCD detectors in high-resolution biological electron microscopy. *Quarterly Reviews of Biophysics*, 33(1):1–27, 2000.

[109] J.-J. Fernández, C.O.S. Sorzano, R. Marabini, and J.-M. Carazo. Image processing and 3-D reconstruction in electron microscopy. *IEEE Signal Processing Magazine*, 23(3):84–94, 2006.

[110] J.J. Fernández, A.F. Lawrence, J. Roca, I. García, M.H. Ellisman, and J.M. Carazo. High-performance electron tomography of complex biological specimens. *Journal of Structural Biology*, 138(1-2):6–20, 2002.

[111] J.J. Fernández and S. Li. An improved algorithm for anisotropic nonlinear diffusion for denoising cryo-tomograms. *Journal of Structural Biology*, 144(1/2):152–161, 2003.

[112] J.J. Fernández and S. Li. Anisotropic nonlinear filtering of cellular structures in cryo-electron tomography. *Computing in Science and Engineering*, 7(5):54–61, 2005.

[113] Fernández, J.-J. and Carazo, J.-M. and García, I. Three-dimensional reconstruction of cellular structures by electron microscope tomography and parallel computing. *Journal of Parallel and Distributed Computing*, 64(2):285–300, 2004.

[114] W. Förstner and E. Gülch. A fast operator for detection and precise location of distinct points, corners and centres of circular features. In *Proceedings of ISPRS Intercommission Conference on Fast Processing of Photogrammetric Data*, pages 281–305, 1987.

[115] S. Foucher, G.B. Bénié, and J.-M. Boucher. Multiscale MAP filtering of SAR images. *IEEE Transactions on Image Processing*, 10(1):49–56, 2001.

[116] S. Foucher, G. Farage, and G. Benie. SAR image filtering based on the stationary contourlet transform. In *Proceedings of IEEE International Conference on Geoscience and Remote Sensing Symposium*, pages 4021–4024, 2006.

[117] A.S Frangakis and F. Förster. Computational exploration of structural information from cryo-electron tomograms. *Current Opinion in Structural Biology*, 14(3):325–331, 2004.

[118] A.S. Frangakis and R. Hegerl. Nonlinear anisotropic diffusion in three-dimensional electron microscopy. In G.G. Leeuwen and van Hartmanis J., editors, *Lecture Notes in Computer Science*, volume 1682, pages 386–397. Springer Verlag, Berlin, Germany, 1999.

[119] A.S. Frangakis and R. Hegerl. Noise reduction in electron tomographic reconstruction using nonlinear anisotropic diffusion. *Journal of Structural Biology*, 135(3):239–250, 2001.

[120] A.S. Frangakis and R. Hegerl. Segmentation of two- and three-dimensional data from electron microscopy using eigenvector analysis. *Journals of Structural Biology*, 138(1-2):105–113, 2002.

[121] A.S. Frangakis, A. Stoschek, and R. Hegerl. Wavelet transform filtering and nonlinear anisotropic diffusion assessed for signal reconstruction performance on multidimensional biomedical data. *IEEE Transactions on Biomedical Engineering*, 48(2):213–222, 2001.

[122] J. Frank. *Three-Dimensional Electron Microscopy of Macromolecular Assemblies: Visualization of Biological Molecules in Their Native State*. Oxford University Press, Oxford, United Kingdom, 2006.

[123] J. Frank and B.F. McEwen. Alignment by cross-correlation. In J. Frank, editor, *Electron Tomography: Three-Dimensional Imaging with the Transmission Electron Microscope*, chapter 9, pages 205–213. Plenum, New York, New York, 1992.

[124] J. Frank, M. Radermacher, P. Penczek, J. Zhu, Y. Li, M. Ladjadj, and A. Leith. SPIDER and WEB: Processing and visualization of images in 3D electron microscopy and related fields. *Journal of Structural Biology*, 116(1):190–199, 1996.

[125] J. Frank, T. Wagenlnecht, B.F. McEwen, M. Marko, C.E. Hsich, and C.A. Mannella. Three-dimensional imaging of biological complexity. *Journal of Structural Biology*, 138:85–91, 2002.

[126] S. Frank, B. Gaume, E. Bergmann-Leitner, W. Leitner, E. Robert, F. Catez, C. Smith, and R. Youle. The role of dynamin-related protein 1, a mediator of mitochondrial fission, in apoptosis. *Developmental Cell*, 1(4):515–525, 2001.

[127] T.G. Frey, G.A. Perkins, and M.H. Ellisman. Electron tomography of membrane-bound cellular organelles. *The Annual Review of Biophysics and Biomolecular Structure*, 35:199–224, 2006.

[128] T.G. Frey, C.W. Renken, and G.A. Perkins. Insight into mitochondrial structure and function from electron tomography. *Biochimica et Biophysica Acta*, 1555(1-3):196–203, 2002.

[129] D.S. Fritsch. A medical description of grayscale image structure by gradient-limited diffusion. In R. Robb, editor, *Visualization in Biomedical Computing*, volume 1808, pages 105–117. Society of Photo-Optical Instrumentation Engineers, 1992.

[130] D.S. Fritsch, S.M. Pizer, and J.M. Coggins. A multiscale medial description of grayscale image structure. In *Proceedings of Advances in Intelligent Robotic Systems*. SPIE, 1991.

[131] J. Fröhlich and J. Weickert. Image processing using a wavelet algorithm for nonlinear diffusion. Report 104, Laboratory of Technomathematics, University of Kaiserslautern, Kaiserslautern, Germany, 1994.

[132] V.S. Frost, J.A. Stiles, K.S. Shanmugan, and J.C. Holtzman. A model for radar images and its application to adaptive digital filtering of multiplicative noise. *IEEE Transactions on Pattern Analysis and Machine Intelligence*, PAMI-4:157–166, 1982.

[133] L. Gagnon, Drissi, and F. Smaili. Speckle noise reduction of airborne SAR images with symmetric daubechies wavelets. In *SPIE Proceedings*, volume 2759, pages 14–24, 1996.

[134] L. Gagnon and A. Jouan. Speckle filtering of SAR images—a comparative study between complex wavelet-based and standard filters. Technical report, Department of R&D, Lockheed Martin, Canada, 1997.

[135] L. Gagnon, H. Oppenheim, and P. Valin. R&D activities in airborne SAR image processing-analysis at Lockheed Martin, Canada. Technical report, Lockheed Martin, Canada, 1998.

[136] N. Gallagher, D.W. Sweeney, C.R. Christensen, G.R. Arce, P.K. Murphy, and J.P. Fitch. Speckle noise filtering by use of median filter root signals. *Journal of the Optical Society of America A: Optics, Image Science & Vision*, 72:1743–+, 1982.

[137] D. Geiger and A. Yuille. A common framework for image segmentation. *International Journal of Computer Vision*, 6(3):227–243, 1991.

[138] P.F.C. Gilbert. Iterative methods for 3-dimensional reconstruction of an object from projections. *Journal of Theoretical Biology*, 36(1):105–117, 1972.

[139] P.F.C. Gilbert. The reconstruction of a three-dimensional structure from projections and its application to electron microscopy. II. direct methods. In *Proceedings of the Royal Society of London. Series B, Biological Sciences*, volume 182, pages 89–102. The Royal Society, 1972.

[140] G. Gilboa. *Super-resolution Algorithms Based on Inverse Diffusion-type Processes*. PhD thesis, Israel Institute of Technology, Haifa, Israel, 2004.

[141] R.M. Glaeser. Limitations to significant information in biological electron microscopy as a result of radiation damage. *Journal of Ultrastructure Research*, 36(3-4):466–482, 1971.

[142] R.M. Glaeser and K.A. Taylor. Radiation damage relative to transmission electron microscopy of biological specimens at low temperature: a review. *Journal of Microscopy*, 112:127–138, 1978.

[143] T.D. Goddard, C.C. Huang, and T.E. Ferrin. Visualizing density maps with UCSF Chimera. *Journal of Structural Biology*, 157(1):281–287, 2007.

[144] D. Goldfarb and W. Yin. Second order cone programming methods for total variation based image restoration. *SIAM Journal on Scientific Computing*, 27(2):622–645, 2002.

[145] G. Golub, T. Chan, and P. Mulet. A nonlinear primal-dual method for total variation-based image restoration. *SIAM Journal on Scientific Computing*, 20(6):1964–1977, 1999.

[146] J.W. Goodman. *Statistical Properties of Laser Speckle Patterns*. Springer-Verlag, Heidelberg, Germany, 1980.

[147] J.W. Goodman. *Speckle phenomenon in optics: theory and applications*. Roberts and Company, Denver, 2006.

[148] R. Gordon, R. Bender, and G.T. Herman. Algebraic reconstruction techniques (ART) for three-dimensional electron microscopy and x-ray photography. *Journal of Theoretical Biology*, 29(3):471–481, 1970.

[149] D.R. Green and J.C. Reed. Mitochondria and apoptosis. *Science*, 281(5381):1309–1312, 1998.

[150] R. Grimm, M. Bärmann, W. Häckl, D. Typke, E. Sackmann, and W. Baumeister. Energy filtered electron tomography of ice-embedded actin and vesicles. *Biophysical Journal*, 72:482–489, 1997.

[151] R. Grimm, H. Singh, R. Rachel, D. Typke, W. Zillig, and W. Baumeister. Electron tomography of ice-embedded prokaryotic cells. *Biophysical Journal*, 74(2 Pt 1):1031–1042, 1998.

[152] W. Grogger, B. Schaffer, K.M. Krishnan, and F. Hofer. Energy-filtering tem at high magnification: spatial resolution and detection limits. *Ultramicroscopy*, 96(3-4):481–489, 2003.

[153] F. Guichard, J.M. Morel, and R. Ryan. Contrast invariant image analysis and PDEs. http://www.cmla.ens-cachan.fr/fileadmin/Membres/morel/JMMBookOct04.pdf, 2001.

[154] H. Guo, J.E. Odegard, M. Lang, R.A. Gopinath, I.W. Selesnick, and C.S. Burrus. Wavelet based speckle reduction with application to SAR based ATD/R. In *IEEE Proceedings of ICIP '94*, pages 75–79, 1994.

[155] N. Gupta, M.N.S. Swamy, and E. Plotkin. Despeckling of medical ultrasound images using data and rate adaptive lossy compression,. *IEEE Transactions on Medical Imaging*, 24(6):743–754, 2005.

[156] A. Handlovičová, K. Mikula, and A. Sarti. Numerical solution of parabolic equations related to level set formulation of mean curvature flow. *Computing and visualization in Science*, 1(2):179–182, 1999.

[157] A. Handlovičová, K. Mikula, and F. Sgallari. Variational numerical methods for solving nonlinear diffusion equations arising in image processing. *Journal for Visual Communication and Image Representation*, 13(1-2):217–237, 2002.

[158] A. Handlovičová, K. Mikula, and F. Sgallari. Semi-implicit complementary volume scheme for solving level set like equations in image processing and curve evolution. *Numerische Mathematik*, 93(4):675–669, 2003.

[159] M.L. Harlow, D. Ress, A. Stoschek, R.M. Marshall, and U.J. McMahan. The architecture of active zone material at the frog's neuromuscular junction. *Nature*, 409(6819):479–484, 2001.

[160] R.G. Hart. Electron microscopy of unstained biological material: The polytropic montage. *Science*, 159:1464–1467, 1968.

[161] P.W. Hawkes and E. Kasper. Principles of electron optics. In *Wave Optics*, volume 3. Academic, New York. New York, 1994.

[162] G.E. Healey and R. Kondepudy. Radiometric CCD camera calibration and noise estimation. *IEEE Transactions on Pattern Analysis and Machine Intelligence*, 16(3):267–276, 1994.

[163] R. Hegerl and A.S. Frangakis. Denoising of electron tomograms electron tomography. In J. Frank, editor, *Electron Tomography: Methods for Three-Dimensional Visualization of Structures in the Cell*, chapter 11, pages 331–352. Springer, Berlin, Germany, 2nd edition, 2006.

[164] R. Hegerl and W. Hoppe. Influence of electron noise on three-dimensional image reconstruction. *Zeitschrift Naturforsch*, 314(12):1717–1721, 1976.

[165] R. Henderson. Realizing the potential of electron cryo-microscopy. *Quarterly Reviews of Biophysics*, 37(1):3–13, 2004.

[166] E. Hervet, R. Fjortoft, P. Marthon, and A. Lopes. Comparison of wavelet-based and statistical speckle filters. In *EUROPTO Conference on SAR Image Analysis, Modeling, and Techniques,*, volume 3497, pages 43–54, 1998.

[167] D. Hessler, S.J. Young, and M.H. Ellisman. A flexible environment for the visualization of three-dimensional biological structures. *Journal of Structural Biology*, 116(1):113–119, 1996.

[168] D.H. Hoekman. Speckle ensemble statistics of logarithmically scaled data. *IEEE Transactions on Geoscience and Remote Sensing*, 29(1):180–182, 1991.

[169] K. Höllig. Existence of infinitely many solutions for a forward-backward heat equation. *Transactions of the American Mathematical Society*, 278(1):299–319, 1983.

[170] K. Höllig and J.A. Nohel. A diffusion equation with a non-monotone constitutive function. In J.M. Ball, editor, *Proceedings of NATO/London Mathematical Society Conference on Systems of Partial Differential Equation*, pages 409–422, 1983.

[171] J.L. Höög and C. Antony. Whole-cell investigation of microtubule cytoskeleton architecture by ET. In J.R. McIntosh, editor, *Cellular Electron Microscopy*, volume 79 of *Methods in Cell Biology*, chapter 6, pages 145–167. Academic Press, San Diego, Califonia, 2007.

[172] W. Hoppe and R. Hegerl. Some remarks concerning the influence of electron noise on 3d reconstruction. *Ultramicroscopy*, 6(1):205–206, 1981.

[173] C. Humphreys. High voltage electron microscopy. In M.A. Hayat, editor, *Principles and Techniques of Electron Microscopy. Biological Applications*, volume 6, chapter 1, pages 1–39. Van Nostrand-Reinhold, Princeton, New Jersey, 1976.

[174] K. Ishizuka. Analysis of electron image detection efficiency of slow-scan ccd cameras. *Ultramicroscopy*, 52(1):7–20, 1993.

[175] J.A. Izatt, M.D. Kulkarni, H.-W. Wang, K. Kobayashi, and M.V. Sivak. Optical coherence tomography and microscopy in gastrointestinal tissues. *IEEE Journal of Selected Topics in Quantum Electronics*, 2(4):1017–1028, 1996.

[176] A.K. Jain. *Fundamental of Digital Image Processing.* Prentice-Hall, Upper Saddle River, NJ, 1989.

[177] J.R. Janesick, T. Elliott, S. Collins, M.M. Blouke, and J. Freeman. Scientific charge-coupled devices. *Optical Engineering*, 26:692–714, 1987.

[178] W. Jiang, M.L. Baker, Q. Wu, C. Bajaj, and W. Chiu. Applications of a bilateral denoising filter in biological electron microscopy. *Journal of Structural Biology*, 144(1/2):114–122, 2003.

[179] E. Jonsson, S.C. Huang, and T. Chan. Total variation regularization in positron emission tomography. Technical Report, University of California Los Angeles, Los Angeles, 1998.

[180] S.P. Kantrow and C.A. Piantadosi. Release of cytochrome c from liver mitochondria during permeability transition. *Biochemical and Biophysical Research Communications*, 232:669–671, 1997.

[181] D. Kaplan and Q. Ma. On the statistical characteristics of log-compressed rayleigh signals. In *Proceedings of IEEE Ultrasonics Symposium*, volume 2, pages 961–964, 1993.

[182] J. Kačur and K. Mikula. Solution of nonlinear diffusion appearing in image smoothing and edge detection. *Applied Numerical Mathematics*, 17(1):47–59, 1995.

[183] B. Kawohl. Remarks on the operator $\operatorname{div}(\nabla u/|\nabla u|)$. In V. Oliker and A. Treibergs, editors, *Contemporary Mathematics 127*, pages 69–83. American Mathematical Society: Geometry and nonlinear partial differential equations, Providence, Rhode Island, 1992.

[184] E. Kellenberger. The potential of cryofixation and freeze substitution: Observation and theoretical considerations. *Journal of Microscopy*, 161(2):183–203, 1991.

[185] S. Kichenassamy. The Perona-Malik paradox. *SIAM Journal of Applied Mathematics*, 57(5):1328–1342, 1997.

[186] K.W. Kinnally, T.A. Lohret, M.L. Campo, and C.A. Mannella. Perspective on mitochondrial multiple conductance channel. *Journal of Bioenergetics and Biomembranes*, 28:115–123, 1996.

[187] D.M. Kirby, D.R. Thorburn, D.M. Turnbull, and R.W. Taylor. Biochemical assays of respiratory chain complex activity. In L.A. Pon and E.A. Schon, editors, *Mitochondria*, volume 80 of *Methods in Cell Biology*, chapter 4, pages 93–119. Academic Press, San Diego, California, 2007.

[188] P. Kisilev, M. Zibulevsky, and Y.Y. Zeevi. Wavelet representation and total variation regularization in emission tomography. In *Proceedings of International Conference on Image Processing*, volume 1, pages 702–705, 2001.

[189] J.J. Koenderink. The structure of images. *Biological Cybernetics*, 50(5):363–370, 1984.

[190] A.J. Koster and M. Bárcena. Cryotomograhy: low-dose automated tomography of frozen-hydrated specimens. In J. Frank, editor, *Electron Tomography: Methods for Three-Dimensional Visualization of Structures in the Cell*, chapter 4, pages 113–161. Springer, Berlin, Germany, 2nd edition, 2006.

[191] A.J. Koster, W.J. de Ruijter, A. Van Den Bos, and K.D. Van Der Mast. Autotuning of a TEM using minimum electron dose. *Ultramicroscopy*, 27(3):251–272, 1989.

[192] J.R. Kremer, D.N. Mastronarde, and J.R. McIntosh. Computer visualization of three-dimensional image data using IMOD. *Journal of Structural Biology*, 116(1):71–76, 1996.

[193] Z. Krivá and K. Mikula. An adaptive finite volume scheme for solving nonlinear diffusion in image processing. *Journal for Visual Communication and Image Representation*, 13(1-2):22–35, 2002.

[194] O.L. Krivanek and P.E. Mooney. Applications of slow-scan CCD cameras in transmission electron microscopy. *Ultramicroscopy*, 49(1-4):95–108, 1993.

[195] G. Kroemer, B. Dallaporta, and M. Resche-Rigon. The mitochondrial death/life regulator in apoptosis and necrosis. *Annual Review of Physiology*, 60:619–642, 1998.

[196] G. Kroemer, P.X. Petit, N. Zamzami, J.-L. Vayssière, and B. Mignotte. The biochemistry of apoptosis. *Federation of American Societies for Experimental Biology Journal*, 9:1277–1287, 1995.

[197] G. Kroemer, N. Zamzami, and S.A. Susin. Mitochondrial control of apoptosis. *Immunology Today*, 18:44–51, 1997.

[198] D. Kuan, A. Sawchuk, T. Strand, and P. Chavel. Adaptive restoration of images with speckle. *IEEE Transactions on Acoustics, Speech, & Signal Processing*, 35(3):373–383, 1987.

[199] D.T. Kuan, A.A. Sawchuk, T.C. Strand, and P. Chavel. Adaptive noise smoothing filter for images with signal–dependent noise. *IEEE Transactions on Pattern Analysis and Machine Intelligence*, PAMI-7:165–177, 1985.

[200] S. Kujawa and D. Krahl. Performance of a low-noise CCD camera adapted to a transmission electron microscope. *Ultramicroscopy*, 46(1-4):395–403, 1992.

[201] M. Kuwahara, K. Hachimura, S. Eiho, and M. Kinoshita. Processing of riangiocardiographic images. In K. Preston and M. Onoe, editors, *Digital Processing of Biomedical Images*, pages 187–202. Plenum Press, New York, New York, 1976.

[202] A. Lawrence, J.C. Bouwer, G.A. Perkins, and M.H. Ellisman. Transform-based backprojection for volume reconstruction of large format electron microscope tilt series. *Journal of Structural Biology*, 154(2):144–167, 2006.

[203] K. Lebart and J.-M. Boucher. Speckle filtering by wavelet analysis and synthesis. In *SPIE Proceedings*, volume 2825, pages 644–651, 1996.

[204] J.-S. Lee. Digital image enhancement and noise filtering by use of local statistics. *IEEE Transactions on Pattern Analysis and Machine Intelligence*, PAMI-2:165–168, 1980.

[205] A.P. Leis, M. Beck, M. Gruska, C. Best, R. Hegerl, W. Baumeister, and J.W. Leis. Cryo-electron tomography of biological specimens. *IEEE Signal Processing Magazine*, 23(3):95–103, 2006.

[206] J.V. Leonard and A.V.H. Schapira. Mitochondrial respiratory chain disorders I: Mitochondrial DNA defects. *Lancet*, 355:299–304, 2000.

[207] J.V. Leonard and A.V.H. Schapira. Mitochondrial respiratory chain disorders II: Neurodegenerative disorders and nuclear gene defects. *Lancet*, 355:389–394, 2000.

[208] S. Levine, Y. Chen, and J. Stanich. Image restoration via nonstandard diffusion. Technical Report 04-01, Department of Mathematics and Computer Science, Duquesne University, Pittsburgh, Pennsylvania, 2004.

[209] R.M. Lewitt. Alternatives to voxels for image representation in iterative reconstruction algorithms. *Physics in Medicine and Biology*, 37(3):705–716, 1992.

[210] C. Li, C. Xu, C. Gui, and M.D. Fox. Level set evolution without re-initialization: A new variational formulation. In *Proceedings of IEEE International Conference on Computer Vision and Pattern Recognition*, pages 430–436, 2005.

[211] X. Li and T. Chen. Nonlinear diffusion with multiple edginess thresholds. *Pattern Recognition*, 27(8):1029–1037, 1994.

[212] Y. Li, A. Leith, and J. Frank. Tinkerbell: A tool for interactive segmentation of 3D data. *Journal of Structural Biology*, 120(3):266–275, 1997.

[213] P.-L. Lions, S. Osher, and L.I. Rudin. Denoising and deblurring images using constrained nonlinear partial differential equations. Technical report, Cognitech, Inc., Pasadena, California, 1993.

[214] C. Liu, W.T. Freeman, R. Szeliski, and S. Kang. Noise estimation from a single image. In *Proceedings of IEEE Computer Society Conference on Computer Vision and Pattern Recognition*, volume 1, pages 901–908, 2006.

[215] X.S. Liu, C.N. Kim, J. Yang, R. Jemmerson, and X. Wang. Induction of apoptotic program in cell-free extracts: Requirements for dATP and cytochrome c. *Cell*, 86:147–157, 1996.

[216] R.F. Loane, E.J. Kirkland, and J. Silcox. Visibility of single heavy atoms on thin crystaline silicon in simulated annular dark-field images. *Acta Crystallographica Section A*, 44:912–927, 1988.

[217] A. Lopes, E. Nezry, R. Touzi, and H. Laur. Structure detection and statistical adaptive speckle filtering in SAR images. *International Journal of Remote Sensing*, 14(9):17351758, 1993.

[218] S.J. Ludtke, P.R. Baldwin, and W. Chiu. EMAN: Semiautomated software for high-resolution single-particle reconstructions. *Journal of Structural Biology*, 128(1):82–97, 1999.

[219] P.K. Luther. Sample shrinkage and radiation damage of plastic sections. In J. Frank, editor, *Electron Tomography: Methods for Three-Dimensional Visualization of Structures in the Cell*, chapter 1, pages 17–48. Springer, Berlin, Germany, 2nd edition, 2006.

[220] Lučić, V. and Förster, F. and Baumeister, W. Structural studies by electron tomography: From cells to molecules. *Annual Review of Biochemistry*, 74:833–865, 2005.

[221] M. Lysaker and X.-C. Tai. Iterative image restoration combining total variation minimization and a second-order functional. *International Journal of Computer Vision*, 66(1):5–18, 2006.

[222] R. Malladi, J.A. Sethian, and B.C. Vemuri. A fast level set based algorithm for topology-independent shape modeling. *Journal of Mathematical Imaging and Vision*, 6(2/3):269–289, 1996.

[223] S.P. Mallick, B. Carragher, C.S. Potter, and D.J. Kriegman. ACE: Automated CTF estimation. *Ultramicroscopy*, 104(1):8–29, 2005.

[224] R. Marabini, G.T. Herman, and J.-M. Carazo. 3d reconstruction in electron microscopy using art with smooth spherically symmetric volume elements (blobs). *Ultramicroscopy*, 72(1-2):53–65, 1998.

[225] R. Marabini, E. Rietzel, R. Schroeder, G. T. Herman, and J.M. Carazo. Three-dimensional reconstruction from reduced sets of very noisy images acquired following a single-axis tilt schema: Application of a new three-dimensional reconstruction algorithm and objective comparison with weighted backprojection. *Journal of Structural Biology*, 120(3):363–371, 1997.

[226] P. Marchetti, M. Castedo, S.A. Susin, N. Zamzami, T. Hirsch, A. Haeffner, F. Hirsch, M. Geuskens, and G. Kroemer. Mitochondrial permeability transition is a central coordinating event of apoptosis. *Journal of Experimental Medicine*, 184:1155–1160, 1996.

[227] S. Marco, T. Bouldier, C. Messaoudi, and J.-L. Rigaud. Electron tomography of biological samples. *Biochemistry*, 69(11):1219–1225, 2004.

[228] A. Marquina and S. Osher. Explicit algorithms for a new time dependent model based on level set motion for a nonlinear debluring and noise removal. *SIAM Journal on Scientific Computing*, 22(2):387–405, 2000.

[229] D. Marr and E. Hildreth. Theory of edge detection. In *Proceedings of Royal Society of London. Series B, Biological Sciences*, volume 207, pages 187–217. Royal Society Publishing, 1980.

[230] D.N. Mastronarde. Dual-axis tomography: An approach with alignment methods that preserve resolution. *Journal of Structural Biology*, 120(3):343–352, 1997.

[231] D.N. Mastronarde. Automated electron microscope tomography using robust prediction of specimen movements. *Journal of Structural Biology*, 152(1):36–51, 2005.

[232] D.N. Mastronarde. Fiducial marker and hybrid alignment methods for single- and double-axis tomography. In J. Frank, editor, *Electron Tomography: Methods for Three-Dimensional Visualization of Structures in the Cell*, chapter 5, pages 163–185. Springer, Berlin, Germany, 2nd edition, 2006.

[233] S. Matej, R.M. Lewitt, and G.T. Herman. Practical considerations for 3-D image reconstruction using spherical symmetric volume elements. *IEEE Transactions on Medical Imaging*, 15(1):68–78, 1996.

[234] K. McDonald. Cryopreparation methods for electron microscopy. In J.R. McIntosh, editor, *Cellular Electron Microscopy*, volume 79 of *Methods in Cell Biology*, chapter 2, pages 23–56. Academic Press, San Diego, Califonia, 2007.

[235] K. McDonald and M.K. Morphew. Improved preservation of ultrastructure in difficult-to-fix organisms by high pressure freezing and freeze substitution: I. *Drosophila Melanogaster* and *Strongylocentrotus Purpuratus* embryos. *Microscopy Research and Technique*, 24:465–473, 1993.

[236] B.F. McEwen and A.B. Heagle. Electron microscopic tomography: a tool for probing the structure and function of subcellular components. *International Journal of Imaging Systems and Technology*, 8(2):175–187, 1997.

[237] B.F. McEwen and M. Marko. Three-dimensional electron microscopy and its application to mitosis research. *Methods in Cell Biology*, 61:81–111, 1999.

[238] A.J. McGibbon, S.J. Pennycook, and D.E. Jesson. Crystal structure retrieval by maximum entropy analysis of atomic resolution incoherent images. *Journal of Microscopy*, 195(1):44–57, 1999.

[239] J.R. McIntosh. Electron microscopy of cells: A new beginning for a new century. *Journal of Cell Biology*, 153(6):F25–F32, 2001.

[240] J.R. McIntosh. Aspects of data collection and analysis. In J.R. McIntosh, editor, *Cellular Electron Microscopy*, volume 79 of *Methods in Cell Biology*, pages 639–642. Academic Press, San Diego, Califonia, 2007.

[241] J.R. McIntosh. Imaging frozen-hydrated cells and cell parts. In J.R. McIntosh, editor, *Cellular Electron Microscopy*, volume 79 of *Methods in Cell Biology*, pages 389–372. Academic Press, San Diego, Califonia, 2007.

[242] J.R. McIntosh. Introduction to electron microscopy of cells. In J.R. McIntosh, editor, *Cellular Electron Microscopy*, volume 79 of *Methods in Cell Biology*, pages xxi–xxvii. Academic Press, San Diego, Califonia, 2007.

[243] R. McIntosh, D. Nicastro, and D. Mastronarde. New views of cells in 3D: An introduction to electron tomography. *Trends in Cell Biology*, 15:43–51, 2005.

[244] T. Meier, K.N. Ngan, and G. Crebbin. A robust markovian segmentation based on highest confidence first. In *Proceedings of IEEE International Conference on Image Processing*, volume 1, pages 216–219. IEEE, 1997.

[245] M. Middendorf and H.-H Nagel. Estimation and interpretation of discontinuities in optical flow fields. In *Proceedings of IEEE Eighth International Conference on Computer Vision*, pages 178–183, Vancouver, Canada, July 2001. IEEE Computer Society Press.

[246] M. Middendorf and H.-H. Nagel. Empirically convergent adaptive estimation of grayvalue structure tensors. *Lecture Notes in Computer Science*, 2449:66–74, 2002.

[247] K. Mikula and N. Ramarosy. Semi-implicit finite volume schemes for solving nonlinear diffusion equations in image processing. *Numerische Mathematik*, 89(3):561–590, 2001.

[248] K. Mikula, A. Sarti, and C. Lamberti. Geometrical diffusion in 3-d-echocardiography. In J. Kačur and K. Mikula, editors, *Proceedings of ALGORITMY '97, Conference on Scientific Computing*, volume 67, pages 167–181. Acta Mathematica Universitatis Comenianae, 1998.

[249] J.A. Mindell and N. Grigorieff. Accurate determination of local defocus and specimen tilt in electron microscopy. *Journal of Structural Biology*, 142(3):334–347, 2003.

[250] D.L. Misell. Image formation in the electron microscope: I. the application of transfer theory to a consideration of elastic electron scattering. *Journal of Physics A: General Physics*, 4:782–797, 1971.

[251] D.L. Misell. Image formation in the electron microscope: II. the application of transfer theory to a consideration of inelastic electron scattering. *Journal of Physics A: General Physics*, 4:798–812, 1971.

[252] H. Moor. Theory and practice of high pressure freezing. In R.A. Steinbrecht and K. Zierold, editors, *Cryotechniques in Biological Electron Microscopy*, pages 175–191. Springer-Verlag, Berlin, Germany, 1987.

[253] P. Mrázek. *Nonlinear Diffusion for Image Filtering and Monotonicity Enhancement*. PhD thesis, Czech Technical University, Prague, Czech Republic, 2001.

[254] P. Mrázek. Selection of optimal stopping time for nonlinear diffusion filtering. In M. Kerckhove, editor, *Third International Conference on Scale-Space and Morphology in Computer Vision*, pages 290–298, Berlin, Germany, 2001. IEEE Computer Society, Springer-Verlag.

[255] P. Mrázek and M. Navara. Selection of optimal stopping time for nonlinear diffusion filtering. *International Journal of Computer Vision*, 52(2/3):189–203, 2003.

[256] P. Mrázek, J. Weickert, and A. Bruhn. *On Robust Estimation and Smoothing with Spatial and Tonal Kernels*, pages 335–352. Geometric Properties from Incomplete Data. Springer, Dordrecht, Holland, 2006.

[257] A. Munnich and P. Rustin. Clinical spectrum and diagnosis of mitochondrial disorders. *American Journal of Medical Genetics*, 106:4–17, 2001.

[258] A. Munnich and P. Rustin. Clinical spectrum and diagnosis of mitochondrial disorders. *American Journal of Medical Genetics*, 106:4–17, 2001.

[259] J.L.A.N. Murk, G. Posthuma, A.J. Koster, H.J. Geuze, A.J. Verkleij, M.J. Kleijmeer, and B.M. Humbel. Influence of aldehyde fixation on the morphology of endosomes and lysosomes: Quantitative analysis and electron tomography. *Journal of Microscopy*, 212(1):81–90, 2003.

[260] M. Nagao and T. Matsuyama. Edge preserving smoothing. *Computer Graphics and Image Processing*, 9(4):394–407, 1979.

[261] H.-H. Nagel and A. Gehrke. Spatiotemporally adaptive estimation and segmentation of OF-fields. *Lecture Notes in Computer Science*, (1407):86–102, 1998.

[262] R. Narasimha, I. Aganj, M. Borgnia, G. Sapiro, S. McLaughlin, J. Milne, and S. Subramaniam. From gigabytes to bytes: Automated denoising and feature identification in electron tomograms of intact bacterial cells. In *Proceedings of 4th IEEE International Symposium in Biomedical Imaging: From Nano to Macro*, pages 304–307, Arlington, Virginia, 2007. IEEE.

[263] K.S. Nathan and J.C. Curlander. Speckle noise reduction of 1-look SAR imagery. In *Proceedings of IGARSS '87 Symposium*, pages 1457–1462, 1987.

[264] F. Natterer and F. Wübbeling. *Mathematical methods in image reconstruction*. Society for Industrial and Applied Mathematics, Philadelphia, Pennsylvania, 2001.

[265] P. Newmark. Cryo-transmission microscopy: fading hopes. *Nature*, 299:386–387, 1982.

[266] S. Nickell, F. Forster, A. Linaroudis, W.D. Net, F. Beck, R. Hegerl, W. Baumeister, and J.M. Plitzko. TOM software toolbox: Acquisition and analysis for electron tomography. *Journal of Structural Biology*, 149(3):227–234, 2005.

[267] I. Nishino, O. Kobayashi, Y. Goto, M. Kurihara, K. Kumagai, T. Fujita, K. Hashimoto, S. Horai, and I. Nonaka. A new congenital muscular dystrophy with mitochondrial structural abnormalities. *Muscle Nerve*, 21:40–47, 1998.

[268] M. Nitzberg and T. Shiota. Nonlinear image filtering with edge and corner enhancement. *IEEE Transactions on Pattern Analysis and Machine Intelligence*, 14(8):826–833, 1992.

[269] N. Nordström. Biased anisotropic diffusion: a unified regularization and diffusion approach to edge detection. *Image and Vision Computing*, 8(11):318–327, 1990.

[270] M. Obeid, A. Tesniere, F. Ghiringhelli, G.M. Fimia, L. Apetoh, J.L. Perfettini, M. Castedo, G. Mignot, T. Panaretakis, N. Casares, D. Metivier, N. Larochette, P. van Endert, F. Ciccosanti, M. Piacentini, L. Zitvogel, and G. Kroemer. Calreticulin exposure dictates the immunogenicity of cancer cell death. *Nature Medicine*, 13(1):54–61, 2007.

[271] C.J. Oddy and A.J. Rye. Segmentation of SAR images using a local similarity rule. *Pattern Recognition Letters*, 1:443–449, 1983.

[272] J.E. Odegard, H. Guo, M. Lang, C.S. Burrus, R.O. Wells Jr., L. M. Novak, and M. Hiett. Wavelet based SAR speckle reduction and image compression. In *SPIE Proceedings*, volume 2487, pages 259–271, 1995.

[273] L.G. Ofverstedt, K. Zhang, L.A. Isaksson, G. Bricogne, and U. Skoglund. Automated correlation and averaging of three-dimensional reconstructions obtained by electron tomography. *Journal of Structural Biology*, 120(3):329–342, 1997.

[274] B.M. Oh, M. Chen, J. Dorsey, and F. Durand. Image-based modeling and photo editing. In *Proceedings of International Conference on Computer Graphics and Interactive Techniques*, pages 433–442. ACM, 2001.

[275] A. Oppenheim. *Superposition in a Class of Nonlinear Systems.* PhD thesis, Massachusetts Institute of Technology, Cambridge, MA, 1964.

[276] S. Osher, M. Burger, D. Goldfarb, J. Xu, and W. Yin. An iterative regularization method for total variation-based image restoration. *SIAM Multiscale Modeling and Simulation*, 4(2):460–489, 2005.

[277] S. Osher and R. Fedkiw. *Level Set Methods and Dynamic Implicit Surfaces*, volume 153. Springer, New York, New York, 2003.

[278] S. Osher and J. Sethian. Fronts propagating with curvature-dependent speed: Algorithms based on the hamilton-jacobi formulation. *Journal of Computational Physics*, 79:12–49, 1988.

[279] S. Osher, A. Solé, and L. Vese. Image decomposition and restoration using total variation minimization and the H^{-1} norm. *SIAM Journal on Multiscale Modeling and Simulation*, 1(3):349–370, 2003.

[280] V.P. Palamodov. Reconstructive integral geometry. In *Monographs in Mathematics*, volume 98. Springer, Berlin, Germany, 2004.

[281] V.Y. Panin, G.L. Zeng, and G.T. Gullberg. Total variation regulated EM algorithm. *IEEE Transactions on Nuclear Science*, 46(6):2022–2210, 1999.

[282] G. Papandreou and P. Maragos. A cross-validatory statistical approach to scale selection for image denoising by nonlinear diffusion. In *Proceedings of IEEE Computer Society Conference on Computer Vision and Pattern Recognition*, volume 1, pages 625–630. IEEE, 2005.

[283] S. Paris and F. Durand. A fast approximation of the bilateral filter using a signal processing approach. In *Proceedings of European Conference on Computer Vision*, pages 568–580, 2006.

[284] S. Paris, P. Kornprobst, and F. Tumblin, J. Durand. A gentle introduction to bilateral filtering and its applications. In *International Conference on Computer Graphics and Interactive Techniques*. ACM SIGGRAPH 2007, Association for Computing Machinery, 2007.

[285] P.A. Penczek. Three-dimensional spectral signal-to-noise ratio for a class of reconstruction algorithms. *Journal of Structural Biology*, 138(1-2):34–46, 2002.

[286] P.A. Penczek. Variance in three-dimensional reconstructions from projections. In *Proceedings of 1st IEEE International Symposium on Biomedical Imaging*, pages 749–752. IEEE, 2002.

[287] P.A. Penczek and J. Frank. Resolution in electron tomography. In J. Frank, editor, *Electron Tomography: Methods for Three-Dimensional Visualization of Structures in the Cell*, chapter 10, pages 307–330. Springer, Berlin, Germany, 2nd edition, 2006.

[288] L.-M. Peng, S.L. Dudarev, and M.J. Whelan. High-energy electron diffraction and microscopy. In *Monographs on the Physics and Chemistry of Materials*, volume 61. Oxford University Press, Oxford, England, 2004.

[289] G. Perkins and T. Frey. Electron tomography. In T. Creighton, editor, *Encyclopedia of Molecular Biology*, pages 796–. John Wiley & Sons, New York, New York, 1999.

[290] G.A. Perkins and T.G. Frey. Recent structural insight into mitochondria gained by microscopy. *Micron*, 31(1):97–111, 2000.

[291] G.A. Perkins, C.W. Renken, T.G. Frey, and M.H. Ellisman. Membrane architecture of mitochondria in neurons of the central nervous system. *Journal of Neuroscience Research*, 66:857–865, 2001.

[292] G.A. Perkins, C.W. Renken, J.Y. Song, T.G. Frey, S.J. Young, S. Lamont, M.E. Martone, S. Lindsey, and M.H. Ellisman. Electron tomography of large, multicomponent biological structures. *Journal of Structural Biology*, 120(3):219–227, 1997.

[293] G.A. Perkins, J.Y. Song, L. Tarsa, T.J. Deerinck, M.H. Ellisman, and T.G. Frey. Electron tomography of mitochondria from brown adipocytes reveals crista junctions. *Journal of Bioenergetics and Biomembranes*, 30(5):431–442, 1998.

[294] P. Perona and J. Malik. Scale space and edge detection using anisotropic diffusion. *IEEE Transactions on Pattern Analysis and Machine Intelligence*, 12(7):629–639, 1990.

[295] P. Perona, T. Shiota, and J. Malik. Anisotropic diffusion. In B.M. ter Haar Romeny, editor, *Geometry-Driven Diffusion in Computer Vision*, volume 1 of *Computational Imaging and Vision*, pages 72–92. Springer, Kluwer, 1994.

[296] M. Persson, D. Bone, and H. Elmqvist. Total variation norm for three-dimensional iterative reconstruction in limited view angle tomography. *Physics in Medicine and Biology*, 46(3):853–866, 2001.

[297] P.X. Petit, M. Goubern, P. Diolez, S.A. Susin, N. Zamzami, and G. Kroemer. Disruption of the outer mitochondrial membrane as a result of mitochondrial swelling. The impact of irreversible permeability transition. *Federation of European Biochemical Societies Letters*, 426:111–116, 1998.

[298] G. Petschnigg, M. Agrawala, H. Hoppe, R. Szeliski, M. Cohen, and K. Toyama. Digital photography with flash and non-flash image pairs. *ACM Transactions on Graphics*, 23(3):664–672, 2004.

[299] T.Q. Pham and L.J. van Vliet. Separable bilateral filtering for fast video preprocessing. In *Proceedings of IEEE International Conference on Multimedia*, pages 4–7. IEEE, 2005.

[300] J. Plitzko and W. Baumeister. Cryoelectron tomography (CET). In P.W. Hawkes and J.C.H. Spence, editors, *Science of Microscopy*, chapter 7, page 535604. Springer, Berlin, Germany, 2007.

[301] L.A. Pon and E.A. Schon. Preface. In L.A. Pon and E.A. Schon, editors, *Mitochondria*, pages xxiii–xxiv. Academic Press, San Diego, California, 2007.

[302] T. Preusser and M. Rumpf. An adaptive finite element method for large scale image processing. In *Proceedings of Scale-Space '99*, pages 223–234, 1999.

[303] M. Proesmans, E.J. Pauwels, L.J. van Gool, T. Moons, and A. Oosterlinck. Image enhancement using non-linear diffusion. In *Proceedings IEEE Computer Society Conference on Computer Vision and Pattern Recognition*, volume 15-17, pages 680–681. IEEE Computer Society, 1993.

[304] M. Rademacher. Weighted back-projection methods. In J. Frank, editor, *Electron Tomography, Three-Dimensional Imaging with Transmission Electron Microscope*, pages 91–115. Plenum Press, New York, New York, 1992.

[305] J. Radon. Über die bestimmung von funktionen durch ihre integralwerte längs bestimmter mannigfaltigkeiten. In A.M.K. Thomas, A.K. Banerjee, and

U. Busch, editors, *Classic Papers in Modern Diagnostic Radiology*, chapter 1, pages 5–22. Springer, New York, New York, 2005.

[306] G.N. Ramachandran and A. V. Lakshminarayanan. Three-dimensional reconstruction from radiographs and electron micrographs: application of convolutions instead of fourier transforms. *Proceedings of National Academy of Science*, 68:2236–2240, 1971.

[307] R. Ramanath and W.E. Snyder. Adapting demosaicking. *Journal of Electronic Imaging*, 12(4):633–642, 2003.

[308] L. Reimer. Transmission electron microscopy. In *Springer Series in Optical Sciences*, volume 36. Springer, New York, New York, 4th edition, 1997.

[309] D. Ress, M.L. Harlow, M. Schwarz, R.M. Marshall, and U.J. McMahan. Automatic acquisition of fiducial markers and alignment of images in tilt series for electron tomography. *Journal of Electron Microscopy*, 48(3):277–287, 1999.

[310] D.B. Ress, M.L. Harlow, R.M. Marshall, and U.J. McMahan. Methods for generating high-resolution structural models from electron microscope tomography data. *Structure*, 12(10):1763–1774, 2004.

[311] A. Rose. Quantum limitations to vision at low light levels. *Image Technology*, 12:13–32, 1970.

[312] L. Rudin, P.-L. Lions, and S. Osher. *Geometric Level Set Methods in Imaging, Vision, and Graphics*, chapter Multiplicative Denoising and Deblurring: Theory and Algorithms. Springer-Verlag, New York, 2003.

[313] L. Rudin and S. Osher. Reconstruction and enhancement of signals using nonlinear non-oscillatory variational methods. Technical Report 7, Cognitech, Pasadena, California, 1990.

[314] L. Rudin, S. Osher, and Fatemi E. Nonlinear total variation based noise removal algorithm. *Physica D*, 60(1-4):259–268, 1992.

[315] H. Rullgård, O. Öktem, and U. Skoglund. A componentwise iterated relative entropy regularization method with updated prior and regularization parameter. *Inverse Problems*, 23:2121–2139, 2007.

[316] B.B. Saevarrson, J.R. Sveinsson, and J.A. Benediktsson. Speckle reduction of SAR images using adaptive curvelet domain. In *Proceedings of IEEE International Geoscience and Remote Sensing Symposium*, volume 6, pages 4083–4085, 2003.

[317] B.B. Saevarrson, J.R. Sveinsson, and J.A. Benediktsson. Combined wavelet and curvelet denoising of SAR images. In 6, editor, *Proceedings of IEEE International Geoscience and Remote Sensing Symposium*, pages 4235–4238, 2004.

[318] B.E.H. Saxberg and W.O. Saxton. Quantum noise in 2d projections and 3d reconstructions. *Ultramicroscopy*, 6(1):85–89, 1981.

[319] I.E. Scheffler. A century of mitochondrial research: Achievements and perspectives. *Mitochondrion*, 1:3–31, 200.

[320] C. Schnörr. Unique reconstruction of piecewise smooth images by minimizing strictly convex non-quadratic functionals. *Journal of Mathematical Imaging and Vision*, 4(2):189–198, 1994.

[321] P. Schults, E. Bollt, R. Chartrand, S. Esedoglu, and K. Vixie. Graduated adaptive image denoising: Local compromise between total variation and isotropic diffusion. Preprint, 2005.

[322] D. Sen, M.N.S. Swamy, and M.O. Ahmad. Unbiased homomorphic system and its application in reducing multiplicative noise. *IEEE Proceedings Vision, Image, and Signal Processing*, 153(5):521–537, 2006.

[323] J. A. Sethian. *Level Set Methods and Fast Marching Methods*. Cambridge University Press, Cambridge, Massachusetts, 1999.

[324] J.A. Sethian. A fast marching level set method for monotonically advancing fronts. *Proceedings of National Academy of Science*, 93(4):1591–1595, 1996.

[325] L.A. Shepp and B.F. Logan. The Fourier reconstruction of a head section. *IEEE Transactions on Nuclear Science*, 21:21–43, 1974.

[326] E.Y. Sidky, C.M. Kao, and X. Pan. Accurate image reconstruction from few-views and limited-angle data in divergent-beam CT. *Journal of X-Ray Science and Technology*, 14(2):119–139, 2006.

[327] D. Skladal, J. Halliday, and D.R. Thorburn. Minimum birth prevalence of mitochondrial respiratory chain disorders in children. *Brain*, 126:1905–1912, 2003.

[328] U. Skoglund, L.-G. Öfverstedt, R.M. Burnett, and G. Bricogne. Maximum-entropy three-dimensional reconstruction with deconvolution of the contrast transfer function: A test application with adenovirus. *Journal of Structural Biology*, 117(3):173–188, 1996.

[329] S.M. Smith and J.M. Brady. SUSAN-a new approach to low level image processing. *International Journal of Computer Vision*, 23(1):45–78, 1997.

[330] N. Sochen, R. Kimmel, and A.M. Bruckstein. Diffusion and confusions in signal and image processing. *Journal of Mathematical Imaging and Vision*, 14(3):237–244, 2001.

[331] V. Solo. A fast automatic stopping criterion for anisotropic diffusion. In *Proceedings of IEEE International Conference on Acoustics, Speech, and Signal Processing*, volume 2, pages 1661–1664. IEEE, 2002.

[332] B. Song. *Topics in Variational PDE Image Segmentation, Inpainting and Denoising*. PhD thesis, University of California Los Angeles, Los Angeles, California, 2003.

[333] C.O. Sorzano, R. Marabini, J. Velazquez-Muriel, J.R. Bilbao-Castro, S.H. Scheres, J.M. Carazo, and A. Pascual-Montano. XMIPP: A new generation of an open-source image processing package for electron microscopy. *Journal of Structural Biology*, 148(2):194–204, 2004.

[334] D. Sousa and N. Grigorieff. Ab initio resolution measurement for single particle structures. *Journal of Structural Biology*, 157(1):201–210, 2007.

[335] J.C.H. Spence. *High-Resolution Electron Microscopy*, volume 60 of *Monographs on the Physics and Chemistry of Materials*. Oxford University Press, Oxford, United Kingdom, 2003.

[336] J.C.H. Spence and J.M. Zuo. Large dynamic range, parallel detection system for electron diffraction and imaging. *Review of Scientific Instruments*, 59(9):2102–2105, 1988.

[337] J. Sporring and J. Weickert. Information measures in scale-spaces. *IEEE Transactions on Information Theory*, 45(3):1051–1058, 1999.

[338] J.-L. Starck, E.J. Candès, and D.L. Donoho. The curvelet transform for image denoising. *IEEE Transactions on Image Processing*, 11(6):670–684, 2002.

[339] R.A. Steinbrecht and M. Müller. Freeze substitute and freeze-drying. In R.A. Steinbrecht and K. Zierold, editors, *Cryotechniques in Biological Electron Microscopy*, pages 149–172. Springer-Verlag, Berlin, Germany, 1987.

[340] A Stoschek and R. Hegerl. Denoising of electron tomographic reconstructions using multiscale transformations. *Journal of Structural Biology*, 120(3):257–265, 1997.

[341] D. Strong and T. Chan. Spatially and scale adaptive total variation based regularization and anisotropic diffusion in image processing. Technical Report 46, University of California Los Angeles, Los Angeles, 1996.

[342] D. Strong and T. Chan. Edge-preserving and scale-dependent properties of total variation regularization. *Inverse Problems*, 19(6):165–187, 2003.

[343] S. Subramaniam. Bridging the imaging gap: Visualizing subcellular architecture with electron tomography. *Current Opinion in Microbiology*, 8:316–322, 2005.

[344] C. Suloway, J. Pulokas, D. Fellmann, A. Cheng, F. Guerra, J. Quispe, S. Stagg, C.S. Potter, and B. Carragher. Automated molecular microscopy: The new Leginon system. *Journal of Structural Biology*, 151(1):41–60, 2005.

[345] B. Tandler, M. Dunlap, C.L. Hoppel, and M. Hassan. Giant mitochondria in a cardiomyopathic heart. *Ultrastructural Pathology*, 26:177–183, 2002.

[346] G. Tang, L. Peng, P.R. Baldwin, D.S. Mann, W. Jiang, I. Rees, and S.J. Ludtke. EMAN2: An extensible image processing suite for electron microscopy. *Journal of Structural Biology*, 157(1):38–46, 2007.

[347] K.A. Taylor, J. Tang, Y. Cheng, and H. Winkler. The use of electron tomography for structural analysis of disordered protein arrays. *Journal of Structural Biology*, 120(3):372–386, 1997.

[348] Wikipedia the free encyclopedia. HeLa. Retrieved August 4, 2008. Web site: http://en.wikipedia.org/wiki/HeLa.

[349] C. Tomasi and R. Manduchi. Bilateral filtering for gray and color images. In *Proceedings of IEEE International Conference on Computer Vision*, pages 839–846. IEEE, 1998.

[350] H.L.V. Trees. *Estimation and modulation theory part I.* John Wiley & Sons, New York, 2001.

[351] D. Typke, K. Dierksen, and W. Baumeister. Automatic electron tomography. In *49th Annual Meeting of the Electron Microscopy Society of America*, pages 544–545, San Francisco, California, 1991. EMSA, San Francisco Press.

[352] F. Ulaby and M.C. Dobson. *Handbook of Radar Scattering Statistics for Terrain.* Artech House, Norwood, MA, 1989.

[353] M.O. Ulfarsson, J.R. Sveinsson, and J.A. Benediktsson. Speckle reduction of SAR images in the curvelet domain. In *Proceedings of IEEE International Geoscience and Remote Sensing Symposium*, volume 1, pages 315–317, 2002.

[354] M. Unser, C.O.S. Sorzano, Thévenaz P., S. Jonić, C. El-Bez, S. De Carlo, J.F. Conway, and B.L. Trus. Spectral signal-to-noise ratio and resolution assessment of 3D reconstructions. *Journal of Structural Biology*, 149(3):243–255, 2005.

[355] P.N.T. Unwin and R. Henderson. Molecular structure determination by electron microscopy of unstained crystalline specimens. *Journal of Molecular Biology*, 94(3):425–440, 1975.

[356] B.K. Vainshtein. Finding the structure of objects from projections. *Kristallografiya*, 15:894–902, 1970.

[357] J. van de Weijer and R. van den Boomgaard. Local mode filtering. In *Proceedings of IEEE Computer Society Conference on Computer Vision and Pattern Recognition*, volume 2, pages 428–433, 2001.

[358] J. van de Weijer and R. van den Boomgaard. On the equivalence of local-mode finding, robust estimation and mean-shift analysis as used in early vision tasks.

In *Proceedings of International Conference on Pattern Recognition*, volume 3, pages 927–930, 2002.

[359] R. van den Boomgaard. The Kuwahara-Nagao operator decomposed in terms of a linear smoothing and a morphological sharpening. In H. Talbot and R. Beare, editors, *Proceedings of 6th International Symposium on Mathematical Morphology*, pages 283–292, Sydney, Australia, April 2002. CSIRO Publishing.

[360] R. van den Boomgaard and J. van de Weijer. Robust estimation of orientation for texture analysis. In *Proceedings of Texture 2002, 2nd International Workshop on Texture Analysis and Synthesis*, Copenhagen, Denmark, June 2002.

[361] P. van der Heide, X.-P. Xu, B.J. Marsh, D. Hanein, and N. Volkmann. Efficient automatic noise reduction of electron tomographic reconstructions based on iterative median filtering. *Journal of Structural Biology*, 158(2):196–204, 2007.

[362] M.G. Van der Heiden, N.S. Chandal, E.K. Williamson, P.T. Schumacker, and C.B. Thompson. Bcl-XL regulates the membrane potential and volume homeostasis of mitochondria. *Cell*, 91:627–637, 1997.

[363] M. van Heel and G. Harauz. Resolution criteria for three dimensional reconstruction. *Optik*, 73:119–122, 1986.

[364] L. Vese and S. Osher. Modeling textures with total variation minimization and oscillating patterns in image processing. *Journal of Scientific Computing*, 19(1-3):553–572, 2003.

[365] C.R. Vogel and M.E. Oman. Iterative methods for total variation denoising. *SIAM Journal on Scientific Computing*, 17(1):227–238, 1996.

[366] N. Volkmann. A novel three-dimensional variant of the watershed transform for segmentation of electron density maps. *Journal of Structural Biology*, 138(1-2):123–129, 2002.

[367] N. Volkmann. A novel three-dimensional variant of the watershed transform for segmentation of electron density maps. *Journal of Structural Biology*, 138(1-2):123–129, 2002.

[368] D.R. Wehner. *High-Resolution Radar*. Artech House, Boston, MA, 2nd edition, 1994.

[369] J. Weickert. Anisotropic diffusion filters for image processing based quality control. In A. Fasano and M. Primicerio, editors, *Proceedings of Seventh European Conference on Mathematics in Industry*, pages 355–362. Teubner, Stuttgart, Germany, 1994.

[370] J. Weickert. Scale-space properties of nonlinear diffusion filtering with diffusion tensor. Report 110, Laboratory of Technomathematics, University of Kaiserslautern, Kaiserslautern, Germany, 1994.

[371] J. Weickert. Theoretical foundations of anisotropic diffusion in image processing. In *Proceedings of 7th TFCV on Theoretical Foundations of Computer Vision*, volume 11 of *Computing Supplement*, pages 221–236, London, 1994. Springer-Verlag.

[372] J. Weickert. Multiscale texture enhancement. In V. Hlaváč and Šára, editors, *Computer Analysis of Images and Patterns, Lecture Notes in Computer Science*, pages 230–237. Springer, Berlin, Germany, 1995.

[373] J. Weickert. *Anisotropic Diffusion in Image Processing*. PhD thesis, Universität Kaiserslautern, Kaiserslautern, Germany, 1996.

[374] J. Weickert. Theoretical foundations of anisotropic diffusion in image processing. *Computing Supplement*, 11:221–236, 1996.

[375] J. Weickert. *Anisotropic Diffusion in Image Processing*. ECMI Series. Teubner-Verlag, Stuttgart, 1998.

[376] J. Weickert. Coherence-enhancing diffusion filtering. *International Journal of Computer Vision*, 31(2/3):111–127, 1999.

[377] J. Weickert. Coherence-enhancing diffusion of colour images. *Image and Vision Computing*, 17(3):201–212, 1999.

[378] J. Weickert. Applications of nonlinear diffusion in image processing and computer vision. *Acta Mathematica Universitatis Comenianae*, LXX(1):33–50, 2001.

[379] J. Weickert. Efficient image segmentation using partial differential equations and morphology. *Pattern Recognition*, 34(9):1813–1824, 2001.

[380] J. Weickert and T. Brox. Diffusion and regularization of vector- and matrix-valued images. In M. Z. Nashed and O. Scherzer, editors, *Inverse Problems, Image Analysis, and Medical Imaging. Contemporary Mathematics*, volume 313, pages 251–268. AMS, Providence, Rhode Island, 2002.

[381] J. Weickert, B.M.t.H. Romeny, and M.A. Viergever. Efficient and reliable schemes for nonlinear diffusion filtering. *IEEE Transactions on Image Processing*, 7(3):398–410, 1998.

[382] J. Weickert and H. Scharr. A scheme for coherence-enhancing diffusion filtering with optimized rotation invariance. *Journal of Visual Communication and Image Representation*, 13(1/2):103–118, 2002.

[383] J. Weickert and C. Schnörr. PDE-based preprocessing of medical images. *Kunstliche Intelligenz*, 3:5–10, 2000.

[384] B. Weiss. Fast median and bilateral filtering. *ACM Transactions on Graphics*, 25(3):519–526, 2006.

[385] R.T. Whitaker and S.M. Pizer. A multi-scale approach to non-uniform diffusion. *Computer Vision, Graphics, and Image Processing: Image Understanding*, 57(1):99–110, 1993.

[386] J. Wiklund, Nicolas V., A.P. Rondao, M. Andersson, and H. Knutsson. T-FLASH: Tensor visualization in medical studio. In *Proceedings of Similar NoE Tensor Workshop*, Las Palmas, Spain, 2006.

[387] H. Winkler. 3D reconstruction and processing of volumetric data in cryo-electron tomography. *Journal of Structural Biology*, 157(1):126–137, 2007.

[388] H. Winkler and K.A. Taylor. Focus gradient correction applied to tilt series image data used in electron tomography. *Journal of Structural Biology*, 143(1):24–32, 2003.

[389] H. Winkler and K.A. Taylor. Accurate marker-free alignment with simultaneous geometry determination and reconstruction of tilt series in electron tomography. *Ultramicroscopy*, 106(3):240–254, 2006.

[390] H. Winnermöller, S.C. Olsen, and B. Gooch. Real-time video abstraction. *ACM Transactions on Graphics*, 25(3):1221–1226, 2006.

[391] P.J. Withagen, F.C.A. Groen, and K. Schutte. CCD characterization for a range of color cameras. In *Proceedings of IEEE Instrumentation and Measurement Technology Conference*, volume 3, pages 2232–2235, 2005.

[392] A.P. Witkin. Space-scale filtering. In A. Bundy, editor, *Proceedings of Eighth International Joint Conference on Artificial Intelligence*, pages 1019–1022, San Francisco, California, 1983. Morgan Kaufmann.

[393] A.P. Witkin. Scale-space filtering: A new approach to multi-scale description. In *Proceedings of IEEE International Conference on Acoustic, Speech & Signal Processing*, volume 9, pages 150–153, 1984.

[394] De Ruijter W.J. Imaging properties and applications of slow-scan charge-coupled device cameras suitable for electron microscopy. *Micron*, 26(3):247–275, 1995.

[395] W. Wriggers, P. Chacón, J. Kovacs, F. Tama, and S. Birmanns. Topology representing neural networks reconcile biomolecular shape, structure, and dynamics. *Neurocomputing*, 56:365–379, 2004.

[396] W. Wriggers, R.A. Milligan, and J.A. McCammon. Situs: A package for docking crystal structures into low-resolution maps from electron microscopy. *Journal of Structural Biology*, 133(2-3):85–195, 1999.

[397] H. Xie, L.E. Pierce, and F.T. Ulaby. Statistical properties of logarithmically transformed speckle. *IEEE Transactions on Geoscience and Remote Sensing*, 40(3):721–726, 2002.

[398] C. Yang, P.A. Penczek, A. Leith, F.J. Asturias, E.G. Ng, R.M. Glaeser, and J. Frank. The parallelization of SPIDER on distributed-memory computers using MPI. *Journal of Structural Biology*, 157(1):240–249, 2007.

[399] N. Zamzami, C. Maisse, D. Métivier, and G. Kroemer. Measurement of membrane permeability and the permeability transition of mitochondria. In L.A. Pon and E.A. Schon, editors, *Mitochondria*, volume 80 of *Methods in Cell Biology*, chapter 16, pages 327–340. Academic Press, San Diego, California, 2007.

[400] N. Zamzami, S.A. Susin, P. Marchetti, T. Hirsch, I. Gómez-Monterrey, M. Castedo, and G. Kroemer. Mitochondrial control of nuclear apoptosis. *Journal of Experimental Medicine*, 183:1533–1544, 1996.

[401] P. Zhang, R.M. Weis, P.J. Peters, and S. Subramaniam. Electron tomography of bacterial chemotaxis receptor assemblies. In J.R. McIntosh, editor, *Cellular Electron Microscopy*, volume 79 of *Methods in Cell Biology*, chapter 14, pages 373–384. Academic Press, San Diego, Califonia, 2007.

[402] X.Q. Zhang and J. Froment. Total variation based fourier reconstruction and regularization for computer tomography. In *Proceedings of Nuclear Science Symposium and Medical Imaging Conference*, volume 4, pages 2332–2336, 2005.

[403] Q.S. Zheng, M.B. Braunfeld, J.W. Sedat, and D.A. Agard. An improved strategy for automated electron microscopic tomography. *Journal of Structural Biology*, 147(2):91–101, 2004.

[404] Q.S. Zheng, B. Keszthelyi, E. Branlund, J.M. Lyle, M.B. Braunfeld, J.W. Sedat, and Agard D.A. UCSF tomography: An integrated software suite for real-time electron microscopic tomographic data collection, alignment, and reconstruction. *Journal of Structural Biology*, 157(1):138–147, 2007.

[405] J. Zhu, P.A. Penczek, R. Schröder, and J. Frank. Three-dimensional reconstruction with contrast transfer function correction from energy-filtered cryoelectron micrographs: Procedure and application to the 70s *Escherichia coli* ribosome. *Journal of Structural Biology*, 118(3):197–219, 1997.

[406] U. Ziese, W.J.C. Geerts, T.P. Van Der Krift, A.J. Verkleij, and A.J. Koster. Correction of autofocusing errors due to specimen tilt for automated electron tomography. *Journal of Microscopy*, 211(2):179–185, 2003.

[407] U. Ziese, A.H. Janssen, J.L. Murk, W.J. Geerts, T. Van der Krift, A.J. Verkleij, and A.J. Koster. Automated high-throughput electron tomography by precalibration of image shifts. *Journal of Microscopy*, 205(2):187–200, 2002.

[408] X. Zong, A.F. Laine, and E.A. Geiser. Speckle reduction and contrast enhancement of echocardiograms via multiscale nonlinear processing. *IEEE Transactions on Medical Imaging*, 17:532–540, 1998.

[409] M. Zoratti and I. Szabò. The mitochondrial permeability transition. *Biochimica et Biophysica Acta–Reviews on Biomembranes*, 1241:139–176, 1995.

[410] J.M. Zuo. Electron detection characteristics of a slow-scan CCD camera, imaging plates and film, and electron image restoration. *Microscopy Research and Technique*, 49(3):245–268, 2000.